Modeling, Simulation and Design of Plasmonic Nanoarchitectures for Ultrafast Circuit Systems

by

Kyungjun Song

A dissertation submitted in partial fulfillment
of the requirements for the degree of
Doctor of Philosophy
(Mechanical Engineering)
in The University of Michigan
2010

Doctoral Committee:

Professor Pinaki Mazumder, Co-Chair
Professor A. Galip Ulsoy, Co-Chair
Professor Anthony M. Waas
Associate Professor Igor L. Markov

For my family

ACKNOWLEDGEMENTS

I am deeply indebted to many people who helped me pursuing and finishing my Ph.D at the University of Michigan.

First of all, I would like to appreciate my advisor, Professor Pinaki Mazumder, for his continued support and ingenious guidance throughout my Ph.D study. He leads me to explore the interesting plasmonics research topics and consistently encourage me to make a significant progress. Having worked with him more than five and half years, I am sure that his creativity and insight will continue to influence my future research work.

Furthermore, I would like to express my sincere gratitude to Professor A. Galip Ulsoy for serving on my co-advisor and giving me invaluable suggestions. In addition, I really appreciate to Professor Anthony M. Waas and Associate Professor Igor L. Markov for serving on my doctoral committee.

I also thank the memebers of our NRD research group : Taeil Jung, Byungsoo Kim, Woo-Hyung Lee, Manoj Rajagopalan, Idongesit E.Ebong and Baohua Wang.

Among my friends I have known in University Michigan, I also would like to thank Donghyun Lee, Donghuck Kam, Jedo Kim, Sungchan Bae, Jeonghoon Ryou, Haewon Park and Jaeil Ahn.

Finally, since my family give me a lot of support and encouragement throughout the long journey, I would like to express my gratitude to them.

TABLE OF CONTENTS

LIST OF FIGURES

Figure

LIST OF TABLES

Table

ABSTRACT

Modeling, Simulation and Design of Plasmonic Nanoarchitectures for Ultrafast Circuit Systems

by

Kyungjun Song

Co-Chairs : Pinaki Mazumder and A. Galip Ulsoy

The dissertation focuses on a new ultrafast circuit system based on plasmonic nanoarchitectures. To achieve this goal, we investigate novel plasmonic devices to integrate with nanoelectronics, resulting in enormous signal functionality, integration and computing speed. First, we concentrate on metallic nanoparticles arrays and metallic nanowires because these plasmonic nanoarchitectures provide a promising way to localize the light below the diffraction limit, thus yielding the feasibility of integration of optical-electronic devices. Specifically, we develop SPICE equivalent circuit models which can be easily simulated together with current electronic circuit components. Second, we introduce new plasmonic switches using metallic metamaterials, because surface plasmon modes generate weakly localized surface plasmon polariton confinement in the RF-THz spectrum. Specifically, we build holes, grooves, and dimples at the subwavelength scale, thus creating spoof surface plasmon polariton modes similar to surface plasmon polariton modes existing in the IR-Optical spectrum. Finally, we provide metallic photonic crystal slabs to increase the nanophotodiode sensitivity. Furthermore, the signal detection emitted by nanometer atoms and molecules can be

significantly enhanced by increasing the transmission of light through the metallic photonic slab. Thus, the artificially designed metallic photonic crystal slab allows us to obtain the high sensitivity needed for ultrafast circuit systems.

CHAPTER I

Introduction

1.1 Motivation

Over the past several decades, VLSI integrated circuits assisted by electrons have had a significant impact on industrial and information technology. As predicted by Moore's law, the information density on a chip has doubled every two years, thus computing power has exponentially increased [1],[2]. Even though Moore's law precisely predicted the increase of computing speed for several decades, the exponential trend of computing speed clearly cannot continue indefinitely. Furthermore, such exponential growth will be limited by the current electron architecture. For example, the electrons flow in modern computers operating at high frequency generate serious problems such as power dissipation, small bandwidth and crosstalk. In order to overcome such fundamental issues, particular attention is being paid to on-chip optical data transfer because photon flows provide the high frequency, large photon energy and short wavelength for ultrafast circuit systems [3],[4].

Recently, the feasibility of silicon lasing, photo-detection, and co-integration of on-chip optical interconnects has sparked enormous optimism in the CMOS VLSI industry because intra-chip high-speed binary data transfer via high-bandwidth optical waveguides is expected to solve various limitations of conventional metallic wires which are dominantly used in intra-chip wiring in commercial chips. With

aggressive device and interconnect scaling, metallic interconnect is witnessing several formidable problems, namely, increasing propagation delays on long global wires, increasing power dissipation due to wide-scale insertion of signal boosting buffers, and intrinsic coupling between wires causing signal-dependent time delays and logical faults. Optical interconnect, in contrast, offers very small interconnect delay, high bandwidth of data transfer, significantly reduces power consumption by obviating the need for repeaters, and virtually eliminates the coupling noise and electromagnetic (EM) interference between various adjacent wires [5],[6],[7].

Therefore, future generation VLSI chips will seek convergence of computing and optical communication where photonic signals propagating at 100's of THz speed will stream into a VLSI chip through a fiber optic cable and then the optical data will be down-converted and processed by computing circuitry operating at 10's of GHz speed. However, the real problem is that optical waveguides used in routing optical signals are generally micron-scale wide (10-100 microns) while the electronic components will employ sub-50 nm CMOS technology causing a huge mismatch between device dimensions because the optical pulse cannnot propagate along the conventional waveguide if the size dimension of the waveguide is smaller than the wavelength of the signal pulse [8],[9].

In order to resolve the coupling problem between optical and electronic signals, surface plasmon (SP) is now being extensively pursued for fabricating nanoscale photonic components. Notably, a metal has a negative dielectric permittivity in the optical spectrum, thereby offering the light confinement in subwavelength structures and guiding light over the plasmonic structure. Therefore, plasmonic devices have the potential to integrate optical components with electron devices because nanoscale plasmonic components have the ability to operate at optical frequencies while the physical dimensions are comparable to electronic components [9]. Furthermore, as illustrated in Fig. 1.1, the promising capability of plasmonic devices to combine

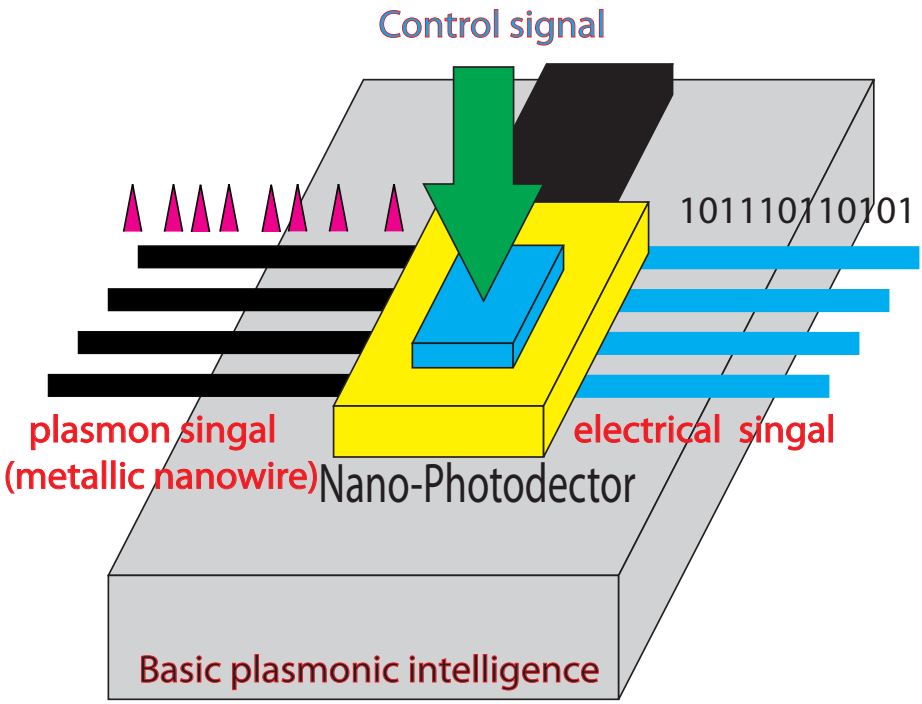

Figure 1.1: Schematic of on-chip integration of plasmonic signals

the electrical functionality, integration and computation can be achieved by using photonic detection devices such as ultrafast photodectors [10] and nanowire field transistors [11].

To achieve light localization on a subwavelength wire based on plasmonic devices, many researchers have investigated one-dimensional plasmonic structures such as metallic nano-particle (MNP) arrays [12],[13],[9],[14],[15] and metallic nanowires (MNW) [8],[16],[17],[18]. With the help of nanofabrication technology such as electron beam lithography (EBL) [19], ordered metallic nanostructures can now be built to manipulate the efficient light-matter coupling between electromagnetic (EM) and metallic nanostructures. For example, the selective optical absorption of a spherical metallic nanoparticle (MNP) allows development of next generation photonic devices such as subwavelength guides [20],[21], focusing elements [21] and SP biosensors [22],[23]. Some analytical caculations [20],[21], numerical approaches [13],[18]

and experiments [12] have demonstrated electromagnetic (EM) signal energy transfer along on array of metallic nanoparticles. In addition, the light confinement method along the metallic nanowires (MNW's) enables to obtain more reliable plasmonic signal transport compared to MNP's chain array. Thus, the SP waves in the metallic nanowires (MNW's) merit special attention due to potential applications in photonic circuitry [24],[25], subwavelength optical imaging [26],[27],[28],[29] and quantum optics [30],[31].

The ultimate goal of this thesis is to develop i) theoretical analysis , ii) physical structures, and iii) optimization of design parameters for plasmonic components combined with semiconductor devices. Specifically, we focus on the local plasmonic interconnect and global plasmonic interconnect to incorporate disparate semiconductor technologies such as CMOS, Si-Ge, semiconductor laser, quantum devices, high electron mobility transistors (HEMT's) and heterojunction bipolar transistors (HBT's).

First, in order to achieve local plasmonic interconnects on a chip, we study the MNP arrays and MNW that can be easily integrated with the current silicon platform. Specifically, we develop SPICE compatible circuit models for plasmonic devices so that they can be simulated together with other CMOS, Si-Ge and Group III-V compound semiconductor devices for which commercial SPICE models are already available. Currently, most of the plasmon devices are stimulated with full-wave Maxwell Equation solvers such as a Finite-Difference Time-Domain (FDTD) simulator which requires a large amount of computing time to model a tiny nanowire. In order to design integrated hybrid systems, as in Fig. 1.1, it will be necessary to develop analytical equations for plasmonic structures so that they can be represented as SPICE equivalent circuit models and can be simulated together with other electronic circuit elements.

However, the limitations of nanoscale plasmonic components are that due to high

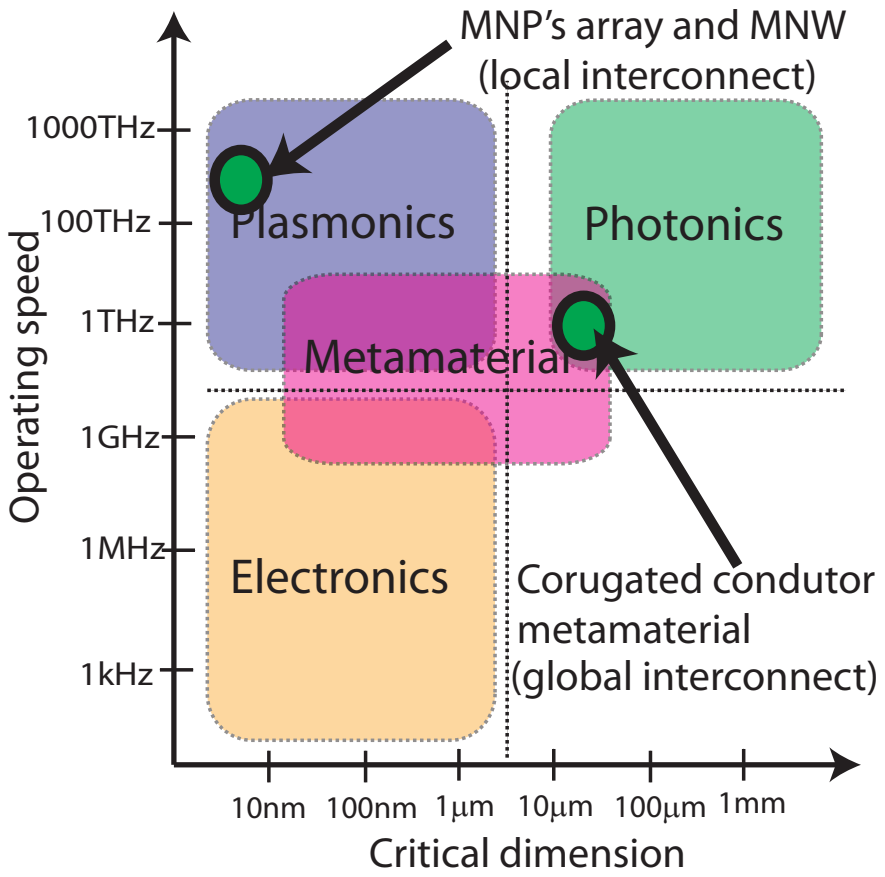

Figure 1.2: Plasmonics is a bridging technology between photonics and electronics because it operates at 100's of THz like photonics at nanoscale dimensions compatible with CMOS electronics

attenuation of SP signal, they can be only used as local interconnects in chip-scale applications. Specifically, the issue of propagation loss along the plamsonic architecture remains to be tackled since the dimension contraction, such as transformation from two-dimensional waves to one-dimensional waves, increases damping coefficients because low-dimensional waves lead to strong momentum waves. Moreover, this significant energy attenuation in the nano-scale domain leads to substantial difficulties in harnessing plasmonics in on-chip nano-scale waveguide and other near-field optical applications.

Next, in order to design long buses and interconnects in VLSI applications, we adopt a new and different method by concentrating on the spoof surface plasmon polariton at near Tera Hertz (THz) speeds as illustrated in Fig. 2. For example, Wang, et el suggested the simple and efficient guiding method based on surface plasmon polariton (SPP) propagating on the simple metal wire, thereby providing low dissipation and low dispersion [32]. Specifically, we demonstrate how to build efficient global plasmonic interconnects by utilizing these mimicking spoof surface plasmon polariton (SSPP) modes [33],[34]. However, to perform more complex signal routing (and process arbitrary Boolean functions if this technique can be extended to logic operations), the long interconnect will require dynamic control of the guided plasmonic signal [35],[36]. Therefore, we demonstrate that dynamic control of spoof surface plasmon polariton modes in the THz frequency domain can be accomplished by using electro-optical control on a corrugated semiconductor structure. Furthermore, the slow light propagation enabled by the corrugated metallic gap structure can dramatically shift the resonant frequency at small refractive index changes. Thus, a powerful switching concept based on resonant frequency modulation can be applied to develop dynamic THz components such as switches and logic gates. The promising ability of the metamaterial is to localize terahertz pulse, providing a high extinction ratio and minaturize the THz switching components for large scale optical integration.

Finally, we design the metallic photonic crystal slab for a nanophotodiode which is useful to convert the optical signal to an electronic signal in very small plasmonic architecture. Specifically, we focus on the new architecture to enhance transmission at a specific frequency by using a one-dimensional periodic arrangement of cuts through corrugated slits. Furthermore, these thin film photonic behaviors can be significantly tailored by creating a photonic band structure, thus allowing us to obtain ultrfast and high sensitive photodectors.

1.2 Organization

Specifically, we study the following four different types of plasmonic interconnect structures in their thesis because they serve for coupling optical signals in three different ways.

1. Local plasmonic interconnect based on chain of metallic nano particles (MNP's): We develop closed-form mathematical equations and SPICE simulation models for a single MNP and then a plasmonic waveguide consisting of a chain of MNP's [37]. Specifically, a parabolic chain of MNP's can be utilized to couple SPP signals flowing through the MNP chain at optical frequency to a wider optical waveguide located at the focal point of the parabolic chain. Since the dimension of the metallic particles is comparable to the sizes of the CMOS electronic components, this SPP waveguide provides a simple mechanism to couple electronic signals to optical signals

2. Local plasmonic interconnect based on metallic nanowire (MNW): We develop an analytical methodology for establishing an equivalent circuit network of non-radiative surface plasmon (SP) energy transport along the metallic nanowire (MNW) [38]. We derive the SP dispersion and damping relation through a modified Bessel function electromagnetic (EM) field expansion which will lead to developing the low-pass transmission line (TL) model. Especially, the low pass TL parameters such as series impedance (Z) and shunt admittance (Y) can be calculated based on the

lumped element model and harmonic voltage (current) distribution. Furthermore, the equivalent circuit parameters such as resistance, inductance, capacitance and conductance are obtained by employing the finite difference (FD) discretization method such as T-cell RGLC networks. Finally, these equivalent circuit elements can be verified by using the HSPICE circuit simulation and 3D scattered finite time domain method (FDTD). Though the propagation length of SP signals on an MNW is in the range of 50 microns, MNW can be utilized to serve as a tapered waveguide to connect the micro-scale wide optical waveguide with nanoscale electronic components.

3. Global plasmonic interconnect and dynamic switch based on spoof surface plasmon polariton (SSPP): We explore artificially corrugated perfect conductor metamaterials with periodic arrays of grooves to propagate Tera Hertz (THz) signals by utilizing strongly localized spoof surface plasmon polariton (SSPP) modes [39]. Specifically, we incorporate electro-optical (EO) materials such as a nematic liquid crystal (N-LC) into the plasmonic gap to build a highly compact and efficient THz tri-state waveguide where the SSPP propagation can be switched ON and OFF by a low-voltage control-signal. The optimal design of the SSPP waveguide enabled by this novel method will demonstrate i) a strong sub-wavelength SSPP localization, ii) relatively high extinction ratio, and iii) small damping attenuation.

4. Photonic metamaterial crystal slab: We present a new design concept to increase the photo-generation rate in a small active domain by using sub-wavelength structures consisting of a surface plasmon photonic crystal slab (SPPCS) acting like a near field generator and an antireflection coating [40]. The polarizability of rectangular metallic cylinder predicts surface plasmon (SP) resonance frequency in the SPPCS photodiode. Thus, the enhanced near field intensity arising from SP resonant oscillation has the potential to solve the low photo-generation problem. In addition, the photonic band structure dramatically changes TM photonic maps with extraordinary transmission and low reflection, thereby leading to an efficient nano-photodiode.

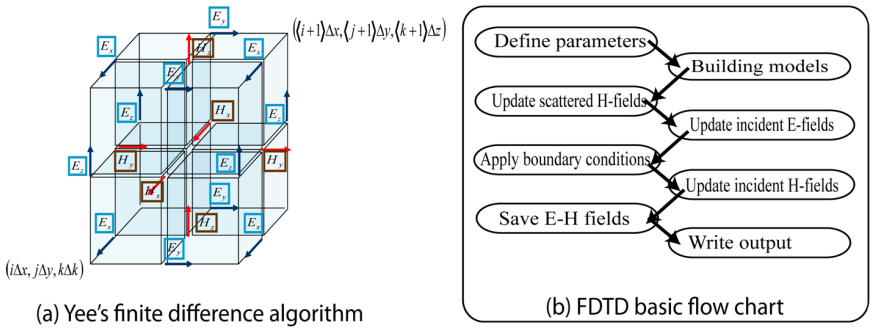

Figure 1.3: (a) Yee's finite difference algorithm, (b) FDTD basic flow chart

1.3 Numerical simulation methods

Development of the software for nanoscale plasmonic architectures requires the complex mathematical computation described by Maxwell equations. Furthermore, the plasmonic computer-aided design (CAD) enables us to calculate the electromagnetic phenomena subjected by nanoscale geometries consisting of different types of materials such as frequency-dependent, nonlinear and anisotropic materials. In addition, we can easily handle the plasmonic behaviors related to scattering, transmission, diffraction and polarization. Many standard numerical approaches such as frequency-domain, time-domain and eigensolver calculations can be applied to calculate the photonic behavior of plasmonic architectures. However, each numerical approach has own unique strength and weakness. Therefore, our plasmonic simulation methods are based on the two core algorithms depending on the Finite-Difference-Time-Domain (FDTD) and Rigorous-Coupled-Wave-Analysis (RCWA) because they are easier to implement and combine with parallel computing with minimal physical sacrifice.

1.3.1 Finite difference time domain method

First, we implement the finite difference time domain method (FDTD), in which we use a leap-frog algorithm and full wave vector representation as shown in Fig.1.3(a) [41],[42],[43]. Fig.1.3(b) shows the basic FDTD flow chart to calculate the E and H field in the scattered finite time domain simulation. Moreover, the FDTD method

allows us to calculate the SSPP dispersion relation, damping curve, quality factor Q and bandwidth for the performance of the plasmonics device. Specifically, we establish the scattered field FDTD implementation since this approach has some advantages over the total field FDTD formulation in that the dispersive calculation error of incident field is negligible and absorbing boundary condition of scattered field can be easily implemented. When developing the FDTD software, we experiment the promising applications such as surface plasmon resonance, metallic nanoparticles and metallic nanowire, nonlinear plasmonic materials and complex electromagnetic phenomena.

In this thesis, we focus on the scattered Finite Different Time Domain Formulation in Plasmonic Structures. Specifically, the total field is divided into two fields, namely, the incident field and scattered field, that is, $E_{tot}(r) = E_{inc}(r) + E_{scat}(r)$. To obtain the optical EM propagation in the plasmonic waveguide, we can not use constant parameters such as permittivity and susceptibility in the metallic structures. Since these parameters have different values corresponding to frequency, it is necessary to implement a frequency dependent model. It can be shown that the electric flux density in a metal can be described by:

$$D(r, w) = \epsilon_0 \epsilon_\infty E(r) + P(r) = \epsilon_0[\epsilon_\infty + \chi_e(r, \omega)]E(r) \tag{1.1}$$

Here, ϵ_0 is the free space permittivity, ϵ_∞ is the relative permittivity at $\omega = \infty$, $P(r)$ is the polarization vector and χ_e is the electric susceptibility. We use the Drude model to demonstrate the material response of a noble metal. The susceptibility of the Drude model is described by the following equation:

$$\chi_e(t) = \frac{\omega_p^2}{\nu_c}(1 - e^{-\nu_c t})S(t) \qquad \chi_e(\omega) = -\frac{\omega_p 2}{\omega(\omega + j\nu_c)} \tag{1.2}$$

Here, $\chi_e(t)$ is the time domain susceptibility, $\chi_e(\omega)$ is the frequency domain suscep-

tibility of Drude model and $S(t)$ is the unit step function. By using time domain susceptibility of the Drude model, we obtain the scattering FDTD field formulation

$$\nabla \times (H^{inc} + H^{scat}) = \sigma(E^{inc} + E^{scat}) + \omega_0 \omega_\infty \frac{[E^{inc} + E^{scat}]}{\partial t} + \omega_0 \frac{\partial}{\partial t}[(E^{inc} + E^{scat}) * \chi(t)] \tag{1.3}$$

This method gives the following numerical relationships between the electrical and magnetic fields in the scattered FDTD formulation.

$$\begin{aligned} E_x^{scatt,n+1}(j) = {} & \tfrac{\epsilon_\infty}{\frac{\sigma \triangle t}{\epsilon_0}\epsilon_\infty + \epsilon_\infty + \chi^0} E_x^{scatt,n}(j) + \tfrac{\epsilon_\infty}{\frac{\sigma \triangle t}{\epsilon_0}\epsilon_\infty + \epsilon_\infty + \chi^0} \textstyle\sum_{m=0}^{n-1} E_x^{scatt,n-m}(j) \triangle \chi^m \\ & + \tfrac{\triangle t}{(\frac{\sigma \triangle t}{\epsilon_0}\epsilon_\infty + \epsilon_\infty + \chi^0)\epsilon_0 \triangle y}[H_z^{N+1/2}(j+1/2) - H_z^{N+1/2}(j-1/2)] \\ & - \tfrac{\triangle t}{(\frac{\sigma \triangle t}{\epsilon_0}\epsilon_\infty + \epsilon_\infty + \chi^0)\epsilon_0 \triangle z}[H_y^{N+1/2}(j+1/2) - H_y^{N+1/2}(j-1/2)] \\ & - \tfrac{\triangle t}{(\frac{\sigma \triangle t}{\epsilon_0}\epsilon_\infty + \epsilon_\infty + \chi^0)} \tfrac{\partial}{\partial t}[E^{n+1} * \chi(t)] \\ & - \tfrac{\sigma \triangle t}{(\frac{\sigma \triangle t}{\epsilon_0}\epsilon_\infty + \epsilon_\infty + \chi^0)\epsilon_0} E_x^{inc,n+1}(j) \\ & - \tfrac{(\epsilon_\infty - 1)\Delta t}{(\frac{\sigma \triangle t}{\epsilon_0}\epsilon_\infty + \epsilon_\infty + \chi^0)\epsilon_0} E_x^{inc,n+1}(j) \end{aligned} \tag{1.4}$$

We use the recursive formation to evaluate the scattered electric field $\psi^n(i) = E_{scat}^n \Delta\chi^0 + \chi^{n-1}(i)\exp(-\nu_c \Delta t)$ where

$$\chi^m = \int_{m\Delta t}^{(m+1)\Delta t} \chi(\Lambda) d\Lambda \qquad \text{and} \qquad \Delta\chi^m = \chi^m - \chi^{m+1} \tag{1.5}$$

As in the case of the Drude model susceptibility, the Drude model recursive formulation can be described by:

$$\Delta\chi^m = -\frac{\omega_p^2}{\nu_c^2}(\exp(-m\nu_c\Delta t))(1 - \exp(-\nu_c \Delta t))^2 \tag{1.6}$$

For determination of the convolution of the incident wave, we use the sine incident

wave by using a complex quantity:

$$E^{inc}(t) = \exp(j\omega t - jk \cdot p) \tag{1.7}$$

Here, k is the wavevector of the incident wave and p is the point of calculation in the simulation domain. The convolution term is given by the following equation:

$$\frac{\partial}{\partial t}[E^{inc,n+1}(i) * \chi(t)] \tag{1.8}$$

With the complex sinewave, this convolution term is then given by:

$$\frac{\partial}{\partial t}[E^{inc,n+1}(i) * \chi(t)] = E_0 \exp(-jk \cdot p)\frac{\omega_p^2}{\nu_c}\frac{\partial}{\partial t}[\int_0^t 1 - \exp(-\nu_c \Lambda - \nu_c t + j\omega\Lambda)d\Lambda] \tag{1.9}$$

1.3.2 Rigorous coupled wave analysis

The RCWA has been the most widely used method for the accurate analysis of the diffraction of electromagnetic waves by periodic structures [44],[45],[46],[47]. Furthermore, it has been used successfully and accurately to analyze various periodic devices such as multiplexed holographic gratings, two-dimensional (2D) surface-relief gratings, and anisotropic gratings for both planar and conical diffraction. In addition, the RCWA method can be applied to calculate the analytical SSPP modes and dispersions including the multiple order terms (n > 0). Even though the theoretical analysis can be used to calculate the SSPP dispersion in simple periodic corrugated structures such as grating structure and metallic wire, the analytical method is highly limited to complex geometries and different grating structures. To solve these difficulties, we introduce more accurate solutions by using the rigorous coupled wave analysis (RCWA).

Moreover, the strength of this algorithm leads us to calculate accurate photonic

maps including reflection, transmission and absorption of the periodic plasmonic structure. Therefore, this approach can be applied to various plasmonic sensing applications such as plasmonic photodiodes, plasmonic biosensors and plasmonic metamaterial devices.

1.4 Original Contributions

The original contributions of the plasmonic research documented in this dissertation can be summarized as follows:

1. Derivation of an equivalent circuit modeling of a linearly equispaced MNPs plasmon wire using rigorous electromagnetic analysis (Chapter II : An Equivalent Circuit Modeling of an Equispaced Metallic Nanoparticles (MNPs) Plasmon Wire. IEEE TRANSACTIONS ON NANOTECHNOLOGY, 8(3):412-418, MAY 2009)

2. Derivation of a SPICE (simulation program with integrated circuit emphasis) circuit modeling of metallic nanowires (Chapter III : Equivalent Circuit Modeling of Nonradiative Surface Plasmon Energy Transfer Along the Metallic Nanowire. To be published : IEEE TRANSACTIONS ON NANOTECHNOLOGY)

3. Introduce a new terahertz switch using the perfect conductor metamaterial based on resonant frequency modulation (Chapter IV : Active Terahertz Spoof Surface Plasmon Polariton Switch Comprising the Perfect Conductor Metamaterial. IEEE TRANSACTIONS ON ELECTRON DEVICES, 56 (11, Sp. Iss. SI) : 2792-2799, NOV 2009)

4. Design a surface plasmon photonic crystal slab for an efficient nanophotodiode (Chapter V : One-Dimensional Surface Plasmon Photonic Crystal Slab (SPPCS) for a nanophotodiode. IEEE TRANSACTIONS ON NANOTECHNOLOGY, 9(4) : 470-473, Jul 2010)

CHAPTER II

An equivalent circuit modeling of an equispaced metallic nanoparticles plasmon wire

2.1 Introduction

In this chapter, we focus on rigorous way to develop the equivalent circuit modeling of a MNP and an equispaced linear MNPs array based on the electric dipole moment (EDM)[37]. First, to develop the inductance and capacitance elements, the internal oscillation energy and EM near-field energy can be calculated based on the EDM. Second, to describe the resistance elements and the applied signal, four main power flows including relaxation loss, radiation outflow emission, host matrix coupling, and applied signal interaction are calculated by using the rigorous EM analysis. Third, the conservation of energy law leads to computation of the relaxation, radiation, and surrounding matrix damping frequency. Fourth, the resonant behavior of SP modes in a single MNP is represented by a lumped SP resonant circuit model. The lumped resonant circuit parameters such as capacitance, inductance, and conductance are calculated by using the equation of motion of the EDM, electric potential, and EM nearfield energy. Finally, nanoelements of a MNP are extensible to the equivalent circuit modeling for a closely equally spaced MNPs array as a voltage-controlled voltage source (VCVS) by using the SP couplings between MNPs. Furthermore, these

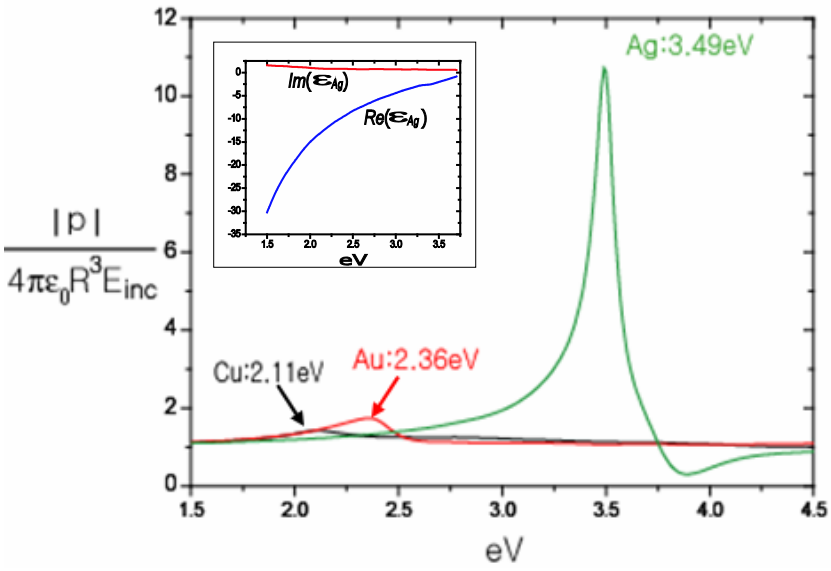

Figure 2.1: Nondimensional EDM $|p|/(4\pi\epsilon_0 R^3 E_{inc})$ as a function of photon energy. These curves are obtained from the cubic spline method by using the Johnsons experimental optical data of three different noble metals: Cu, Au, and Ag.

calculations not only give a qualitative understanding about SP modes originating from a single MNP, but also provide the physical intuition of the complex physical phenomena occurring in the MNPs waveguide.

2.2 EDM of a spherical MNP

In a spherical MNP waveguide, the first spherical MNP along the chain is optically irradiated by a near-field generator such as NSOM (near-field scanning optical microscope) or optical input system such as far and near field conversion structure [48], [49]. Since the wavelength of light is large compared to the geometry of particles, the validity of uniform EM field is reasonable and the electric charge distribution produces the coherent EDM. Especially, in the nanoscale domain, SP modes generate an EM dipole field. In order to evaluate the EDM and account for strong EM absorption at the optical spectrum, we assume that uniform EM wave applies to spherical MNP

and produces the electron cloud oscillation. Under these assumptions, the EDM of the MNP can be described by

$$p = 4\pi\epsilon_0 R^3 \left(\frac{\epsilon_r(\omega) - 1}{\epsilon_r(\omega) + 2} \right) E_{inc} \tag{2.1}$$

where R is the radius of an MNP and $\epsilon_r(\omega)$ is the dielectric response. Fig. 2.1 shows the nondimensional EDM $|p|/(4\pi\epsilon_0 R^3 E_{inc})$ by using the Johnsons experimental data of three different noble metals such as Cu, Au, and Ag [50]. In addition, the complex dielectric constant $\epsilon_r(\omega) = \epsilon_{re}(\omega) + j\epsilon_{im}(\omega)$ is obtained from the cubic spline regression method, as shown in inset of Fig. 2.1. As can be seen, three noble metals have different magnitude of the EDM, Cu (1.422), Au (1.739), and Ag (10.72), with different resonant frequencies: Cu (2.11 eV), Au (2.36 eV), and Ag (3.49 eV). In general, these Lorentzian behaviors can be explained by using the Drude model approximation. The complex dielectric of noble metals can be described by the Drude model

$$\epsilon_r(\omega) = 1 - \frac{\omega_p^2}{\omega(\omega + j\gamma)} \tag{2.2}$$

where $\omega_p = \sqrt{n_e e^2/\epsilon_0 m_e}$ is the bulk plasma frequency and γ is the relaxation damping frequency. It follows from the previous equations that the EDM can be written as

$$p = 4\pi\epsilon_0 R^3 \frac{-\omega_p^2}{3\omega(\omega + j\gamma) - \omega_p^2} E_{inc} \tag{2.3}$$

From (2.3), the resonant frequency can be calculated as

$$\omega_o = \sqrt{\frac{\omega_p^2}{3} - \frac{\gamma^2}{2}} \tag{2.4}$$

However, in the case of the MNP, because the bulk plasma frequency (ω_p) is about ten times higher in magnitude than the relaxation frequency (γ) [50], the relaxation damping frequency effect on the resonance frequency is almost negligible. Therefore,

the resonant frequency is almost equal to $\omega_o = \sqrt{1/3}\omega_p$. However, the Lorentzian line shape with FWHM depends on bulk plasma frequency (ω_p) and relaxation damping frequency (γ). For instance, as shown in Fig. 2.1, Ag with high bulk plasma frequency (ω_p) and low relaxation frequency (γ) generates the localized EM field enhancement compared to other noble metals such as Au and Cu.

2.3 Internal oscillation energy and EM near-field energy

To demonstrate inductance and capacitance of the MNP, it is necessary to calculate the internal oscillation energy and EM near-field energy in that internal oscillation energy gives the equation of motion of SP modes, and EM near-field energy allows us to calculate the energy of the capacitance element. First, in order to calculate the internal oscillation and EM near-field energy, we begin to examine the basic physical mechanism of SP mode in the MNP. Inside the MNP, light creates an electron gas displacement with respect to positive-ion charge. The surface charge polarization generates an electric field that acts as the restoring force inside the MNP. Thus, this harmonic oscillatory motion is analogous to simple mechanical motion, which is described by the spring constant and the relative displacement from the equilibrium position. The spring constant and resonant frequency of electron clouds can be calculated by an internal electric field inside the MNP. Accordingly, the internal oscillation energy of electron density of the MNP can be described in terms of the EDM

$$H_o = \frac{1}{2}\frac{m_e}{Ne^2}\left(\frac{dp}{dt}\right)^2 + \frac{1}{2}\frac{m_e\omega_o^2}{Ne^2}p^2 \tag{2.5}$$

where the first term denotes the kinetic energy, the second term describes the potential energy, $p = \int x^{'}\rho(x^{'})d^3(x^{'})$ is the EDM, ω_o is the resonant oscillation frequency, N is the number of electrons, and m_e is the optical electron mass. Note that $N = 4\pi R^3\rho/3$, where ρ is is the electron gas concentration and R is the radius of the MNP.

However, in contrast to a uniformly polarized infinite dielectric slab, the spherical surface charge distribution with axial symmetry produces the near-field EM energy outside the MNP. To calculate the near-field EM energy,we make two assumptions: 1) almost all EM energy density can be generated by the EDM because particle dimensions are small compared to the wavelength of oscillation frequency and 2) the surrounding medium is linear dispersive with small attenuation coefficient and frequency-independent permittivity. With two assumptions, the electric field in the near-field zone ($kr \ll 1$) can be calculated by the localized oscillating system [17]

$$E(r,t) = \frac{1}{4\pi\epsilon r^3}[3\overrightarrow{e_r}(\overrightarrow{e_r} \cdot \overrightarrow{p}) - \overrightarrow{p}] \tag{2.6}$$

where ϵ is the permittivity in the surrounding matrix, $\overrightarrow{p} = p(r)\cos(\omega_o t)\overrightarrow{e_z}$ is the EDM inside the MNP, and $\overrightarrow{e_r}$ is a unit vector in the radial direction. And, the effective EM energy can be described by the Poyntings theorem

$$\frac{1}{2}\left[\frac{d(\omega\epsilon)}{d\omega}\right]\langle E(r)\cdot E(r)\rangle \approx \frac{1}{2}\langle E(r)\cdot E(r)\rangle \tag{2.7}$$

Therefore, the near-field EM energy outside the MNP can be obtained by integrating over the whole volume outside the particle

$$E_N = \frac{\epsilon}{2}\int_R^\infty \int_0^{2\pi} \int_0^\pi E(r)\cdot E(r) r^2 sin\theta d\theta d\phi dr \tag{2.8}$$

The near-field EM energy can be expressed in terms of the EDM

$$E_N = \frac{1}{12}\frac{p^2}{\pi\epsilon R^3} \approx \frac{1}{24}\frac{|p|^2}{\pi\epsilon R^3} \tag{2.9}$$

where $|p| = \sqrt{\overrightarrow{p}^* \cdot \overrightarrow{p}}$ means the magnitude of the EDM. The term is responsible for dispersion relationship, optical force, and EM energy transfer along the MNP

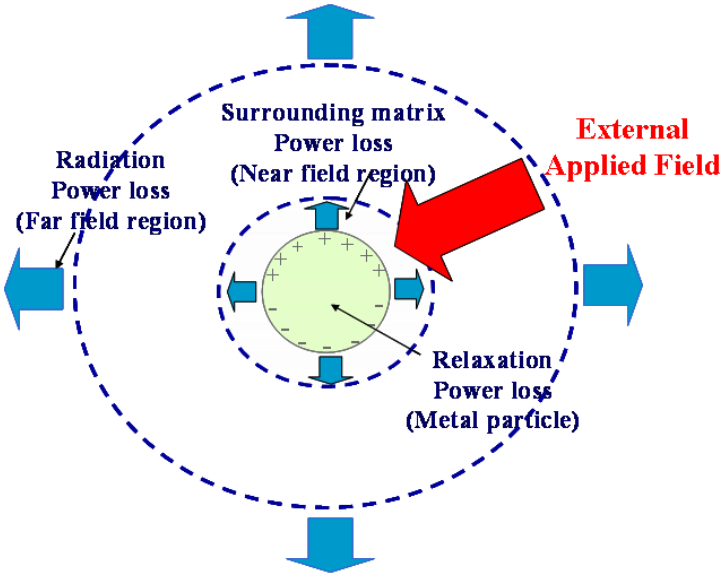

Figure 2.2: For the oscillatory SP modes in an MNP, energy dissipation mechanisms such as relaxation (inside MNP), radiation energy outflow (far-field region), and surrounding matrix power loss (near-field region) are existed in three different regions.

waveguide

2.4 Power flow calculation of a spherical MNP

In this section, we now focus on resistance elements and the applied current signal. The resistance elements and the applied current signal are strongly related to power flows. In the case of resistance elements, there exist dissipative power flows because of three main possible mechanisms, including electron clouds relaxation [51], radiation energy outflow [52], and resonant surrounding matrix coupling [52] in the three different domains, as shown in Fig. 2.2. Assuming that relaxation collision damping force is proportional to the derivative of the electric charge displacement, the damping force for electron clouds inside the MNP can be described by

$$F_D = M_e \gamma \frac{dx}{dt} \tag{2.10}$$

where γ denotes the relaxation damping coefficient. Therefore, the relaxation damping power loss per unit time can be written as follows in terms of the EDM:

$$\frac{dW_D}{dt} = \frac{M_e \gamma}{Ne^2} \left[\frac{dp}{dt}\right]^2 \tag{2.11}$$

In the case of the radiation damping loss, this damping mechanism is the emission of EM power flow outside the nanoparticle. Since the radiation pattern is similar to the dipole field distribution, radiation power depends on the dipole plasmon mode. The electric dipole field in the far-field region ($kr \gg 1$) is given by

$$E(r,t) = \frac{vk^2 Z}{4\pi}([e_r \times p] \times e_r)\frac{e^{ikr}}{r} \tag{2.12}$$

The Poynting vector allows us to calculate the radiation power as follows:

$$\frac{dW_R}{dt} = \frac{v^2 Z k^4 |p|^2 \sin^2(w_o t - r/v)}{6\pi} \tag{2.13}$$

where $v = c/n$ is the EM velocity, $Z = (\epsilon/\mu)^{1/2}$ is the impedance in the surrounding matrix, and k is the EM wavenumber. If we ignore the retarded time-delay phase difference ($r/v \approx 0$) and assume the perfect harmonic oscillator model $p(r,t) = p(r)\cos(w_o t)$ because the damping decay rate is very small compared to the oscillation frequency, the radiation power loss can be approximately obtained in terms of the rate of change of momentum:

$$\frac{dW_R}{dt} = \frac{v^2 Z k^4}{6\pi w_o^2} \left(\frac{dp}{dt}\right)^2 \tag{2.14}$$

The last decay mechanism is the EM resonant coupling interaction with the surrounding matrix. In the actual dispersive nonmagnetic media such as silicon-based material, EM energy may be dissipated into the surrounding matrix. This dissipated

power loss per unit time can be calculated as follows [17]:

$$\frac{dW_M}{dt} = w_o \epsilon_0 Im\chi(w_0) \langle E(r) \cdot E(r) \rangle \tag{2.15}$$

where w_o is the oscillation frequency and $Im\chi(w_o)$ denotes the imaginary susceptibility in the surrounding matrix. Therefore, the absorbed energy in the host matrix per unit time is calculated

$$\frac{dW_M}{dt} \approx \frac{w_o \epsilon_0 Im\chi(w_o) p}{6R^3 \pi \epsilon_{re}^2} \approx \frac{\epsilon_0 Im\chi(w_o)}{6R^3 \pi \epsilon_{re}^2 w_0} \left(\frac{dp}{dt}\right)^2 \tag{2.16}$$

Finally, the EM field of the applied signal interacts with electron clouds in the MNP, as shown in Fig. 2.2. This interaction between the applied signal and electron clouds produces the external force in the MNP

$$F = -NeE_I \tag{2.17}$$

where E_I means the electric field of the applied signal. The power flow of the applied signal per unit time can be calculated in terms of the EDM

$$\frac{dW_A}{dt} = -E_I \frac{dp}{dt} \tag{2.18}$$

2.5 Extended oscillatory equation motion of a spherical MNP

To obtain the equation of motion of SP modes in a single MNP, the time derivative of internal oscillation energy in the MNP is equal to power flow due to the relaxation, radiation, surrounding matrix, and applied signal

$$\frac{d}{dt}(H_o) = -\frac{dW_D}{dt} - \frac{dW_R}{dt} - \frac{dW_M}{dt} + \frac{dW_A}{dt} \tag{2.19}$$

The extended oscillatory equation of motion including all damping mechanisms in the MNP can be described by

$$p'' + (\gamma + \gamma_R + \gamma_M)p' + \omega_o^2 p = -\frac{Ne^2}{m_e} E_I. \tag{2.20}$$

where γ_R is the radiation damping frequency and γ_M is the surrounding damping matrix. The radiation damping frequency is given by

$$\gamma_R = \frac{2\rho e^2 v^2 Z k^4 R^3}{9 m_e w_o^2} \tag{2.21}$$

where $Z = (\epsilon_0/\mu)^{1/2}$ is the impedance in the air matrix. And, the matrix damping frequency is also determined by

$$\gamma_M = \frac{2\rho e^2 Im\chi(\omega_o)}{9 m_e \epsilon_{re}^2 w_o} \tag{2.22}$$

It follows from (2.21) and (2.22) that radiation damping frequency (γ_R) depends on the particle size, SP oscillation frequency, and metal physical properties, whereas matrix damping frequency (γ_M) relies on the optical properties of the surrounding matrix, SP oscillation frequency, and metal physical properties. To obtain radiation damping frequency, we choose Ag particles with different radii because the radiation frequency relies on the particle size. For this calculation, we have used electron concentration $\rho_{Ag} = 5.85 \times 10^{28}/m^3$ and an electron mass $m_{Ag} = 8.745 \times 10^{-31} kg$ for Ag . The surrounding matrix is chosen to be SiO_2 with small attenuation coefficient $\alpha \sim 3/m$ and the refractive index $n \sim 1.56$ under the assumption of an isotropic medium in the optical regime. For maximum EDM, we use the resonant oscillation frequency $\omega_o = 5.302 \times 10^{15} rad/s$, as shown in Fig. 2.1. For these parameters, we calculate the imaginary susceptibility $Im\chi(\omega_o) \sim n\alpha c/\omega_o = 2.546 \times 10^{-7}$ and the surrounding matrix damping frequency $\gamma_M = 3.49 \times 10^8 rad/s$. Fig. 2.3 shows

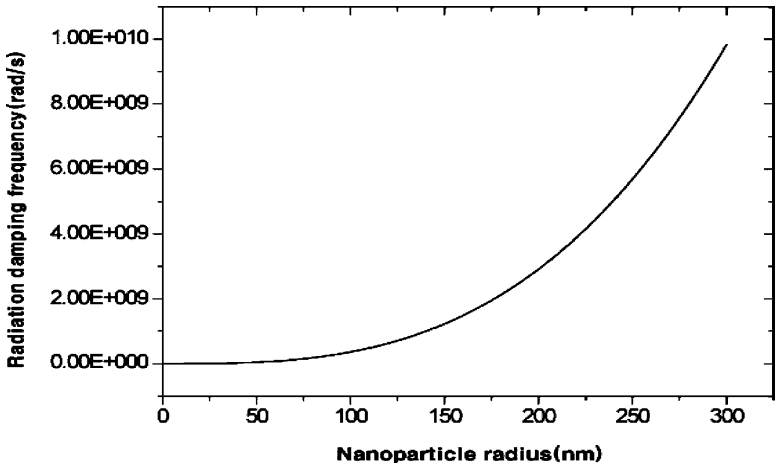

Figure 2.3: Radiation damping frequency (γ_R) can be calculated corresponding to different radii. This calculation is performed for Ag.

the radiation frequency corresponding to the radius of MNP. Radiation damping frequency (γ_R) is almost equal to the value of $2.91 \times 10^9 rad/s$ for 200 nm radius. Therefore, in the case of resonant oscillation mode with small radius MNP and small attenuation coefficient of the surrounding matrix, radiation and surrounding matrix damping frequency are negligible compared to relaxation damping frequency since relaxation damping (γ) has the order of $10^{14} rad/s$. However, the radiation damping (γ_R) can be an important factor in the event of high oscillation frequency and large particle dimension, whereas the matrix damping frequency can be a significant factor in a poor host matrix with large attenuation coefficient.

2.6 Nanocircuit elements of a MNP

The SP resonant behavior of a MNP can be modeled as a lumped resonant circuit, as shown in Fig. 2.4. The circuit equation for the lumped resonant circuit is given by

$$\frac{d^2v(t)}{dt^2} + \frac{G}{C}\frac{dv(t)}{dt} + \frac{1}{LC}v(t) = \frac{1}{C}\frac{di}{dt} \tag{2.23}$$

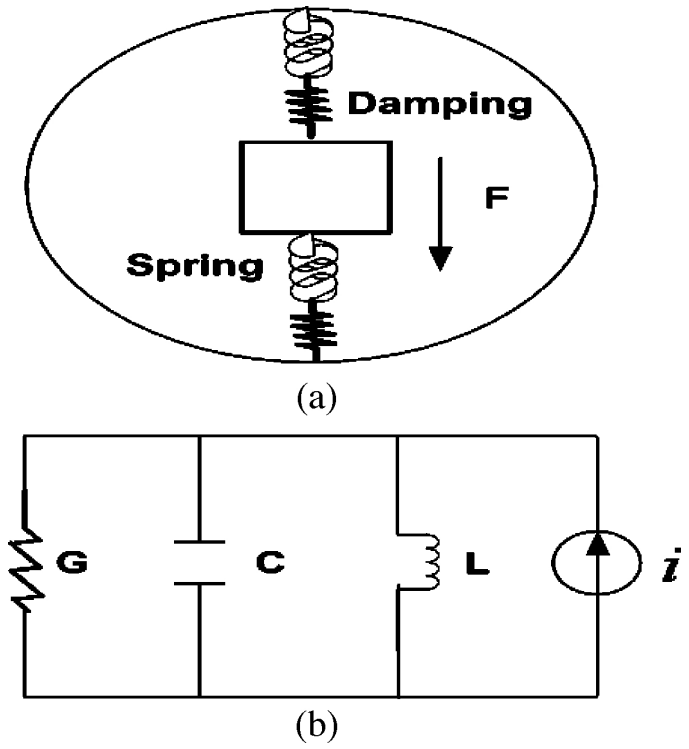

Figure 2.4: Equivalent models for a plasmonic MNP. (a) Mechanical spring-mass-damping model. (b) Lumped resonant circuit model.

where $v(t)$ represents the equivalent current voltage, and C, L, and G denote capacitance, inductance, and conductance, respectively. In the spherical MNP, the average electric potential can be written in terms of the EDM. The average electric potential around the MNP can be calculated by integration of the internal electric field. In general, the symmetric charge configuration of a hemispherical region gives the average potential as follows:

$$v_{avg} = -\frac{4R}{3}E_{int} = -\frac{p}{\pi R^2(\epsilon - \epsilon_0)} \tag{2.24}$$

where $E_{int} = 3\epsilon E_I/(\epsilon + 2\epsilon_0)$ denotes the internal electric field inside the MNP [10]. Therefore, the equation of motion in the lumped resonant circuit can be described in terms of the EDM:

$$\frac{d^2p}{dt^2} + \frac{G}{C}\frac{dp}{dt} + \frac{1}{LC}p = \frac{-\pi R^2(\epsilon - \epsilon_0)}{C}\frac{di}{dt} \tag{2.25}$$

Table 2.1: NANOCIRCUIT ELEMENTS OF THREE NOBLE MNPS (RADIUS R = 20 NM) THAT IS SURROUNDED BY A FREE SPACE WITH A REFRACTIVE INDEX $n = 1$

	Cu	Au	Ag
eV(resonance)	2.11	2.36	3.49
ω_o (rad/s)	3.206e15	3.585e15	5.302e15
ϵ	-7.262+j3.460	-4.261+j2.435	-2.068+j0.279
γ (rad/s)	1.449e14	1.075e14	3.226e13
C	7.439af	3.124af	0.880af
L	13.08fH	24.91fH	40.43fH
G	1.078mS	0.339mS	0.0283mS

It has been shown that three related equations between the lumped element model and the extended equation of motions of the EDM can be established by connecting (2.20) and (2.25) as follows:

$$\frac{G}{C} = \gamma + \gamma_R + \gamma_M = \gamma_T \qquad \frac{1}{LC} = \omega_o^2 \qquad \frac{Ne^2}{m_e} E_I = \frac{\pi R^2 (\epsilon - \epsilon_0)}{c} \frac{di}{dt} \tag{2.26}$$

There are four lumped unknown parameters (G, C, L, i) and three related equations between the lumped circuit model and the equation of motion of the MNP. Therefore, to determine all circuit parameters, it is necessary to set up one additional relation. In the optical spectrum, the metallic structures have the negative permittivity that can be described by the inductance (L), and surrounding material has the positive permittivity that can be presented by the capacitance (C) [53],[54]. Therefore, the stored energy in the capacitance element in the lumped resonant circuit is almost equal to the EM near-field energy outside MNP

$$U_C = \frac{1}{2} C v_{avg}^2 \approx \frac{1}{4} C |v_{avg}|^2 = \frac{1}{24} \frac{|p|^2}{\pi \epsilon_0 R^3} \tag{2.27}$$

The capacitance of a MNP is given by

$$C = \frac{\pi R |\epsilon - \epsilon_0|^2}{6 \epsilon_0} \tag{2.28}$$

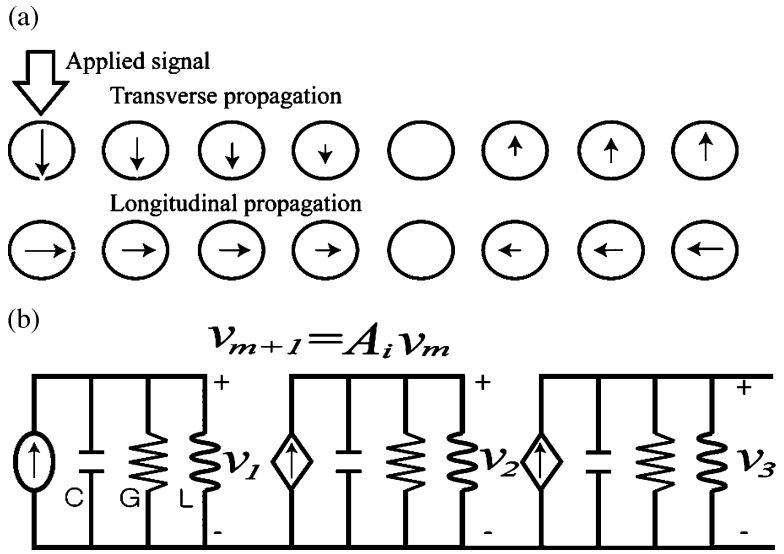

Figure 2.5: (a) Two fundamental coupled oscillations of a plasmon wire: longitudinal oscillations and transverse oscillation. (b) Equivalent circuit modeling for MNPS plasmon wire as a VCVS.

Table I shows C, L, and G components for three different noble MNP (radius 20 nm) at three different resonant frequencies, which is surrounded by a free space with a refractive index $n = 1$. To calculate nanocircuit components, the relaxation damping frequency (γ) is taken from the Johnsons data [18]. As can be seen, compared with Cu and Au, Ag has high inductance and small conductance for efficiently sending SP along the MNPs. At resonant frequency $\omega_o = 5.302 \times 10^{15} rad/s$, the permittivity of Ag has the value of $(-2.068 + j0.279)\epsilon_0$ obtained by Johnson's experimental optical data [18]. Let us assume the spherical MNP with $R = 20$ nm. Equations (2.26) and (2.28) show that the circuit parameters of Ag of the MNP has the value of $C = 0.880$ aF, $L = 40.43$ fH, and $G = 0.0283$ mS.

2.7 Equivalent circuit of MNPs plasmon wire

The subwavelength energy transfer along a closely equispaced MNPs plasmon wire with spatial distance d can be modeled by using the nanoelements of the MNP. As can be seen in Fig. 2.5, the first MNP of the plasmon wire is illuminated by a

laser, thus coupled SP modes can be transported along the MNPs array. From the point of the antenna theory, near field produced by mth dipole antenna is received by identical (m - 1)th and (m + 1)th dipole antennas respectively; near field from (m + 1)th dipole accordingly transmits mth and (m + 2)th dipole antennas. In addition, the efficiency of receiving antenna is also determined by the orientation between the receiving dipole antenna and transmitting dipole antenna. The fundamental orientations of dipole antenna in Fig. 2.5(a) indicate that there are two kinds of SP coupled modes: longitudinal coupled modes where dipole moments are along the propagation direction and transverse coupled modes where dipole moments are perpendicular to the axis of the array. Depending on the polarization orientation, the E-field received by the mth dipole antenna from the nearest SP coupling is given by using (2.6):

$$E_{p,m} = \frac{\mu_i p_{m+1}(t)}{4\pi\epsilon_0 n^3 d^3} + \frac{\mu_i p_{m-1}(t)}{4\pi\epsilon_0 n^3 d^3} \tag{2.29}$$

where μ_i is the polarization constant for which μ_L = -2 and $\mu_T = 1$, p_m is the EDM of the mth MNP, n is the refractive index of the matrix, and d is the distance of an equally spaced linear array. The equation of motions of the mth ($m \gg 2$) MNP can be obtained by using the nearest EDM interaction

$$p''_{i,m} + \gamma_T p'_{i,m} + \omega_o^2 = -\mu_i \omega_c^2 (p_{i,m-1} + p_{i,m+1}) \tag{2.30}$$

where the SP coupling frequency will be

$$w_c^2 = \frac{Ne^2}{4\pi\epsilon_0 n^3 d^3 m_e} = \frac{\rho R^3 e^2}{3\epsilon_0 n^3 d^3 m_e} s \tag{2.31}$$

The propagating wave solution to (2.30) have the following form [20]:

$$p_{i,m} = p_{i,m-1} exp(-\alpha d + j(\omega t \pm kd)) \tag{2.32}$$

where p_{m-1} and p_m are the EDM of $(m-1)$th and mth MNP, respectively, and α is the damping constant per unit length. Substituting (2.32) into (2.30) yields

$$w\gamma_T + 2\mu_i\omega_c^2 \sin(kd)\sinh(\alpha d) \tag{2.33}$$

$$w^2 = w_c^2 + 2\mu_i w_c^2 \cos(kd)\cosh(\alpha d) \tag{2.34}$$

For $\alpha d \ll 1$, attenuation constant is approximately given by

$$\alpha_i = \frac{\gamma_T \omega}{2|\mu_i| d \sin(kd)\omega_c^2} \tag{2.35}$$

where α_T and α_L are the transverse and longitudinal damping factor, respectively. At the resonance frequency ($\omega = \omega_o$), the wavenumber condition should be satisfied

$$kd = \frac{\pi}{2} \tag{2.36}$$

Since the voltage of the mth MNP can be calculated by the EDM of the mth MNP

$$v_m(t) = -\frac{p_m(t)}{\pi R^2(\epsilon - \epsilon_0)} \tag{2.37}$$

The parameter that relates v_m and v_{m-1} is the MNP plamson wire $A_i = v_m/v_{m-1}$

$$\mid \frac{A_m}{A_{m-1}} \mid = \exp(-\alpha_i d) \tag{2.38}$$

Fig. 2.5(b) shows the equivalent circuit model for the closely linear MNPs plsmon wire as a VCVS with voltage gain A_i . Thus, voltage gain (A_i) has magnitude

$$\mid \frac{A_m}{A_{m-1}} \mid = \exp(-\alpha_i d) \tag{2.39}$$

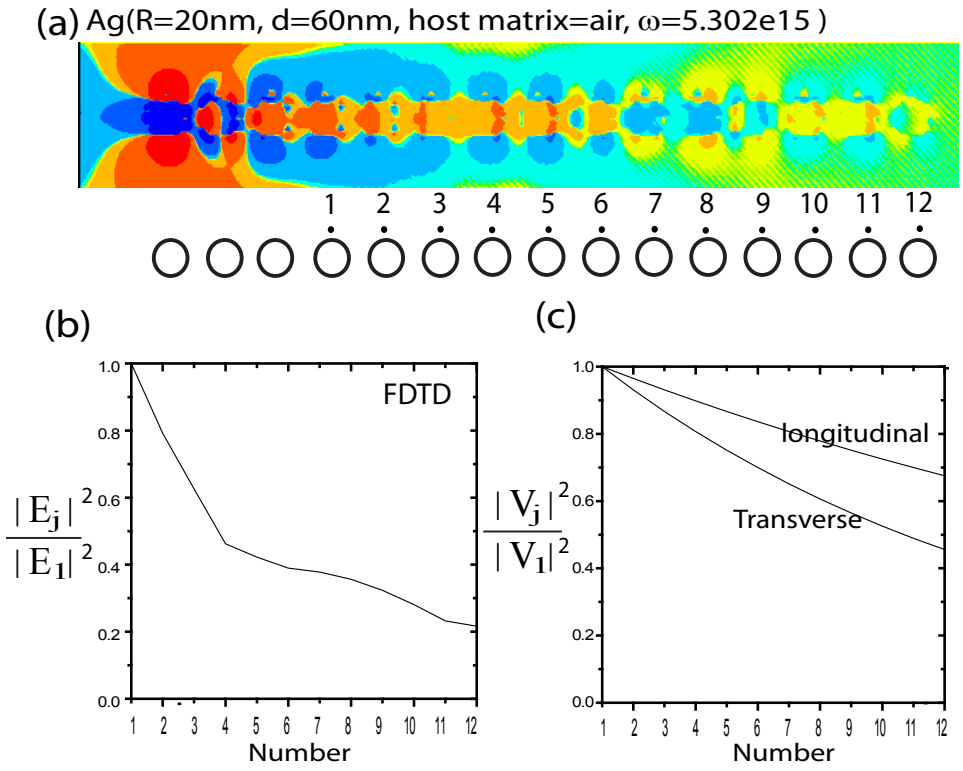

Figure 2.6: (a) Time snapshots of z component (in the xy plane) of scattered electric field in the Ag plasmon wire. (b) Average E-field density in the Ag MNPs plasmon wire is obtained by FDTD simulation. Values are calculated at the identical positions of each MNP, and E-field densities are normalized to the E-field density of position 1. (c) Average voltage of the Ag plasmon wire is calculated by Ag circuit parameters. The voltages of MNPs plasmon wire at different positions are normalized to the voltage of position 1.

Table 2.2: EQUIVALENT CIRCUIT PARAMETERS OF THREE NOBLE MNPS PLASMON WIRE (RADIUS R = 20 NM) SEPARATED BY A SPATIAL DISTANCE (d = 60 NM) AT THREE DIFFERENT RESONANT FREQUENCIES, WHICH IS SURROUNDED BY A FREE SPACE WITH A REFRACTIVE INDEX $n = 1$

	Cu	Au	Ag
eV(resonance)	2.11	2.36	3.49
ω_o (rad/s)	3.206e15	3.585e15	5.302e15
ω_c(coupling frequency)	1.508e15	1.530e15	1.547e15
α_T(transverse damping)	1.702e6/m	1.379e6/m	5.956e6/m
α_L(longitudinal damping)	8.512e5/m	6.859e5/m	2.978e5/m
exp(-α_Td)	0.9209	0.9631	0.9649
exp(-α_Ld)	0.9502	0.9597	0.9829

Table II gives the equivalent circuit parameters including coupling frequency ω_c , attenuation factor α, voltage gain $\exp(-\alpha d)$ for three different noble MNP's (radius $R = 20$ nm) array with the spatial distance ($d = 60$ nm) at three different resonant frequencies, which is surrounded by a free space with a refractive index $n = 1$.

To demonstrate the validity of our equivalent circuit parameters, we have conducted 3-D scattered finite-difference time-domain (FDTD) simulation. Fig. 2.6(a) plots the EM energy transfer in Ag plasmon wire with radius 20 nm and distance 60 nm. For realizing a resonant SP subwavelength transfer along the plasmon wire, the incident plane wave ($\omega_o = 5.302 \times 10^{15}$ rad/s), polarized parallel to the longitudinal axis of the wire, irradiates at the first MNP. Accordingly, we obtain the average E-field density at different locations from position 1 to position 12. Values are calculated at the identical positions located at the 30 nm offset points (z-directed) from the center of MNPs, and E-field densities are normalized to the E-field density of position 1. In addition, Fig. 2.6(c) shows the voltage attenuation based on Table II. As shown in Fig. 2.6(b) and (c), the FDTD calculation, from position 1 to position 3, provides strong damping coefficient compared to equivalent circuit modeling because we ignore higher order electric moments with small SP interaction compared to EDM coupling. However, FDTD simulation, after position 3, shows that attenuation

coefficient is closely similar to the voltage attenuation since the SP energy transfer along the MNPs plasmon wire is transported by strong EDM coupling, as plotted in Fig. 2.6(a), thus validating our equivalent circuit modeling.

2.8 Conclusion

To calculate the MNP nanocircuit elements, the theoretical SP physical mechanism of the single MNP has been demonstrated. As described in previous sections, the spherical MNP has a lot of advantages over any other plasmonic structures in that they demonstrate optical selectivity (FWHM), an SP modes resonator, and an effective near-field EM generator. Furthermore, instead of full-wave computation-intensive FDTD simulation, the lumped element circuit model of the MNPs plasmon wire offers us fast system-level simulation models such as SPICE to investigate the behavior of the SP modes in MNPs in the presence of conventional electronic components. Therefore, we can efficiently analyze complex MNPs structure combined with photonic and electric elements by using the equivalent circuit modeling.

CHAPTER III

An equivalent circuit modeling of a metallic nanowire

3.1 Introduction

In this chapter, we focus on the rigorous way to present the equivalent circuit elements of the metallic nanowire (MNW). To establish nonlinear circuit block of SP modes along the MNW, we have used to physical approach to define nonlinear equivalent circuit elements (R, L, C and G) are capable of mimicking SP behaviors such as SP dispersion relation $k(\omega)$, damping curves $\alpha(\omega)$ and power flow $P(\omega)$. To demonstrate the equivalent circuit elements of SP MNW based on physical approach [55],[56], we need to develop the physical equation formulations. First, we investigate the dispersion relation and damping curve of non-radiative SP waves along the MNW by using Newton-Raphson algorithm. We can gain an intuitive understanding of the low pass TL model by investigating the SP dispersion relation. For instance, in the conventional TL model, the per-unit-length (PUL) circuit parameters are derived from the integral of Maxwell's equation. However, contrary to the conventional TL approach, our circuit elements are based on the dispersion relation and damping curve because the propagation constant is determined by PUL circuit elements : $\alpha + jk = \sqrt{(r + j\omega l)(g + j\omega c)}$ where r, l, g and c denote resistance per unit length,

inductance per unit length, conductance per unit length and capacitance per unit length. Second, to be complete description of all circuit parameters, the current (I) and voltage (V) should be described as the physical quantity. For example, in the transmission line analysis, the EM fields of a TEM satisfy a static field distribution in a transverse plane, thus voltage and current are uniquely defined as a transverse plane based on the integration of E or H fields. However, because the SP modes generate TM modes, we have used the net power flow concept to obtain effective characteristic impedance ($Z_c = V/I$) in analogy with the calculation of radiation impedance for an antenna. In this way, we can calculate the effective voltage as a physical meaning. Especially, among many SP propagation modes, we focus on the dominant TM propagation mode (n=0) with no surface charge variation in the direction, thus easily obtaining the effective current and effective voltage along the MNW. Furthermore, the lumped element model and time-harmonic current (or voltage) distribution lead us to calculate the low pass transmission parameters such as series impedance (Z) and shunt admittance (Y). Thirdly, the FD (finite difference) methods such as T-cells, π-cells and half-cells enable us to obtain the equivalent circuit parameters of MNW: resistance (R), capacitance (C), inductance (L), or conductance (G). Fourthly, these equivalent circuit parameters of the MNW are validated by HSPICE and FDTD simulation. Finally, we develop the equivalent circuit networks for the parallel MNWs.

3.2 Dispersion relation and damping curve of surface plasmon in the MNW

In the case of flat metallic surface, the SP dispersion can be calculated by solving the Maxwell equations. In detail, this relationship is given by the following well-known formula [57]:

$$k_{sp} = k_f \sqrt{\frac{\epsilon_s \epsilon_m}{\epsilon_s + \epsilon_m}} \tag{3.1}$$

where $k_f = \omega/c$ is the free space wave-vector, ϵ_s is the permittivity of the surrounding material and ϵ_m is the frequency dependent permittivity of the metallic structure. However, in order to calculate the SP dispersion in the MNP, we shall consider the sub-wavelength cylindrical structures with a cross-section of radius R_0 ($R_0 \ll \lambda$) in the longitudinal z axis, transverse r and θ plane. In the case of subwavelength circular geometry, we assume that non-radiative near field energy is transported along the z direction and phase constants of r and θ are imaginary because EM wave satisfies the Heisenberg uncertainty principle ($\triangle x \triangle p > \hbar$). Furthermore, unlike a conventional optical waveguide, the SP modes are purely transverse magnetic (TM) modes because the surface charge generates a transverse magnetic field at the interface between a metal structure and a surrounding matrix. Therefore, the non-radiative EM fields in the metal core ($r < R$) are given by as follows [8]:

$$E_{z1} = AI_n(k_{\rho 1}r), \quad E_{r1} = A\frac{ik_z}{k_{\rho 1}}I_{n+1}(k_{\rho 1})$$
$$H_{\theta 1} = A\frac{i\omega\epsilon_1}{k_{\rho_1}}I_{n+1}(k_{\rho_1}r) \tag{3.2}$$

and EM fields in the host matrix ($r > R$) are

$$E_{z1} = BK_n(k_{\rho 1}r), \quad E_{r1} = -B\frac{ik_z}{k_{\rho 1}}K_{n+1}(k_{\rho 1})$$
$$H_{\theta 1} = -B\frac{i\omega\epsilon_2}{k_{\rho_2}}K_{n+1}(k_{\rho_2}r) \tag{3.3}$$

where $k_{\rho_i} = \sqrt{k_z^2 - \epsilon_i\mu\omega^2}$, i=1, 2 are transverse phase components, I_n and K_n are the n^{th} order exponential growth and decaying functions for the modified Bessel equation, R is the radius of MNW. From boundary conditions with tangential electric-magnetic (EM) field components continuity, one-dimensional SP transcendental equation can be obtained:

$$\frac{K_n(k_{\rho_2}R)}{I_n(k_{\rho_1}R)} = \frac{-\epsilon_2 k_{\rho 1}K_n(k_{\rho_2}R)}{\epsilon_1 k_{\rho 2}I_n(k_{\rho_1}R)} \tag{3.4}$$

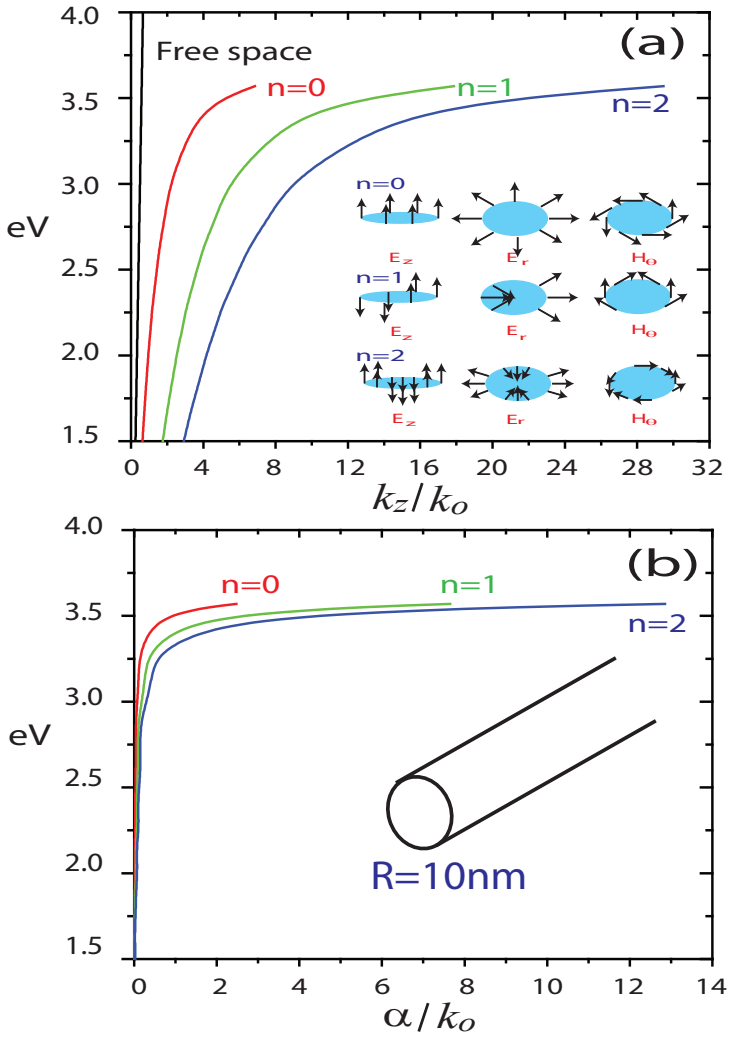

Figure 3.1: (a) Dispersion relations of Ag (silver) MNW with radius (R=10nm) (b) Damping curves of Ag (Silver) MNW with radius (R=10nm). These calculations are obtained from the cubic spine method by using Johnson's experimental optical data. ($k_0 = \omega_p/c$, ω_p is the bulk plasma frequency, c is the light velocity). H fields have the following term $H = H_0 \exp(-\alpha z)\exp(\mathrm{i}\omega t - \mathrm{i}k_z z)$

Newton-Raphson numerical algorithm leads us to calculate the dispersion relation and damping curves in the function of frequency. In this calculation, we have used the complex dielectric constant of Ag, $\epsilon_r(\omega) = \epsilon_{re}(\omega) + j\epsilon_{im}(\omega)$, obtained from the cubic spline method by using the Johnson's experimental optical data [50]. Fig. 3.1(a) shows the SP dispersion relations and damping curves calculated using (3.4) for SP propagating along the Ag MNW with radius $R = 10nm$ which is surrounded by free space medium ($\epsilon_2 = 1$). These dispersion curves are plotted as a function k_z/k_0 ($k_0 = \omega_p/c$, ω_p is the bulk plasma frequency : $9.183\times10^{15} rad/s$, c is the light velocity), which has the non-dimensional wave number. As in the inset of Fig. 3.1(a), the symmetric fundamental mode (n=0) with no surface charge variation in the θ direction leads to small momentum mismatch between free space and SP wave, and small damping coefficients compared to the higher other modes (n>0). Moreover, as shown in Fig. 3.1(a), for a low frequency, SP modes asymptotically approach the light line and small damping loss and, at large k_z, the SP modes approaching the cutoff frequency $0.707\omega_p$ has the strong damping loss. This behavior is similar to that of flat metallic SP mode. However, compared to zero curvature structure which denotes metallic flat surface, positive charge distribution and circular electron confinement with small geometry (R=$10nm$) induce the strong momentum. For example, for ω=$0.4\omega_p$, the momentum of fundamental mode (n=0) numerically found to be $k_z \sim 9.4k_f (k_f = \omega/c)$. However, in the case of metallic flat structure with free space surrounding material $\epsilon_2 = 1$, for ω=$0.5\omega_p$, the momentum of SP analytically found to be $k_{sp} \sim 1.22k_f$ by using (3.1). This strong momentum mismatch of one-dimensional SP wave is responsible for the EM coupling problem and multiple scattering interferences between light and SP wave. In order to check the size contraction of non-radiative SP propagation along the MNW, we have simulated for MNWs with different radius. In Fig. 3.2(a) and 3.2(b), the dispersion relations and damping curves obtained by Newton-Rapshon algorithm for the case of n=0 (fundamental propagation mode) are also plotted. As

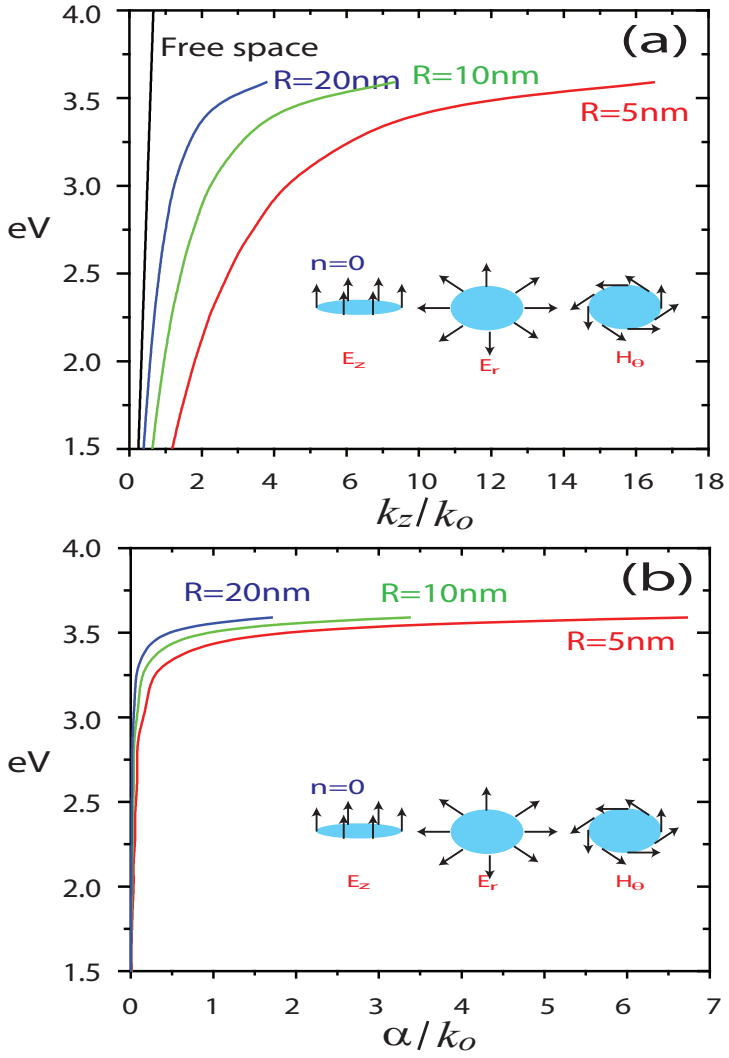

Figure 3.2: (a) Dispersion relations of Ag (silver) MNW with diffrent radii (b) Damping curves of Ag (Silver) MNWwith different radii. These calculations are obtained from the cubic spine method by using Johnson's experimental optical data. ($k_0 = \omega_p/c, \omega_p$ is the bulk plasma frequency, c is the light velocity). H fields have the following term $H = H_0\exp(-\alpha z)\exp(\mathrm{i}\omega t - \mathrm{i}k_z z)$

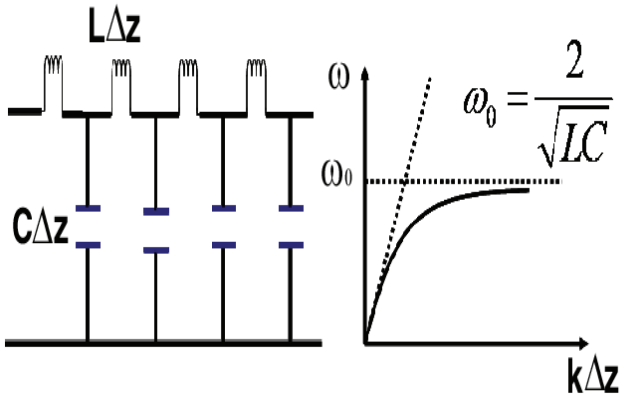

Figure 3.3: The lumped low pass transmission line model and dispersion curve.

can be seen, small radius leads to increase the momentum and attenuation coefficient. As expected, the size contraction has a significant impact on the photonic behavior of SP wave.

3.3 Nano-transmission line modeling of MNW

It has been shown that SP modes along the MNW have the cutoff frequency ω_0=0.707ω_p. Below the cutoff frequency (ω_0), SP modes can be generated along the MNW. Intuitively, this behavior can be interpreted as a low pass lumped TL model with series L (inductance per unit length) and C (capacitance per unit length), having the cutoff frequency ω_0=$2/\sqrt{LC}$ as shown in Fig. 3.3. This dispersion analysis of TL model provides a theoretical physical concept for the energy transfer mechanism along the MNW. In this section, we examine a simple case of the TL modeling of the MNW. To calculate the TL parameters, we begin to find out the basic physical mechanism in the MNW. The electron cloud oscillation around the metallic surface can be generated by a local field excitation. These oscillatory electron clouds give rise to unique EM field distribution, where the magnetic fields have only axial component H which means the TM waves. If we consider the SP damping factor, SP energy transfer can be modeled as a low-pass lumped TL consisting of inductance, capacitance, resistance

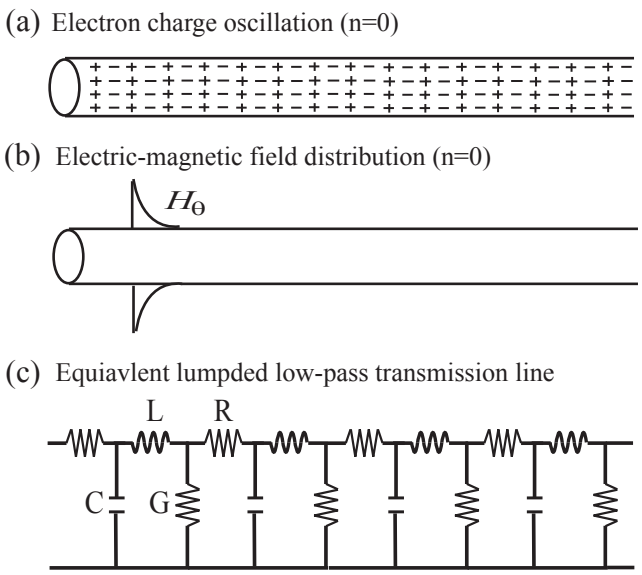

Figure 3.4: Equivalent models of nonradiative SP wave along the MNW with fundamental mode n=0 with no surface charge variation in the direction. (a) Electron charge oscillation model. (b) EM field distribution. (c) Equivalent lumped low-pass transmission line model.

and conductance as shown in Fig. 3.4(c). Furthermore, in order to calculate these circuit parameters, it is necessary to evaluate the current and voltage as a physical quantity. In general, the voltage and current of TEM wave in the usual fashion as integral in the transverse plane:

$$I(z,t) = -\oint \vec{H} \cdot \vec{dl} \quad \text{and} \quad V(z,t) = -\oint \vec{E} \cdot \vec{dl} \tag{3.5}$$

For SP wave that cannot support a TEM wave, we cannot define unique voltage and current at a given point along the SP MNW. For these reasons, we choose the equivalent current, equivalent voltage and equivalent impedance for TM lines. Even though they are not unique voltage or current, the equivalent parameters yield the proper physical behavior of the guided wave such as power flow, propagation constant and damping. As a first step, to find out equivalent current flow, we start with the transverse EM field distribution around the MNW. By using the magnetic field

continuity at the metallic surface (ρ=R), it is easily found that the EM fields inside the MNW ($\rho < R$) are given by:

$$H_\theta = H_\theta(r = R)\frac{I_{n+1}(k_{\rho 1}\rho)}{I_{n+1}(k_{\rho 1}R)} \tag{3.6}$$

$$E_r = H_\theta(r = R)\frac{k_z I_{n+1}(k_{\rho 1}\rho)}{\omega\epsilon_1 I_{n+1}(k_{\rho 1}R)} \tag{3.7}$$

In the outside region ($\rho > R$) , the EM fields are also given by:

$$H_\theta = H_\theta(r = R)\frac{K_{n+1}(k_{\rho 1}\rho)}{K_{n+1}(k_{\rho 1}R)} \tag{3.8}$$

$$E_r = H_\theta(r = R)\frac{k_z K_{n+1}(k_{\rho 1}\rho)}{\omega\epsilon_2 K_{n+1}(k_{\rho 1}R)} \tag{3.9}$$

The current flow is governed by the Ampere Law:

$$\nabla \times H = \frac{\partial D}{\partial t} + J_p + J_f = \frac{\partial(\epsilon_p E)}{\partial \epsilon_t} + J_f \tag{3.10}$$

where J_p is the polarization current density and J_f is the source current density and ϵ_p=$\epsilon_o\epsilon_m$ represents a free electron model. Moreover, the EM fields originate from the embedded electron charge oscillation of metallic structure, thereby reducing to source free region with source current $J_f = 0$. In this section, we only concentrate on the fundamental (n=0) non-radiative TM mode with no surface charge variation in the direction. With the stokes theorem, the total current flow of fundamental mode (n=0) around the MNW is readily obtained:

$$I_z(R) = 2\pi R H_\theta(r = R) \tag{3.11}$$

The validity of (3.11) can be physically explained by oscillating charge distributions inside the MNW ($r \leq R$) as shown in Fig. 3.4(a). Since the magnetic fields lie in

the transverse plane, the induced currents around the MNW are directed into the z axis. However, the physical quantity of voltage is not easily obtained by using the integral formulation E_r as shown in (3.5) because the locally distributed oscillating charges around the periphery of the MNW generates not TEM wave, but TM wave with E_z field. As an alternative of E_r field integration, we have used net power flow over the cross section (r-θ plane) to obtain the physical quantity of voltage flow. For example, in a similar way, the radiation impedance for the antenna such as dipole or linear wire with a current distribution can be obtained by calculating the radiation power flow. This idea is extensible to obtain the effective voltage along the MNW. In detail, the time averaged power flow in the $+z$ direction around the MNW at the given point z is given by:

$$P_{net} = P_z^{in} + P_z^{out} = \frac{1}{2}\int_{A_{in}} E_r^+ \cdot H_\theta^{+*} + \frac{1}{2}\int_{A_{out}} E_r^+ \cdot H_\theta^{+*} \tag{3.12}$$

Then, Eqn. (3.12) can be written in terms of current flow:

$$P_{net} = \frac{1}{2} I_z^+(r=R) I_z^{+*}(r=R)(Z_{in} + Z_{out}) \tag{3.13}$$

where

$$Z_{in} = \frac{k_z}{2\pi R^2 \omega \varepsilon_1} \frac{1}{I_1(kR)I_1(kR)} \int_0^R I_1(k_{\rho_1}\rho) I_1(k_{\rho_1}\rho)\rho d\rho \tag{3.14}$$

and

$$Z_{out} = \frac{k_z}{2\pi R^2 \omega \varepsilon_2} \frac{1}{K_1(kR)K_1(kR)} \int_R^\infty K_1(k_{\rho_1}\rho) K_1(k_{\rho_1}\rho)\rho d\rho \tag{3.15}$$

As can be seen, the power flow along the MNW can be classified as the right handed power flow (P_z^{out}) and left handed power flow (P_z^{in}). In detail, outside the MNW, E_r and H_θ have right cross product in terms of wave-vector k_z, so $P_z^{out}>0$. However, inside the MNW, E_r has reverse direction because of $\varepsilon_2<0$, denoting left cross product

and denoting $Re(P_z^{in})$<0. The net power flow is the sum of P_z^{out} and P_z^{in}. To be specific, we can calculate the Z_{out}=201.1 and Z_{in}=$-2.4268 - 0.0709j$ at $2.0eV$ (red spectrum) in the case of MNW with radius $10nm$ based on the SP dispersion relation and damping curve as shown in Fig. 3.1. Because of $Z_{out} \gg Z_{in}$, the dominant power flow around the MNW is P_z^{out}, thus validating the SP dispersion relation mimicking to the low pass TL. On the other hand, if the left handed power flow dominates, the series impedance $Im(Z \sim jk_z Z_c)$ is negative, thus denoting the high pass TL to explain the negative refractive EM behavior. Furthermore, this net power flow concept can be used to connect between effective current and effective voltage in the circuit theory. Especially, the complex power flow in the circuit theory can be expressed in terms of complex harmonic voltage and current:

$$P^+ = \frac{1}{2} V^+ I^{+*} = \frac{1}{2} I^+ Z_c I^{+*} \tag{3.16}$$

In this section, we define the characteristic impedance of the MNW to connect the voltage and current.

$$Z_c = Z_{in} + Z_{out} \tag{3.17}$$

where Z_c=V^+/I^+ means connecting parameter to relate effective voltage and effective current at a single position. In the case of the MNW, the Z_c can be approximately written as:

$$Z_c \cong Z_{out} \tag{3.18}$$

In a typical TL method, the characteristic impedance Z_c provides information about reflection properties. For example, the MNW with Z_c is terminated with a load impedance Z_L, the reflection coefficient can be described by:

$$\Gamma_L = \frac{Z_L - Z_c}{Z_L + Z_c} \tag{3.19}$$

Physically, the terminated load impedance of MNW can be approximately modeled as open circuit load $Z_L \longrightarrow \infty$ because the current distribution only confined to inside the MNW. However, the MNWs consist of physical lines with various discontinuities and transitions such as gap in MNWs, change in radius, T-junction MNW and coax-to-MNW junction. These discontinuities are required to shunt or series elements across the junction to satisfy the SP physical phenomenon such as EM matching issues. This analysis is much more difficult to analyze and more detail EM analysis is needed to obtain the accurate equivalent circuit elements. In this paper, we only deal with MNWs without no discontinuities and transitions. Now, it has been shown that the effective voltage and effective current flow at a physical single position are related to net power flow, we now focus on the TL parameters. We have started two fundamental assumptions: the lumped element model and sinusoidal current (or voltage) waveform. The validity of the lumped circuit model is that circuit parameters of the MNW are not distributed into a single physical position but are lumped into all length. Thus, the TL equations can be expressed as:

$$\frac{dV}{dz} = ZI \quad \text{and} \quad \frac{dI}{dz} = -YV \tag{3.20}$$

where Z and Y mean the distributed series impedance and shunt admittance, respectively. The second assumption denotes that the current (or voltage) in the $+z$ direction can be expressed as follows:

$$\begin{aligned} I(z,t) &= I\exp(-\alpha z)\exp(\mathrm{i}\omega t - ik_z z) \\ V(z,t) &= V\exp(-\alpha z)\exp(\mathrm{i}\omega t - ik_z z) \end{aligned} \tag{3.21}$$

where k_z and α are satisfied with SP transcendental equation. Therefore, with the help of (3.21), Eqn. (3.20) can be described by:

$$\begin{aligned} \frac{dV(z,t)}{dz} &= -(\alpha + jk_z)V(z,t) = -ZI \\ \frac{dI(z,t)}{dz} &= -(\alpha + jk_z)V(z,t) = -YI \end{aligned} \tag{3.22}$$

With the help of connecting parameter Z_c between V and I, the lumped series impedance (Z) and shunt admittance (Y) can be expressed as:

$$Z = (\alpha + jk_z)Z_c \quad \text{and} \quad Y = \frac{\alpha + jk_z}{Z_c} \tag{3.23}$$

In the case of sinusoidal excitation, the Z and Y of the low pass TL can be described as:

$$r + j\omega l = (\alpha + jk_z)Z_c \quad \text{and} \quad \mathrm{g} + j\omega c = \frac{\alpha + jk_z}{Z_c} \tag{3.24}$$

where r, l, g and c denote resistance per unit length (R/m), inductance per unit length (L/m), conductance per unit length (G/m) and capacitance per unit length (C/m), respectively. In the case of the MNW, the damping coefficient (α) can be an order of magnitude of the wave vector (k_z) in the optical spectrum as shown in Fig. 3.5(a). Thus, the damping factor (α) should be considered to calculate the TL parameters of the MNW. Fig. 3.5(b) shows the fundamental mode (n=0) impedance (Z=R+jX) curves for MNW by using the dispersion relation and damping coefficient calculated from the SP dispersion relation. Firstly, positive reactance ($X > 0$) indicates the inductive element because of $Z_{out} \gg Z_{in}$, verifying a low-pass lumped TL. As it is expected, the damping coefficient of SP proportionally provides equivalent nano-resistance as shown in Fig. 3.5(b). For example, in the blue (optical) spectrum ($\omega\sim 4.56 \times 10^{15} rad/s : 3.0eV$), resistance and reactance of the MNW with radius $10nm$ approximately have about $0.404\Omega/nm$ and $10.7\Omega/nm$, denoting high

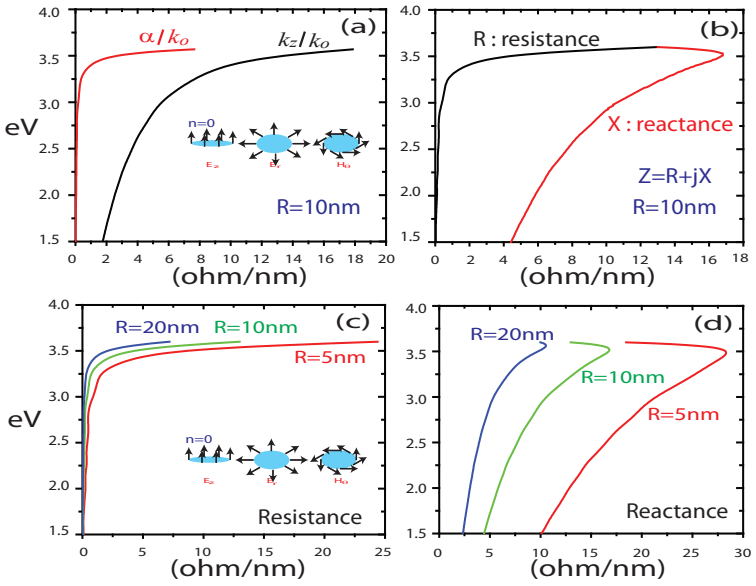

Figure 3.5: (a) Plasmon 0^{th} mode wave number and damping coefficient of Ag with radius 10nm. (b) Impedance (Z=R+jX) of plasmon 0^{th} mode of metallic nanowire with radius 10nm. (c) Resistance of SP 0^{th} mode as a function of frequency with different radii. (d) Reactance of SP 0^{th} mode as a function of frequency with different radii.

damping mechanism. However, in the red (optical) spectrum ($\omega_p \sim 3.04\times10^{15} rad/s$: $2.0eV$), resistance and reactance have about $0.101\Omega/nm$ and $5.82\Omega/nm$, denoting small damping mechanism and low impedance compared to blue spectrum. Fig. 3.5(c)-(d) shows the effect of radius on the impedance of SP propagation along the MNW. As can be seen, the small dimension of the MNW leads to strong attenuation and high reactance. From the curves, as the radius increases twice, the resistance and reactance almost decrease at half values.

3.4 The equivalent circuit modeling for SP propagation along the MNW

In previous sections, we have introduced the TL properties of the SP MNW: capacitance per unit length (C/m), inductance per unit length (L/m), resistance per

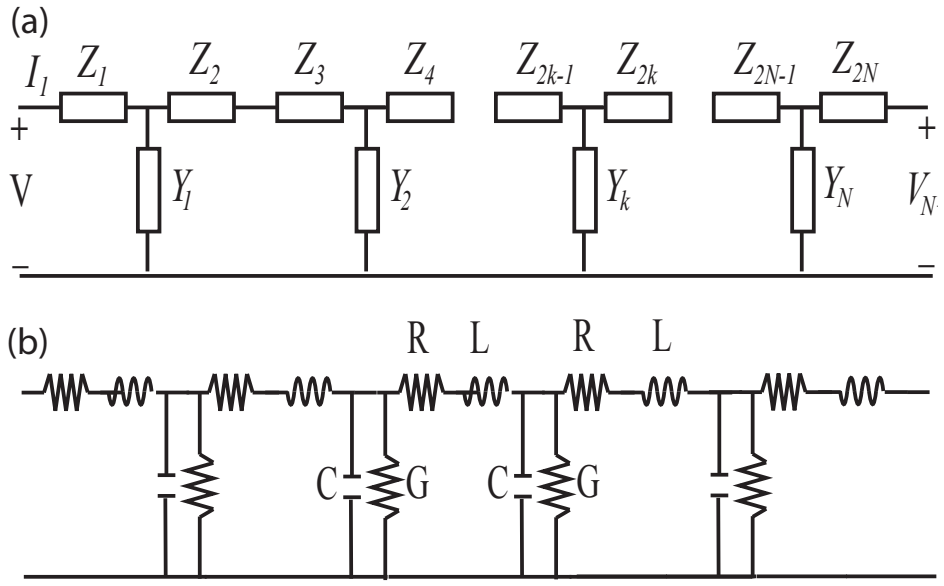

Figure 3.6: (a) Finite difference (FD) based element equivalent circuit (b) T-cell RGLC circuit model of a low-pass transmission line model.

unit length (R/m) and conductance per unit length (G/m). These parasitic elements have an impact on the photonic behavior of the SP MNW circuit and influence its delay, power attenuation and reliability [58]. Basically, the lossy TL can be analyzed by using two basic approaches: convolution method with impulse response and lumped element circuit model [59].

In this section, we focus on the lumped equivalent circuit model, thus easily implemented in the existing circuit simulation tools such as Spice simulator. To demonstrate the lumped equivalent circuit model, let the distributed per-unit-length (PUL) parameters of the MNW be denoted by Z and Y, representing series impedance and shunt admittance, respectively. By applying the finite difference (FD) method in (22), the FD discretization with respect to z leads to a RGLC network as shown in Fig. 3.6. Among many different FD discretizaion methods such as T-cells, π-cells and half-cells, we have simulated the symmetric T-cell method since different cell methods lead to a quite similar result if the cell lengths are small enough. Let us assume that

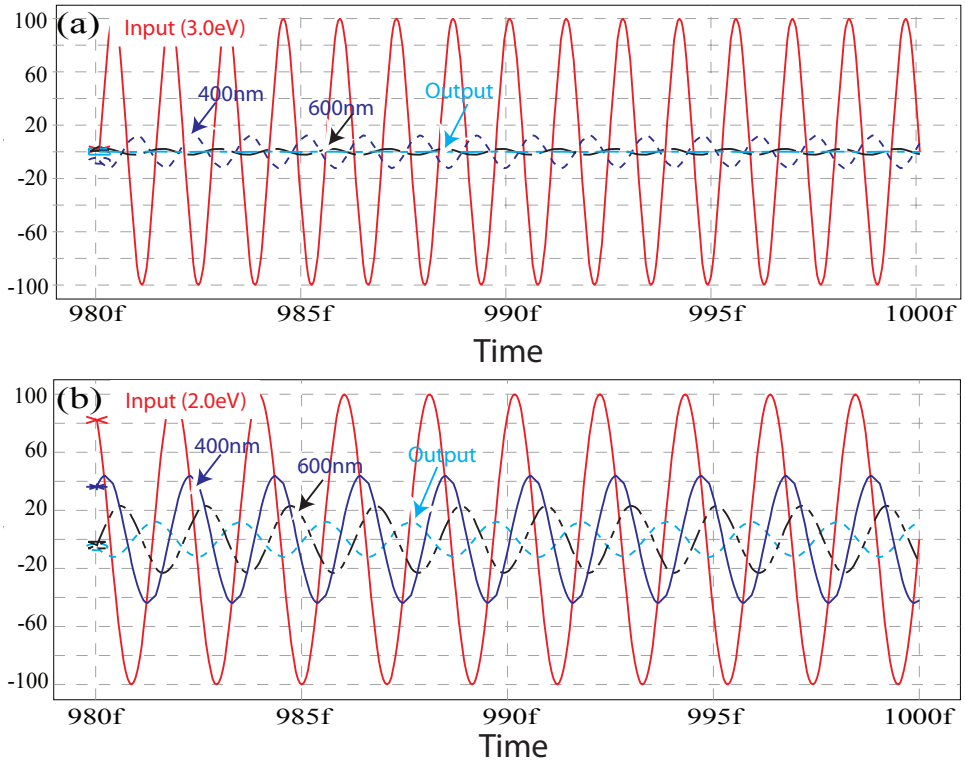

Figure 3.7: H-spice transient analysis of Ag MNW (radius: 10nm, length : 800nm) obtained by H-spice simulator: (a) Blue optical frequency ($\omega \sim 4.5610^{15}$ rad/s: 3.0eV). (b) Red optical frequency ($\omega \sim 3.0410^{15}$rad/s: 2.0eV)

the number of T-cells is N, the resistance, inductance, conductance and capacitance elements of i^{th} T-cell segment can be obtained by:

$$\bar{Z}_i = R_i + sL_i = \frac{Zl}{2N} \quad \text{and} \quad \bar{Y}_i = G_i + sC_i = \frac{Yl}{N} \tag{3.25}$$

where l is the length of the MNW, N is the number of T-cell segment. If we consider a MNW with a length $l = 800nm$, a radius $R = 10nm$ and free space host matrix ($n = 1$). By dividing the MNW into 40 sections, T-cell equivalent circuit parameters at the blue spectrum have the values: $R = 3.92ohm$, $L = 23.25fH$, $G = 0.264mS$ and $C = 1.94aF$. On the other hand, at the red frequency ($\omega = 3.04 \times 10^{15} rad/s : 2.0eV$), the T-cell equivalent circuit parameters have the following values: $R = 1.01ohm$, $L = 19.13fH$, $G = 0.0489mS$ and $C = 0.979aF$. In Fig. 3.7, the transient analysis performed by HSPICE is illustrated as a function of time. In this case, the input source generates a sinusoidal signal with the amplitude $100V$. Four signal waveforms represent the transient voltage at input port, $400nm$ node, $600nm$ node and output port $800nm$, respectively. The parasitic elements of blue spectrum ($3.0eV$) play a dominant role in SP power attenuation as shown in Fig. 3.7(a). As expected in previous sections, to address signal dissipation, it is necessary to decrease the operational signal frequency. As shown in Fig. 3.7(b), the red spectrum leads to transfer SP non-radiative signal with small damping factors compared to blue spectrum operation. To confirm the following equivalent circuit parameters of MNW, we have conducted 3D scattered FDTD implementation since this approach has some advantages over the total field formulation in that the dispersive calculation-error of incident field is negligible and absorbing boundary condition of scattered field can be easily implemented [60]. Based on the frequency dependent FDTD, our simulation volume is chosen as a three dimensional rectangular box with dimension $1000 \times 300 \times 300nm^3$. We consider an Ag MNW with a length of $800nm$ and a radius of $10nm$, which is surrounded by

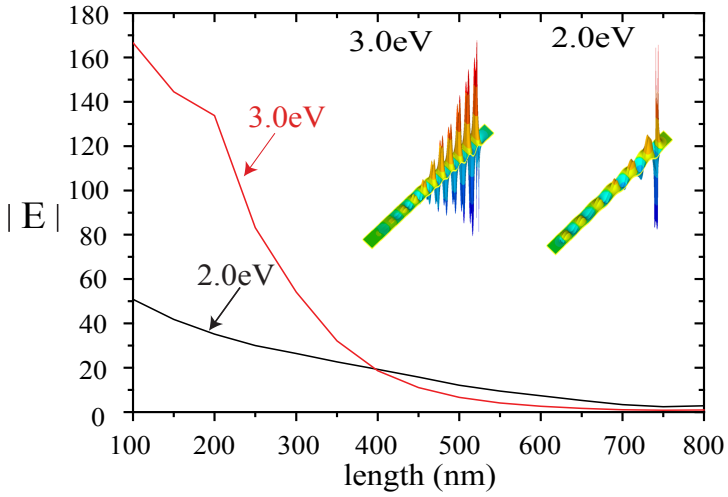

Figure 3.8: The average E-field density in the Ag MNW (radius=10nm) performed by FDTD. These values are calculated at the positions at 15nm offset positions (z-directed) from the axis of MNW.

a free space (n=1). For demonstrating a local non-radiative SP propagation along the MNW, the incident plane wave, polarized parallel to the longitudinal axis of the MNW, irradiates at the input terminal of the MNW. Accordingly, we obtain the average E-field density at different positions. These values are calculated at the positions at 15nm offset positions (z-directed) from the axis of MNW. The inset of Fig. 3.8 shows x component of the scattered field (x-y plane) calculated by using the FDTD simulation for two difference frequencies. As shown in Fig. 3.8, even though the blue frequency (ω=$4.56 \times 10^{15} rad/s : 3.0eV$) generates strong subwavelength localization at the input port of SP MNW because the resonant SP frequency of Ag MNW locates at the blue spectrum, power attenuation become dominant in this spectrum. In contrast, red spectrum (ω=$3.04 \times 10^{15} rad/s : 2.0eV$) produces weak subwavelength confinement and slowly attenuating near field along the SP MNW. In Fig. 3.9, the attenuation of E-field (FDTD) and voltage (H-spice) are compared. These values at different positions are normalized to the input values. The closely agreement between FDTD and H-spice validates the MNW equivalent circuit parameters. As the

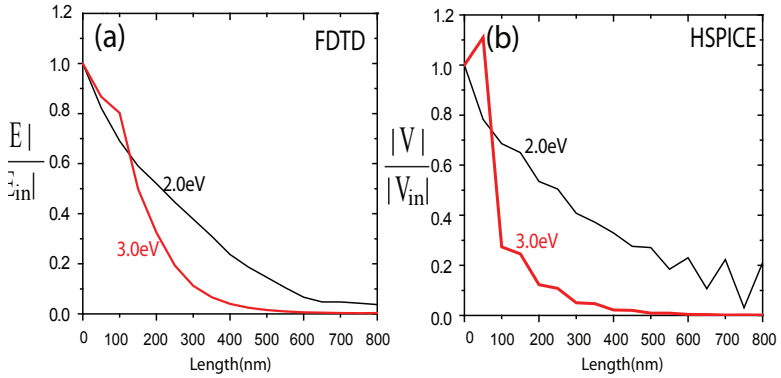

Figure 3.9: (a) The average E-field density in the Ag plasmon wire (radius=10nm) calculated by using FDTD simulation. (b) The average voltage of the Ag plasmon wire (radius=10nm) calculated by H-spice simulation based on the circuit parameters. These values are normalized to the input values.

frequency reduces, small damping coefficients lead to multiple reflections between two terminals of MNW. When the propagation speed and operational frequency become sufficiently fast, the multiple reflection plays an important role in the behavior of TL. For example, the Fabry-Perot resonator as the silver MNW with diameter around $100nm$ is experimentally demonstrated [61]. In detail, by using the Fabry-Perot resonator analysis, if the electric amplitude of the SP wave after $2(k-1)$ traveling is A_k, the amplitude gain loss per pass between MNW is $g = \exp(-\alpha L)$ and the phase change between adjacent wave k and $k+1$ is the $\theta = k_z L$. The amplitude A_k has the following relations: $A_1 = A_0 t^2 g \exp(\mathrm{j}\theta)$ and $A_{k+1} = A_k r^2 g^2 \exp(2\mathrm{j}\theta)$ if $k \geq 1$, where A_0 denotes the amplitude of incident electric field in the MNW. Thus, the SP transmittance is given by:

$$T_{plasmonic} = \left| \frac{A_{trans}}{A_0} \right| = \frac{(1-R)^2 g^2}{(1-Rg^2)^2 + 4Rg^2 \sin^2(k_z L)} \tag{3.26}$$

where $R{=}r{*}r$ denotes the reflectivity of SP wave in the MNW. As seen from (3.26), the SP transmittance can be controlled by reflectance coefficient, wave number and guiding length. To generate the multiple reflections along MNW, we now focus on the SP

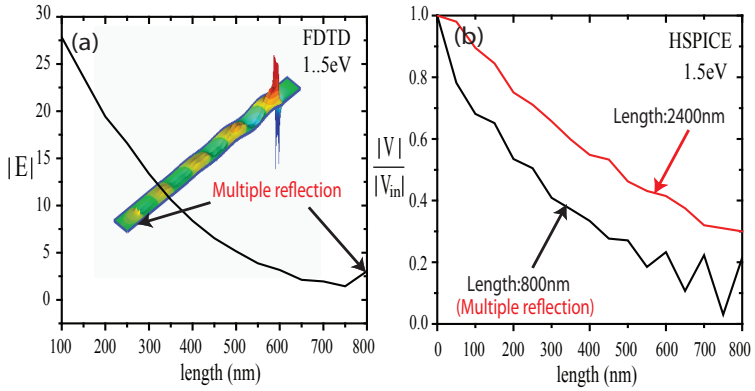

Figure 3.10: (a) The average E-field density in the Ag plasmon wire (radius=10nm, length=800nm) at a frequency ($\omega \sim 2.2810^{15}$rad/s: 2.0eV) by FDTD. (b) The average voltage of the Ag plasmon wire (radius=10nm) calculated by H-spice simulation based on the circuit parameters. Black line denotes the N=40 segments with length l=800nm and red line indicates the N=120 segments with length l=2400nm, respectively.

guiding mechanism in the MNP at a frequency $1.5eV$ ($\omega = 2.28 \times 10^{15} rad/s : 1.5eV$). In Fig. 3.10(a), the average E-field density for Ag MNW ($R = 10nm$) is obtained by FDTD simulation. As can be seen, the extraordinary EM field enhancement at the destination terminal can be explained by the multiple reflections between MNW. In order to check the effect of multiple reflections, we have conducted two different equivalent circuit models with different T-cell segments. Black line denotes the $N = 40$ segments with length $l = 800nm$ and red line indicates the $N = 120$ segments with length $l = 2400nm$, respectively. Both all T-cell equivalent circuit parameters at the frequency $1.5eV$ have the values: R=0.306ohm, L=19.39fH, G=0.0127mS and C=0.749aF. In the case of N=120 segment (length=2400nm), the termination of the line appears an infinite extension termination line because damping effects leads to small portion of reflection wave. Fig. 3.10(b) gives us a clue on how multiple reflections take an affects on the transient behavior of MNP wire. As apparent from figure, multiple reflections generate a complex voltage behavior at the destination and rapidly decreasing voltage waveform compared to infinite extension transmission

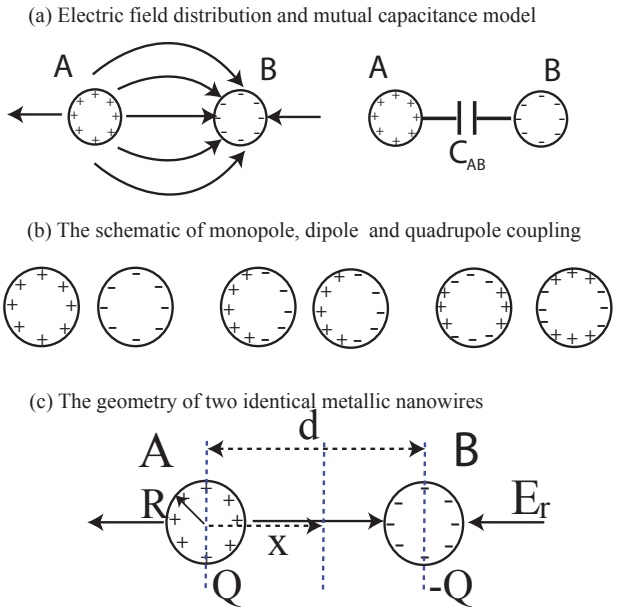

Figure 3.11: (a) Electric field distribution and mutual capacitance model. (b) The schematic of monopole, dipole and quadrupole coupling. (c) The geometry of two identical MNWs.

line.

3.5 The circuit network of MNWs

Until now, we have concentrated on the single MNW structure. However, when MNWs array are close together, power can be coupled between the MNWs array due to the interaction of the EM fields of the MNW lines [62],[63]. When signal pulses are transmitted between MNWs, two fundamental mechanisms are strongly related: (1) Electric field coupling [64] and (2) Magnetic field coupling [65], . In this section, we concentrate on the electric static coupling because the electric-static coupling is dominant [66]. In detail, the electric-static coupling is modeled as the mutual capacitance as shown in Fig. 3.11(a). In the case of MNWs, the electric-static coupling is evaluated by using the multiple expansion method. As shown in inset of Fig. 1(a), the charge distribution of the MNW can be expanded as sum of

monopole, dipole and quarupole, etc. Fig. 3.11(b) shows the schematic depiction of electric-static coupling of multiple expansions. In the case of non-radiative TM modes, at n=1 and and n=2, dipole and quadrupole electric-static coupling mimics the electric coupling between MNWs. In the case of fundamental mode (n=0), the monopole electric-static field distribution allows us to evaluate the mutual capacitance C_{AB} between two MNWs. In simplicity, we consider the n=0 TM propagation mode and corresponding mutual capacitance C_{AB} between two identical wires (r=R) with spatial distance d between their axes as shown in Fig. 3.11(c). At the point x ($x \geq R$), the E_r fields can be calculated as a result of superposition of the E_r fields from A wire and B wire, that is,

$$E_{r1} = -B\frac{ik_z}{k_{\rho 2}}[K_1(k_{\rho 2})x + K_1(k_{\rho 2}(d-x))] \tag{3.27}$$

The surface charge Q at r=R is calculated by using the Gauss's law

$$\frac{Q}{2\pi R\epsilon_2} = -B\frac{ik_z}{k_{\rho 2}}K_1(k_{\rho 2R}) - A\frac{ik_z}{k_{\rho 1}}I_1(k_{\rho 1R}) \tag{3.28}$$

From boundary conditions with tangential magnetic field components continuity, we obtain the following constitutive relation:

$$\frac{A}{B} = -\frac{k_{\rho 1}\epsilon_2 K_1(k_{\rho 2}R)}{k_{\rho 2}\epsilon_1 I_1(k_{\rho 1}R)} \tag{3.29}$$

Substituting (3.29) into (3.28) yields

$$\frac{Q}{2\pi R\epsilon_2} = -B\frac{ik_z}{k_{\rho 2}}[K_1(k_{\rho 2R}) - \frac{\epsilon_2}{\epsilon_1}K_1(k_{\rho 2R})] \tag{3.30}$$

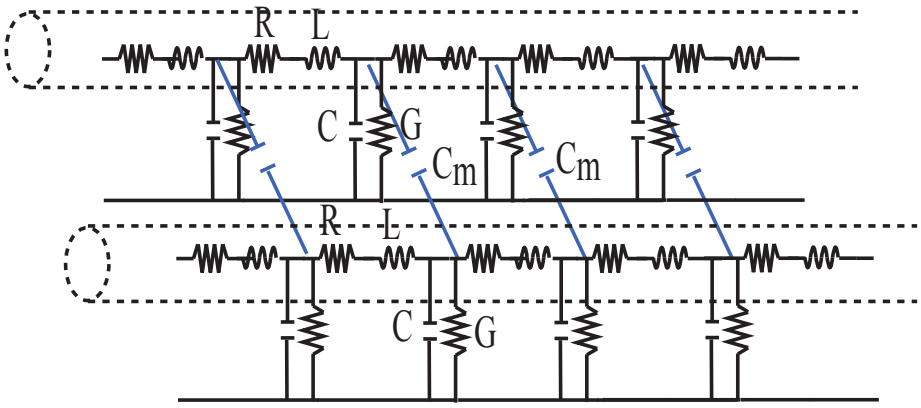

Figure 3.12: The circuit model of the parallel MNW wires.

The voltage between two MNWs ($d \gg R$) can be approximately obtained by the integration of E_r :

$$V = \int_{R}^{d-R} E_r dx \tag{3.31}$$

We obtain the mutual capacitance ($C_{AB} = Q/V$) between two MNWs:

$$C_{AB} \approx \frac{Re[\pi R \epsilon_0 K_1(k_{\rho 2} R)(1 - \frac{\epsilon_2}{\epsilon_1})]}{\int_R^{d-R} K_1(k_{\rho_2} x) dx} \tag{3.32}$$

Let us assume the two MNWs with radius R=20 nm, spatial distance d=60nm and free space host matrix (n=1). (3.30) shows that the mutual capacitance of Ag wire has the value C_{AB}=0.1240nF/m (at 3.0eV) and C_{AB}=34.47pF/m (at 2.0eV), respectively. To be specific, we construct the equivalent circuit networks for a coupled MNWs line as shown in Fig. 3.12. For example, if we consider two identical MNWs with a length l=800 nm and divide the MNWs into 40 sections, T-cell equivalent circuit parameters (at 2.0eV) have the following values: R=1.01ohm, L=19.13fH, G=0.0489mS, C=0.979aF and C_m=0.6893aF. This coupled circuit network can be analyzed by using the even- and odd-mode analysis or HSPICE circuit simulator. Furthermore, this analysis based on the electro-static coupling can be extended to evaluate the crosstalk

between multiple MNWs.

3.6 Conclusion

We have studied the equivalent circuit modeling of SP propagation along the MNW. Our proposed equivalent circuit model provides a basic understanding of the nature of SP propagation along the MNW and distributed circuit elements, and of how operational frequency and guiding geometry affect the performance of MNW circuitry. Even though SP of MNW in the near-infrared and visible spectrum has severe limitations as a longer signal interconnect, the fast velocity and high operational frequency enabled by SP wave will provide a novel approach to obtain ultrafast speed integrated circuitry. Furthermore, this equivalent circuit modeling will aid us in the further analysis and optimization of complex SP devices.

CHAPTER IV

Terahertz spoof surface plasmon polariton waveguide and switch comprising the perfect conductor metamaterial

4.1 Background

Even though the terahertz (THz) frequency (0.1∼3 THz) remains an underexploited regime in the electromagnetic (EM) spectrum and very little commercial products operating in the THz domain have penetrated in the market, the THz EM spectrum has recently evoked a considerable interest among device and circuit researchers. New investigations are currently underway to identify future promising applications like astronomical remote sensing, medical imaging systems, military detection, and ultrafast computer logic circuit [67],[68],[69],[70]. Specifically, as a basic building block for THz family of devices, passive elements such as waveguide, ring resonator,and filter are now being explored as components for the next generation of integrated circuits. Unfortunately, the conventional index-guiding methods such as plastic ribbons and sapphire fibers are not suitable for THz guiding or focusing, because of their high signal power loss [4]. As an alternative to solving the damping problems, simple metal wire was recently developed for guiding THz radiation in the form of surface plasmon polariton (SPP) that propagates at the interfacial surface

between a dielectric and a metal [5]. Compared to dielectric-based waveguides, the THz SPP wave offers low loss and low dispersion. Therefore, metallic structures for carrying THz signal have gained considerable attention for THz passive elements.

However, a simple metal wire supports weakly guided THz waves because of negligible field penetration into the metallic side in comparison to the dielectric matrix surrounding the metallic wire. To overcome the weak SPP confinement in the THz domain, surface topology engineering can be employed to create holes, grooves, and dimples which mimic realistic SPP behavior at the visible or ultraviolet spectrum [71], [72]. The resulting spoof SPP (SSPP) modes enhance the subwavelength confinement on themetal surface by generating highly localized surface bound modes in the perfect conductor [73],[74]. In this chapter, we demonstrate how to build efficient THz passive circuit by utilizing these mimicking SSPP bound modes [33],[34]. However, to perform more complex signal routing and process arbitrary Boolean functions, the integrated circuit devices will require dynamic control of the guided THz signal [35]. Specifically, the active SPP circuit operating in the near infrared or optical frequency spectrum have been demonstrated and currently being explored by using some innovative methods such as electrooptical (EO), thermooptical, and all-optical devices [75],[76]. Furthermore, dynamic control of SPP modes in the lower frequency domain can be accomplished by using optical or thermal control on corrugated semiconductor structure [77]. This will open a promising possibility for controlling SPP signal and three-terminal SPP devices.

In this chapter, we present a novel way to obtain an active THz SSPP switch or modulator in the perfect conductor. More recently in the literature, it is reported that the highly localized SSPP bound modes along the corrugated metallic wire can be controlled by varying its geometrical dimensions such as radius or height [34], [78]. In addition to the geometry-based method, the dynamic control of the SSPP modes can be achieved by changing the refractive index of the indentation of the grooves or

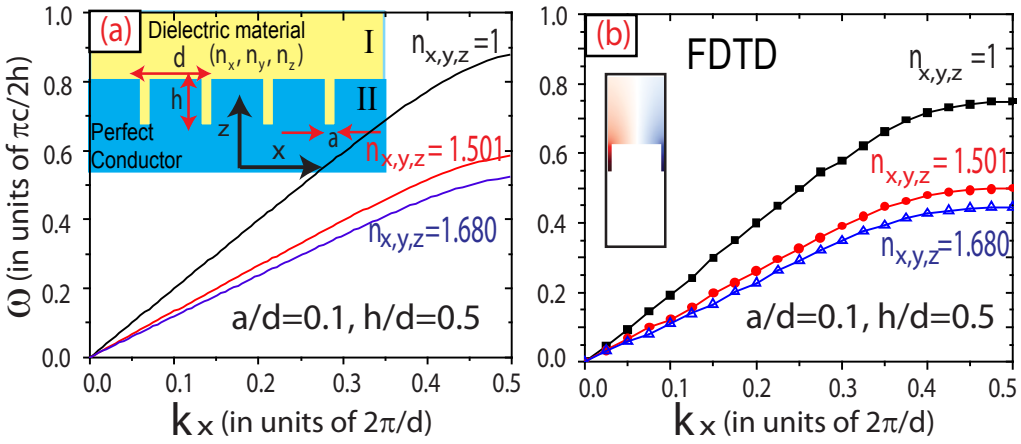

Figure 4.1: (a) Dispersion diagram of SSPP modes calculated from (4.7). (b) Dispersion diagram of SSPP modes calculated from FDTD. The structure is supported by a 1-D array of grooves with geometrical parameters $a/d = 0.1$ and $h/d = 0.5$.

the host matrix. Here, we demonstrate that the TM dispersion relation of surface-bound modes in the perfect conductor limit can be tailored by changing the refractive index of the grooves Specifically, the incorporation of nematic liquid crystal (N-LC) into the plasmonic gap structure, where the SSPP bound modes propagate in the dielectric gap between two textured perfect conducting surfaces, allows the device to modulate the resonant frequency of the FabryProt-like wave [79] depending on the LC orientation. This simple principle enables us to design active THz SSPP switches and modulators that are activated by electrically or optically controlled birefringence.

4.2 Dispersion diagram of SSPP along the corrugated periodic metamaterial

The inset of Fig. 4.1(a) schematically shows a perfectly conducting surface that is corrugated periodically with the linearly spaced rectangular grooves that are infinite in y-direction and have height h, width a, and periodic lattice distance d. Moreover, the permittivity of Region I and grooves have anisotropic permittivity (n_x, n_y,

n_z). First, we are interested in calculating the dispersion relation of TM-polarized waves propagating in the x-direction along the corrugated wave structure bounded by anisotropic dielectric material (n_x, n_y, n_z). To analyze the TM dispersion analysis as a quasi-analytical form, the EM modes can be expanded in terms of Floquet modes that are characteristic waves for periodic structures. The H field with TM polarization (magnetic field perpendicular to the plane of grating structure in Region I) may be expressed in terms of modes

$$H_y^I = \sum_{n=-\infty}^{\infty} \rho_n \exp(jk_{z,\mathrm{I}}^n) \exp(jk_{x,\mathrm{I}}^n) \tag{4.1}$$

where ρ_n are amplitude of diffractions $k_{x,I}^n = k_x + 2\pi n/d$ and $(k_{x,I}^n/n_z)^2 + (k_{z,I}^n/n_x)^2 = (\omega/c)^2$ account for biaxial index ellipsoids with $n_x^2 = \epsilon_x/\epsilon_0$, $n_y^2 = \epsilon_x/\epsilon_0$ $n_z^2 = \epsilon_z/\epsilon_0$ and c is the velocity of light. On the other hand, the circular normal surface $(k_{x,I}^n + k_{z,I}^n)^2/n_y^2 = (\omega/c)^2$ represents the TE polarization wave. Notably, in Region II, all fields are zero except inside the grooves (-a/2$\leq$ x $\leq$ a/2) of the perfect conductor, thus H_y within the grooves can be written as a linear combination of the backward and forward z-directional TM modes

$$H_y^{II} = A^+ \exp(jk_{z,\mathrm{II}} z) + \mathrm{A}^- \exp(-jk_{z,\mathrm{II}} z) \tag{4.2}$$

where A^+ and A^- are constants and $k_{z,II} = n_x\omega/c$ (in the case of TE polarization: $k_{z,II} = n_y\omega/c$). It is straightforward to show that the dispersion relation of TM polarized surface wave propagating in x-direction along the periodically corrugated metamaterial can be rigorously derived by applying the boundary conditions: tangential E and H fields at the interface between Region I and II, tangential E fields vanishing at the perfect conductor surface and E-fields at the bottom of the grooves

($z = h$). From the boundary condition, the following equations can be obtained by:

$$\sum_{n=-\infty}^{\infty} \frac{k_{z,II} S_n^2}{k_z n}(A^+ - A^-) = (A^+ + A^-) \text{ and } A^+ \exp(jk_{II,z}h) = A^- \exp(-jk_{II,z}h) \quad (4.3)$$

where $S_n = (1/\sqrt{ad}) \int_{-a/2}^{a/2} \exp(jk_x^{(n)}x)dx$ which is solved to show that $S_n = (\sqrt{a/d})$ $\text{sinc}(k_x^{(n)}a/2)$. We can obtain constitutive matrix with the form of a matrix equation: $Q \times A = 0$, i.e.,

$$\begin{bmatrix} \sum_{n=-\infty}^{\infty} \frac{k_{z,II} S_n^2}{k_z n} - 1 & -\sum_{n=-\infty}^{\infty} \frac{k_{z,II} S_n^2}{k_z n} - 1 \\ \exp(jk_{II,z}h) & \exp(-jk_{II,z}h) \end{bmatrix} \begin{bmatrix} A^+ \\ A^- \end{bmatrix} = \begin{bmatrix} 0 \\ 0 \end{bmatrix} \quad (4.4)$$

The TM dispersion relation can be obtained in the condition of det $Q = 0$, i.e.,

$$1 - j \sum_n (\frac{k_{z,II} S_n^2}{k_{z,I}^n}) \tan(k_{z,II}h) = 0 \quad (4.5)$$

where j is $\sqrt{-1}$ and $S_n = (\sqrt{a/d})\text{sinc}(k_x^{(n)}a/2)$. With the help of the surface bound condition ($k_x \gg n_z\omega/c$) and the subwavelength limit ($\lambda \gg d$ and h), the zero order ($n = 0$) dominates among all other diffraction modes. Thus, the TM dispersion relation of surface bound modes can be simplified as

$$\sqrt{n_x^2 \frac{k_x^2}{n_z^2} - n_x^2 \frac{\omega^2}{c^2}} = n_x \frac{\omega}{c} S_0^2 \tan(\frac{n_x \omega h}{c}) \quad (4.6)$$

In the limit $k_x a \ll 1$, (4.6) becomes

$$k_x = n_z \frac{\omega}{c} \sqrt{1 + (\frac{a}{d})^2 \tan^2(\frac{n_x \omega h}{c})} \quad (4.7)$$

As a simple form, in the case of $n_x = n_y = n_z = 1$, (4.7) coincides with that in eq.(14)of [80], explaining the behavior for $\omega(k_x)$ in the air grooves ($n = 1$). Note that the TM dispersion relation of SSPP modes not only depends on the geometrical parameters

but also relies on the refractive indices of grooves and on Region *I*. In detail, the cutoff SSPP frequency $\omega_c = \pi c/2n_x h$ calculated from (4.5) is controlled by the depth of grooves h and the x-directional refractive index n_x. Recently, the cutoff frequency ω_c on periodically corrugated metal wires also shown to be inversely proportional to the depth of radial grooves [34]. To demonstrate the effect of the refractive index, Fig. 4.1 shows the TM dispersion relation for SSPP bound modes supported by a periodically corrugated perfect conductor with geometrical parameters $a/d = 0.1$ and $h/d = 0.5$. Three different isotropic refractive indices are analyzed: $n_{x,y,z} = 1$, $n_{x,y,z} = 1.501$, and $n_{x,y,z} = 1.680$. For SSPP modes, at the long wavelength ($\lambda \gg d$), the dispersion curves asymptotically approach the light line $k_x = n_z\omega/c$ because the EM wave does not recognize the fine periodic structure. However, as the frequency increases up to the cutoff frequency ω_c , the highly localized surface bound modes are generated along the textured structure. In addition, Fig. 4.1(b) shows the dispersion diagram of SSPP modes calculated from FDTD. These band diagrams can be analyzed in the form of periodic Bloch modes, which means the EM field satisfies the Bloch periodic boundary condition. Even though the results of FDTD much like that of analytical method, the small difference between analytical calculation and FDTD is explained by the multiple order terms (abs(n)$>$ 0) in (4.5). In Fig. 4.1(a), we disregard the high-order terms (abs(n)$>$ 0) in (4.6) and (4.7), thus pulling up the dispersion curve.

4.3 Dispersion diagram of SSPP along the sandwiched metamaterial

In the previous section, it has been shown that the SSPP bound modes in a corrugated perfect conductor can be controlled by changing the refractive index of the grooves. We now focus on a realistic THz micron-scale switch device. The inset of Fig. 4.2(a) shows a schematic picture of an active THz plasmon switch consisting of a

dielectric plasmon gap between two corrugated perfect meta-materials with geometrical parameters a/d =0.1, h/d =0.5 and t/d =1/3, thus confining the localized THz pulse and demonstrating the highly miniaturized active THz switch. For a complex geometry, the SSPP dispersion curves and mode profiles of the sandwiched structure can be obtained by FDTD. In contrast to one-dimensional corrugated structure, the sandwiched structure exhibits interesting features. To be specific, the reflection symmetry through the plane z=0 generates multiple SSPP modes along the signal line as shown in Fig. 4.2(a). The dispersion of first band modes closely matches with that of one-dimensional array grooves calculated from (4.7). In addition, the periodic x-directional transition symmetry creates the SSPP band-gap similar to photonic crystals. Furthermore, the second modes (resonant modes) with a flat band are located at the region between the SSPP band-gap. Thus, these modes become a slow light in which the velocity of SSPP modes physically can be lowered. Furthermore, slow light enabled by resonant mode operation is promising method for shrinking the size of THz devices and controlling THz signal in the time domain [81],[82],[83].

In contrast to periodic dielectric ($n > 0$) waveguide, the existence of resonant modes can be understood intuitively by considering the field distribution inside metallic gap structure. For example, the periodic dielectric corrugated gap structure with refractive index ($n >$0) cannot support the localized field because of the boundary condition. However, the metallic structure provides the confined deep SSPP modes on the subwavelength scales, thus supporting the resonant modes as shown in Fig. 4.2(a).

To obtain an efficient THz switch, we concentrate on the resonant SSPP modes for two fundamental reasons: small damping mechanism and strong SSPP confinement. Firstly, to verify the small damping system at resonant modes, we conduct the computation of the quality factor $Q \sim \omega_o/\gamma$ where is the loss rate as shown in Fig. 4.2(b). The quality factor Q is useful in determining the system behavior in the resonant

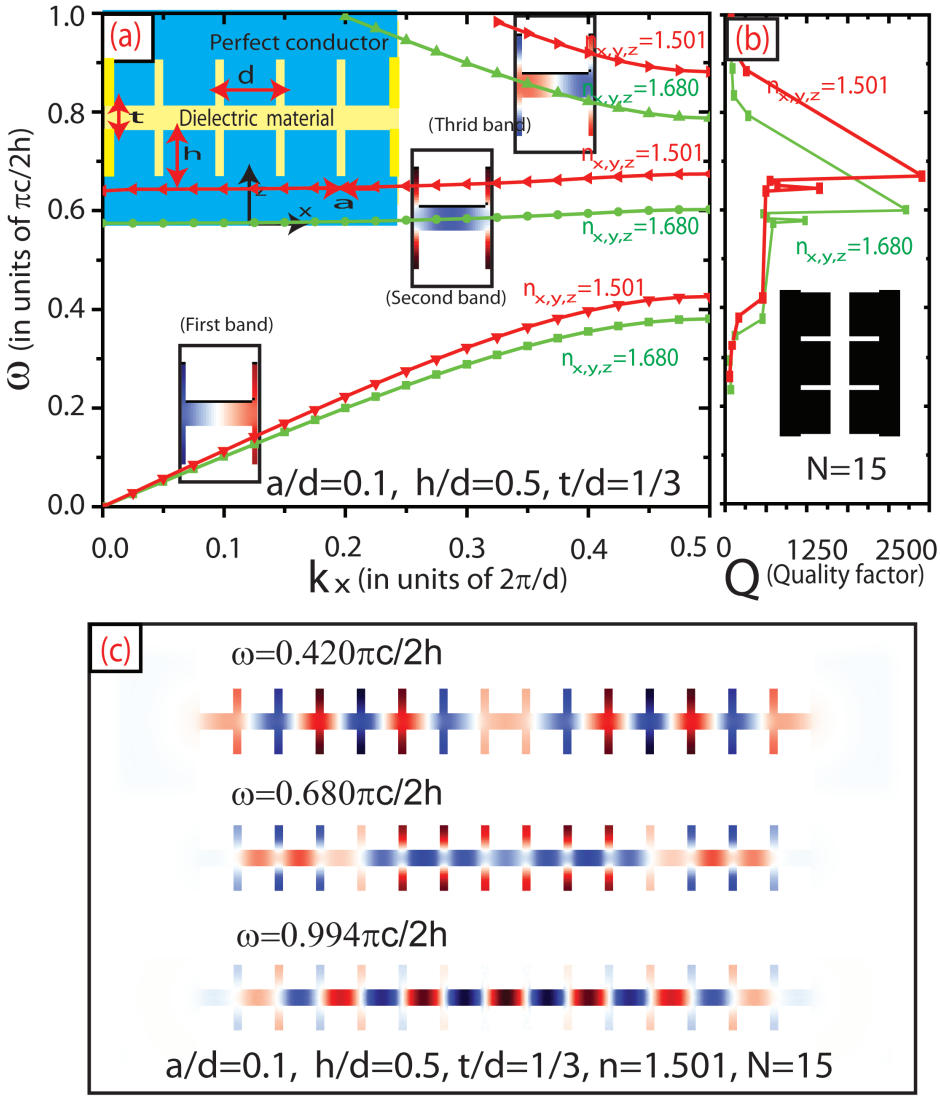

Figure 4.2: (a) Dispersion diagram of SSPP bound modes supported by the sandwiched conductor metamaterials with geometrical parameters $a/d = 0.1$, $h/d = 0.5$, and $t/d = 1/3$. (b) Quality factor Q for SSPP switch with the grooves ($N = 15$) is obtained by FDTD. (c) Mode profiles for SSPP switch with the grooves ($N = 15$) at three different operating frequencies: first-band mode ($\omega = 0.420\pi c/2h$), second-band mode ($\omega = 0.680\pi c/2h$), and third-band mode ($\omega = 0.994\ \pi c/2h$).

system. In our system, the net dimensionless decay rate can be rewritten as sum of two dominant decay rates: $1/Q = 1/Q_r + 1/Q_w$, where $1/Q_r$ and $1/Q_w$ denotes the radiative and waveguide decay rates, respectively. To eliminate the radiative loss and estimate the waveguide decay, we excite the Gaussian point source at the center of sandwiched structure with groove numbers (N=15) and analyze the response with the help of filter diagonalization method [84]. In this case, Q has a sharp peak at the specific frequency, thus verifying resonant modes and narrow band pass filter. Similar to the extraordinary transmission of sub-wavelength metallic holes [85],[86], the enhanced transmission through a corrugated sandwiched structure can be achieved by operating the resonant frequency. Secondly, to demonstrate the sub-wavelength SSPP confinement at resonant modes, the field profiles at three different frequencies are shown in Fig. 4.2(c). Fig. 4.2(c) shows the magnetic-field (H_z) patterns of states localized about a corrugated metallic gap. By examining the field profiles, the first band mode ($\omega = 0.420\pi c/2h$) shows the equally field distribution in the y-z plane. However, the third band mode ($\omega = 0.994\pi c/2h$) exhibits the alternating two different field concentrations in the y-z domain. Especially, at the resonant mode ($\omega = 0.680\pi c/2h$), the EM fields are mainly concentrated on the grooves, thus demonstrating strong SSPP subwavelength localization. Therefore, these features increase the high EM field intensity and sensitivity in a small volume, thus enhancing nonlinear optical effects for THz active devices such as switch and multiplexer.

In addition, for a more practical THz design, we need to optimize guiding parameters that SSPP resonant modes are located in the THz domain. The key design rule is that SSPP resonant frequency is inversely proportional to the refractive index (n) and height (h) as similar to cutoff frequency $\omega_c = \pi c/2n_x h$ in the one-dimensional SSPP structure. Fig. 4.3(a) shows the TM dispersion relations of sandwiched conductor meta-material supported by geometrical conditions: $a = 6\ \mu m$, $d = 60\ \mu m$, $h = 30\ \mu m$ and $t = 20\ \mu m$. In detail, at $n = 1.501$ and $n = 1.680$, the resonant

frequencies are about $\omega = 1.60$ THz and $\omega = 1.45$ THz, respectively. This resonant frequency modulation in our THz architecture enables us to control or steer the THz signal by manipulating the refractive indices of periodic grooves.

4.4 Spoof THz switch based on metamaterial

In this section, we apply the theoretical approach to practical implementation. To turn signal lines ON and OFF based on a shift of resonance frequency, a large birefringence is warranted at a low control signal, thus offering significant flexibility into existing optoelectronic devices. For example, the refractive index change can be achieved by several methods such as conventional electrooptic and nonlinear optical bistable material. In this chapter, we introduce the N-LC with the dielectric anisotropy defining as $\triangle n = n_e - n_o$, where n_e and n_o are refractive indexes parallel and perpendicular to the molecular axis [87],[88]. Furthermore, the LC birefringence can be easily controlled by changing alignment of LC based on a low voltage. In this way, the orientations of LC induced by electric field or optical excitation determine the three fundamental refractive indices of x-, y-, and z-axis, thus modifying the artificially engineered SSPP modes in the active THz switch.

To confirm the active switching operating at THz frequency based on the LC orientations, we conducted HFSS simulation based on the finite-element method (FEM). In the FDTD simulation, we investigated the basic principles of SSPP guiding 2-D structure based on the isotropic medium. However, in the FEM simulation, for a more realistic physical model, we designed a 3-D THz switch. The spatial snapshots of magnitude E field in the xz plane along the active 3-D finite THz switch, as shown in Fig. 4.3(b)−(d). Basically, the 2-D structure has one mirror symmetry plane $z = 0$, thus classifying the TM modes and TE modes. However, the 3-D structure has two mirror symmetry plane $z = 0$ and $y = 0$, thus all modes have symmetric (even) and antisymmetric (odd) with respect to two planes. Therefore, the guiding width

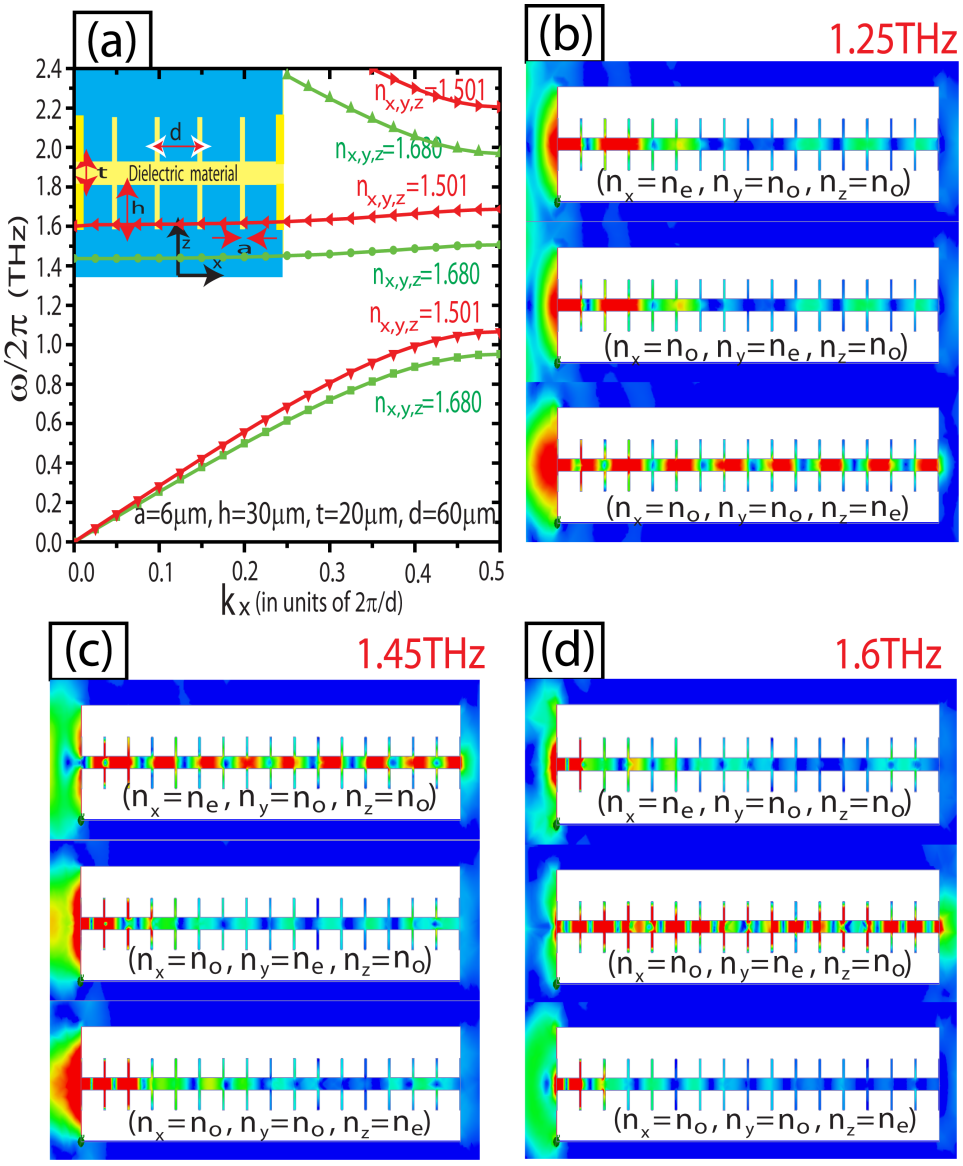

Figure 4.3: (a) Dispersion graphs of the spoof surface plasmon supported by the sandwiched conductor metamaterial with geometrical parameters for $a = 6$ μm, $d = 60$ μm, $h = 30$ μm, and $t = 20$ μm. (b)−(d) Spatial distributions of the E-field along the active THz switch devices for three different fundamental LC orientations at 1.25, 1.45, and 1.6 THz, respectively. The geometrical configurations for a = 6 μm, d = 60 μm, h = 30 μm, t = 20 μm, $n_o = 1.501$, and $n_e = 1.680$.

w is important factor to determine the dispersion curve and resonant frequency. For example, for the case of thin structure with small width w,the EM field modes are imposed by the two mirror symmetric conditions ($z = 0$ and $y = 0$). However, for the case of thick structure with large width w, the EM field modes almost constrained by the one mirror symmetric condition ($z = 0$). To verify the previous analytical method based on 2-D analysis, we use large width $w = 160\ \mu m$ (y-direction) and the structure has the same geometrical parameters of 2-D guiding structure containing 16 grooves. Furthermore, contrast to FDTD simulation, we use biaxial medium from N-LC with $n_o = 1.501$ and $n_e = 1.680$ [89]. Therefore, we consider three fundamental LC orientations: $(n_x = n_e, n_y = n_o, n_z = n_o)$, $(n_x = n_o, n_y = n_e, n_z = n_o)$, and $(n_x = n_o, n_y = n_o, n_z = n_e)$. As expected from the TM dispersion analysis, the THz guided wave along the guiding gap is engineered by different LC orientations. In particular, at 1.6 THz, the y alignment ($n_y = n_e$) of LC generates strongly coupled SSPP resonant modes, thus meaning ON-state. This field pattern is very similar to the resonant mode of FDTD simulation, as shown in Fig. 4.2(c). This extraordinary transmission can be explained by TM dispersion analysis, as shown in Fig. 4.3(a), because the SSPP modes based on the anisotropic medium are constrained by n_x and n_z as illustrated in (4.7). Therefore, the THz guided wave can be characterized by the isotropic medium ($n = 1.501$), thus the resonant modes are located at 1.6 THz. On the other hand, x or z alignment of LC prohibits THz pulse signal about the metamaterials, thus denoting OFF-state.

In order to obtain the optimal THz switching, Fig. 4.4(a)−(c) shows the E field amplitude calculated at the output of THz switch in which the periodic lattice (d = 60 μm), groove width (a = 6 μm), and thickness (t = 20 μm) are fixed, and at the heights (h) of 20, 30, and 40 μm, respectively. As shown, the transmittance of the SSPP bound modes along the plasmonic gap can be controlled by the guiding geometry, operation frequency f, and refractive index n [18]. Additionally, a dramatic

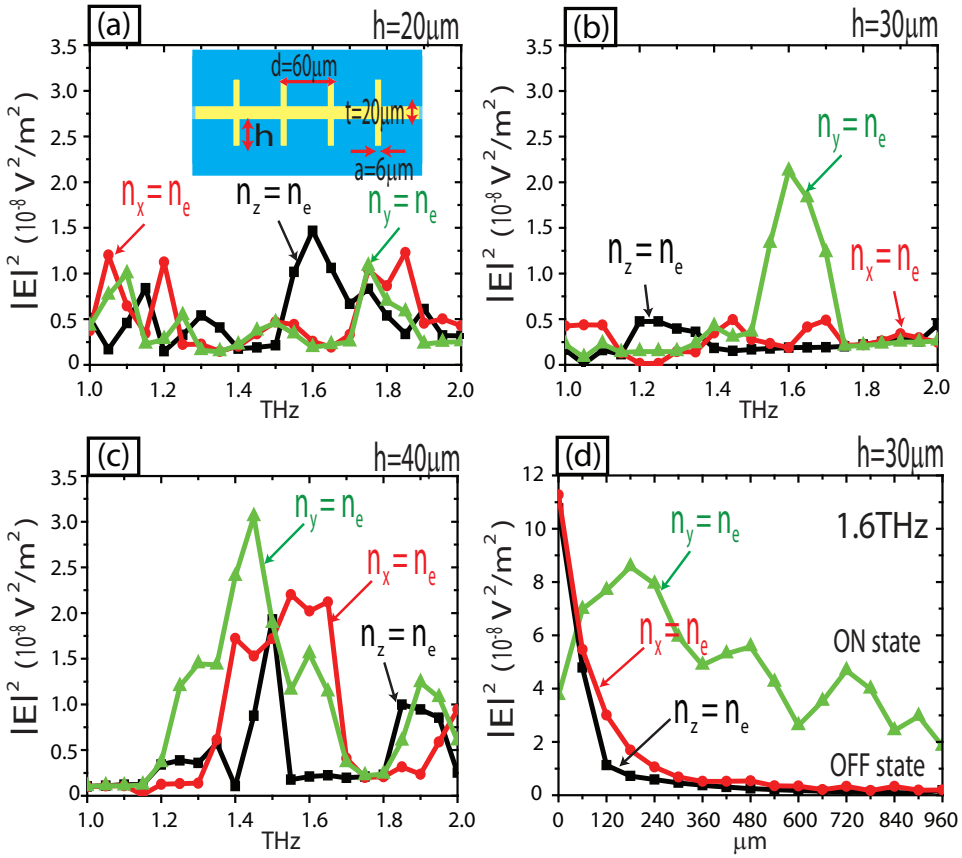

Figure 4.4: (a)−(c)E field amplitude versus frequency calculated at the output of THz switch in which the periodic lattice ($d = 60\ \mu m$) and groove width ($a = 6\ \mu m$) are fixed, and at the heights of 20, 30, and 40 μm, respectively. (d) Magnitude of E field, evaluated at $f = 1.6$ THz, along the x-direction at different locations of the metamaterials corresponding to three different fundamental LC orientations.

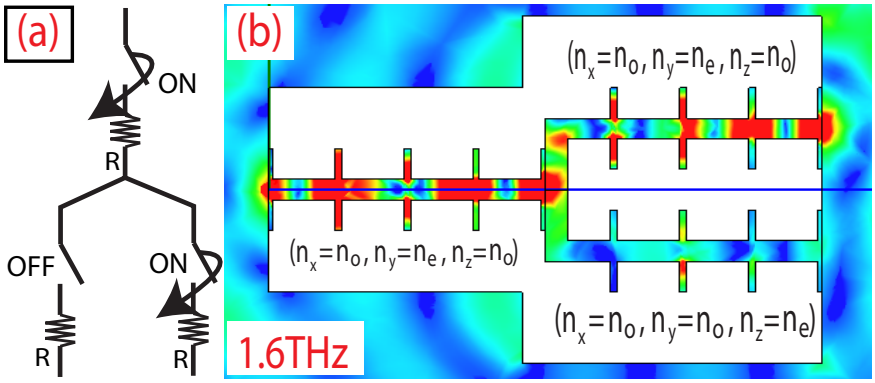

Figure 4.5: (a) Equivalent circuit of the THz Y-junction switch with three control signals. (b) Spatial distributions of the E-field along the active Y-junction THz switch with geometrical configurations for $a = 6\ \mu m$, $d = 60\ \mu m$, $h = 30\ \mu m$, and $t = 20\ \mu m$ at 1.6 THz.

dependence of the height of the corrugated structure is clearly visible. The increase in E magnitude with increasing height between 1 and 2 THz is due to the large depth of indentation leading to strong EM field penetration into the metallic side. Furthermore, the optimal guiding switching can be obtained at 1.6 THz with h = 30 μm, thus obtaining approximately maximum 10.51-dB extinction ratio defined as $r_e = 10\ \log(P_{ON}/P_{OFF})$ with ON-state (Y alignment) and OFF-state (X or Z alignment), as shown in Fig. 4.4(b). In addition, Fig. 4.4(d) shows the signal attenuation at different locations of metamaterials with a height of 30 μm at 1.6 THz corresponding to three different LC orientations. As apparent from the figure, the extraordinary SSPP resonance between grooves, in the ON-state(Y alignment), leads to small signal attenuation, thus having 3.21 dB/mm. However, in the OFF-state (X or Z alignment), the signal loss is almost equal to 18.51 dB/mm.

More importantly, this simple linear structure designed for the optimal switching condition can be easily extended to more complex logic elements. Fig. 4.5(a) shows the equivalent circuit model of a Y-junction THz switch containing four grooves in each section and independent control signal line. As shown in Fig. 4.5(b), this THz circuit model can be easily realized by manipulating the combination sets of LC orien-

tation. In the case of Y-junction switching, we can obtain intuitively understanding of signal transmission by applying coupled mode theory. Since each junction can be considered as a weak resonant cavity which is adjacent to THz waveguides, the transmission in ON-state or OFF-state depends on the specific junction geometry. In practical realizations, we need to consider the impedance matching issues between each junctions and THz corrugated waveguides. Additionally, the signal lines consisting of small grooves can solve the possible issues such as uniform LC alignment under an electric field or inherent LC damping. Furthermore, the geometry is simple to fabricate and can be easily implemented to execute THz Boolean logic algorithm.

4.5 Challenges and summary

In this chapter, we have demonstrated that active control of SSPP signal at THz frequencies can be accomplished by modulating the refractive index of N-LC material. However, further consideration must be given for practical implementation of the core idea proposed in this chapter.

(1) First, the main physical issue stems from limited bandwidth [90]. In principle, dramatic signal slow down and efficient energy transfer can be achieved by using resonant modes. However, the operation of resonance modes imposes significant bandwidth constraints, thereby limiting the range of available operational frequencies. For example, as shown in Fig. 4.2(a), the bandwidth of secondband mode is almost zero. To increase the bandwidth of second-band mode, we can design the bandwidth by choosing appropriate waveguide structures. For example, we can change geometrical parameter h/d based on the guiding parameters $a/d = 0.1$, $t/d = 1/3$, and $n = 1.501$, as shown in Fig. 4.6. More specifically, for small height $h/d = 0.3$ and large height $h/d = 0.7$, the bandwidth of second mode is large. However, for medium height $h/d = 0.5$, the bandwidth of second mode goes to zero, thus compressing the bandwidth of THz pulse, as shown in Fig. 4.6(b). Even though bandwidth compression enables

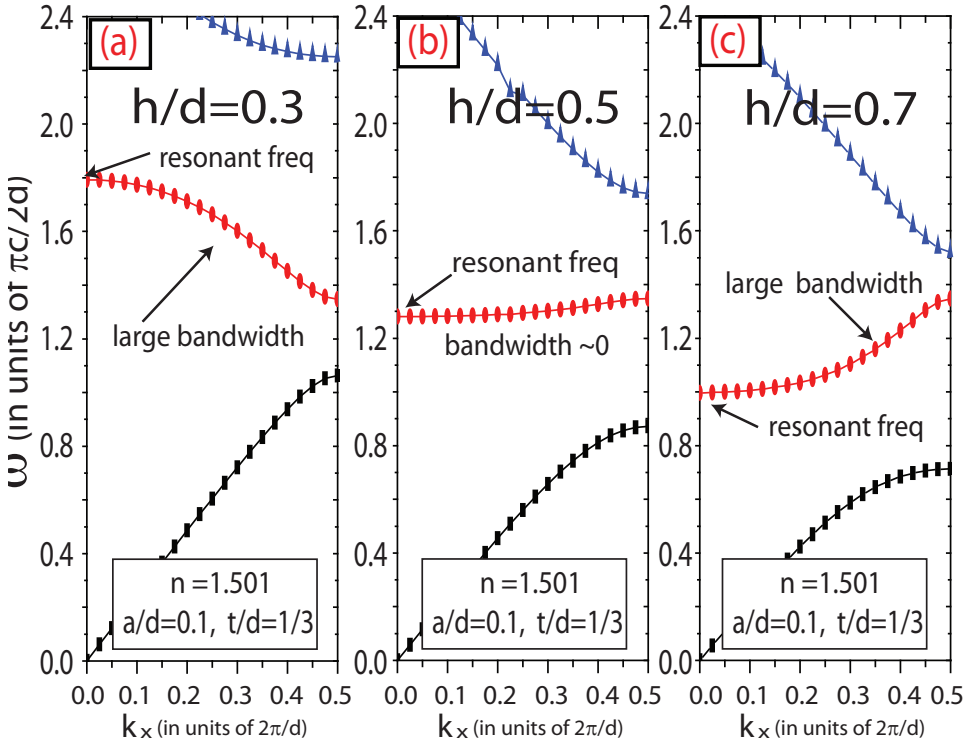

Figure 4.6: Dispersion diagram of SSPP bound modes supported by the sandwiched conductor metamaterials with geometrical parameters $a/d = 0.1$, $t/d = 1/3$, and $n = 1.501$ for three different choices of h/d. (a) At $h/d = 0.3$, the bandwidth of second band is large. (b) At $h/d = 0.5$, the bandwidth goes to zero. (c) At $h/d = 0.7$, the bandwidth of second band is large.

designers to spatially compress the pulsewidth and increase the internal fields, the small bandwidth is not desirable in THz applications. Therefore, it is essential to consider the delay-bandwidth product for an efficient THz switching device [91].

(2) Second, the switching speed of LC is significantly lower than conventional EO materials such as KH2PO4 or LiNbO3. This difficulty can be addressed by using other methods such as nonlinear EO, optically controlled, or loss-induced material [92]. Recently, SPP signals in metallic on dielectric waveguides can be controlled by using the phase transition of crystalline gallium [18]. As an alternative for SSPP routing, this phase transition owing to the temperature change or external optical excitation provides strong modulation strength ($\delta n/n$) and relatively fast switching speed

(3) Third, the inherent attenuation of LC in the THz domain may have an influence on SSPP dispersion, thereby changing resonant modes, bandwidth and quality factor (Q). In general, the SSPP dispersion mode strongly depends on the dispersive modulation (δn) and absorptive modulation ($\delta\alpha$). Since absorption is strongly related to signal attenuation, absorption modulation is not broadly considered as a switching mechanism. However, absorption modulation ($\delta\alpha$) may extend the degree of freedom for signal routing similar to absorptive optical bistability method.

(4) Fourth, the device performance depends on the polarization of the incident THz field. Therefore, the THz circuit system requires the TM polarizer at the input port.

(5) Fifth, the insertion loss at the input port has a large value because the input port and subwavelength gap structure have a significant impedance mismatch. To decrease the momentum mismatch, we can design the THz waveguide or switching system with a periodic arrangement of cutthrough corrugated slits [93]. This arrangement may lead to solve the momentum mismatch between the gap structure and input port.

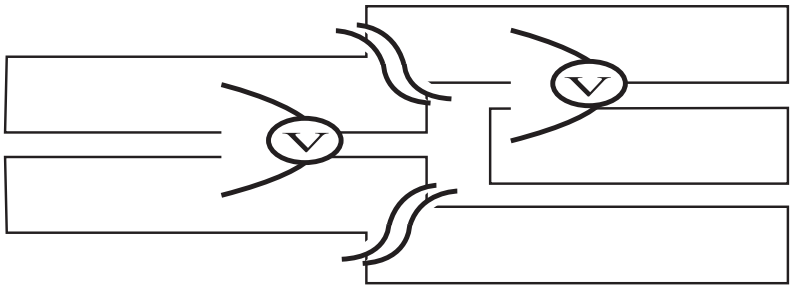

Figure 4.7: Schematic of the THz Y-junction switching: electric contacts placed directly onto the electrically disconnected metallic lines.

(6) Finally, the device implementation such as electrical contacts cannot be easily made. For example, in the case of Y-junction switch, if we assume that the electric contacts placed directly onto corrugated metallic structures, the metallic structure has physically the same voltage value. To obtain the different voltage configurations between signal lines, the device designers need to obtain electrically disconnected metallic lines, as shown in Fig. 4.6. In addition, electric contacts in the immediately vicinity of confined SSPP modes may result in additional signal loss. Therefore, it is essential to find a way to minimize the signal loss.

However, even though there remain many unresolved challenges to design experimental plasmon logic gates, the basic method presented here provides promising possibilities for the active THz device occupying an area of several micrometermeters square. In particular, the proposed linear Y-junction switching devices operate as a $2:1$ multiplexer, a fundamental building block in the digital systems. This chapter concludes that the unique properties of SSPP modes having strong subwavelength EM confinement, low signal attenuation, and high extinction ratio will open a new vista for the next generation subwavelength active THz devices.

CHAPTER V

One-dimensional surface plasmon photonic crystal slab for a nanophotodiode

5.1 Introduction

The periodic surface plasmon photonic crystal slab (SPPCS) modifies photonic properties of a metallic film by artificially tailoring a metallic sub-wavelength topology, thus leading to dramatic change of surface plasmon (SP) dispersion curves. Especially, the strong near field confinement and enhanced EM transmission of SPPCS generates considerable interest because this engineered SP dynamics opens up new possibilities and promising optoelectronic technology [94],[95],[96],[97],[98],[99],[100],[101]. For example, the ability to transmit EM field through the SPPCS could increase the efficiency of photonic devices such as TM polarizer [102] and optical filter [57]. In addition, the capability to increase SP near field intensity has large potential in optoelectronic devices such as photovoltaics [103] and light emitting diode (LED) [104]. In this chapter, we focus on a new way to enhance the photo-generation rate for a nano-photodiode by using one dimensional (1D) SPPCS. In general, the conventional photodiode usually use an antireflection layer (Fig. 5.1(a)) to decrease reflection loss in the semiconductor material, thereby obtaining maximum far field intensity. However, this small reflection loss method has some limitations for a miniaturization of

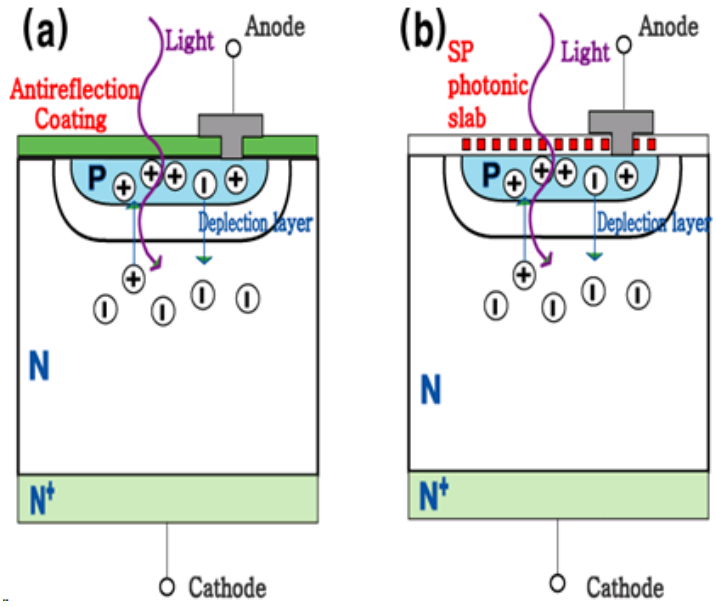

Figure 5.1: (a) Conventional photodiode with an antireflection coating. (b) Surface plasmon photonic slab (SPPCS) for a photodiode.

the optical circuitry. First of all, the size of antireflection coating is almost comparable to the wavelength of light. Furthermore, for the nano-photodiode, it is necessary to have a thinner depletion layer and small active semiconductor [11], thus resulting in the small amount of photo-generation rate because of smaller active semiconductor region under the far field optical field density. To overcome dimension issue of antireflection coating and low photo-generation rate in the small semiconductor layer of the nano-photodiode, the SPPCS (Fig. 5.1(b)) could be the best solution for three following reasons: (1) The SPPCS building blocks have the nano-scale dimensions, (2) The localized and delocalized SP modes from SPPCS concentrates strong photons to a small semiconductor layer, (3) TM polarized wave efficiently transmits through SPPCS, thus behaving like an antireflection coating.

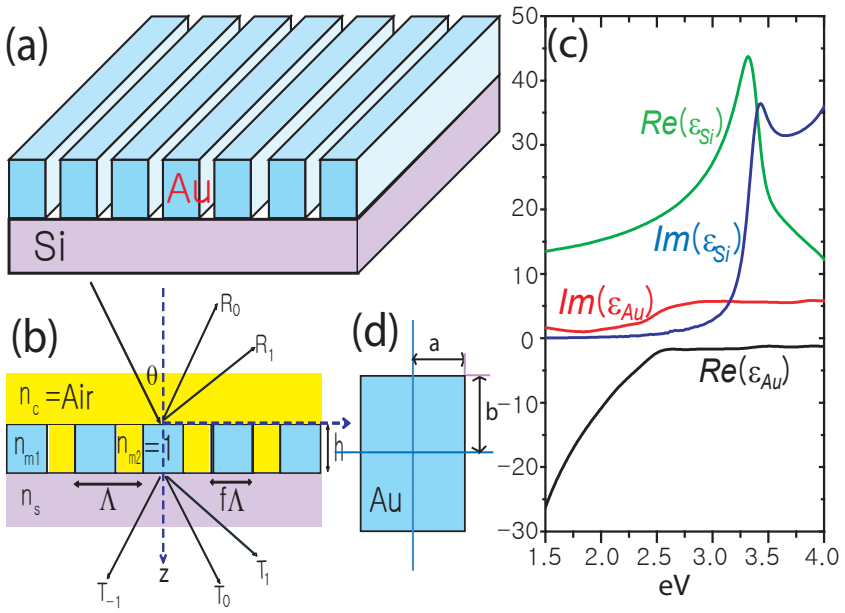

Figure 5.2: (a) Schematic view of SPPCS. (b) Geometry of SPPCS. The parameters are defined as in the figure: Λ is the periodicity, $f\Lambda$ is width of Au and h is the thickness of the SPPCS. (c) The complex dielectric constant of Au and Si was obtained by experimental data based on the cubic regression method. (d) The cross section of Au rectangular cylinder.

5.2 Dimensionless reduced polarzability of rectangular cylinder

Fig. 5.2(a) and 5.2(b) show schematics of our SPPCS photodiode of consisting of Si active semiconductor and Au (Gold) photonic slab. The grating structure is composed of two different media with Au and air (n=1). The frequency dependent optical properties of Au [50] and Si are obtained by interpolating the Johnson's and Palik's experimental data as displayed in Fig. 5.2(c). First, we have calculated the polarizability of the rectangular metallic cylinder (Fig. 5.2(d)) to obtain surface plamon (SP) resonant frequency for an efficient near field EM confinement in the semiconductor layer. Physically, when the wavelength of the incident field is large compared to the geometry of the metallic rectangular cylinder, the confined electron cloud generates the dipole-like polarization, thus explaining the surface plasmon resonance in the 2-D rectangular geometry. This polarizability of the rectangular metallic cylinder placed at free space (n=1) is given by [105]:

$$p_L = -8\chi ab(C_1 - C_2(a^2 - b^2)) \tag{5.1}$$

where χ is the electric susceptibility given by $\chi = (\epsilon_m - 1)/(4\pi)$, $\epsilon_m(\omega) = \epsilon_r(\omega) + \epsilon_i(\omega)$ is the complex dielectric function of metal, $C_1(\epsilon_m, a, b)$ and $C_2(\epsilon_m, a, b)$are function of ϵ_m, a and b. Eyges and Gianino have derived a detailed mathematical formulation for the polarizability of rectangular dielectric cylinders by using the Green function analysis [14]. Fig. 5.3(a) shows the magnitude of dimensionless reduced polarizability for rectangular SP cylinder (a=25nm, b=25nm) by using the Johnson's experimental data of three different noble metals: Cu (copper), Au (gold) and Ag (silver) [12]. As can be seen, compared with Cu and Au, Ag shows the maximum polarizability, thus generating strong EM field enhancement. However, the imaginary permittivity of Si tremendously increases from 3.0eV as shown in Fig. 5.2(c), thus the resonance

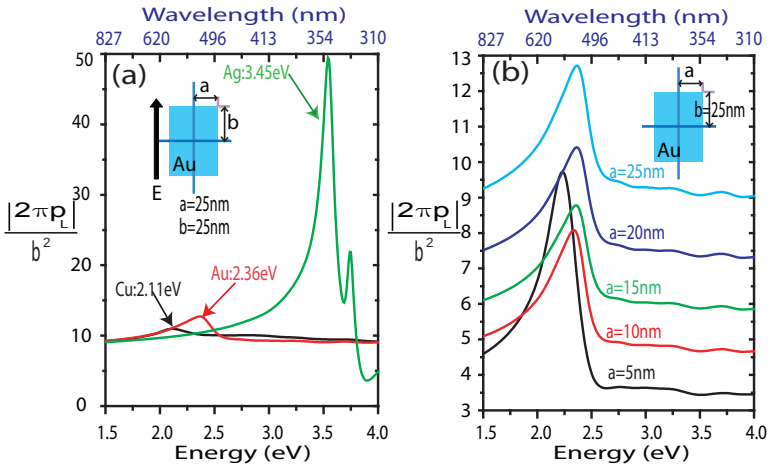

Figure 5.3: (a) Dimensionless reduced polarizability of rectangular SP cylinder as a function of photon energy. These curves are obtained from the cubic spline method by using the Johnson's experimental optical data of three different noble metals: Cu, Au and Ag. (b) Dimensionless reduced polarizability of Au rectangular cylinder with different geometry ratio (a/b).

frequency (3.49eV) of Ag rectangular cylinder lies in the strong damping region. Therefore, we choose Au to minimize far field damping loss in the semiconductor medium at the resonant condition (2.36eV) and obtain the efficient delocalized SP modes at the lower frequency. In Fig. 5.3(b), the magnitude of polarizability of Au cylinder can be manipulated by changing a (width) and b (height). As the ratio (r=a/b, b is 25nm) decreases, the magnitude of polarizability of Au also decreases because of the capacity of electron cloud inside the metallic cylinder

5.3 The photonic map of SPPCS

In order to check SP resonant modes have an effect on the efficiency of SPPCS photodiode. We have employed the rigorous coupled wave analysis (RCWA) to obtain TM-photonic maps including absorption, transmission and reflection [44], [45]. To demonstrate the usefulness of SPPCS for the photodiode, we first investigate the Au film (no grating structure) with thin thickness (h=50nm) shown in the inset of Fig. 5.4(a). First, we investigate the dispersion relations $\omega(k)$ for SP on the thin films by

considering EM boundary conditions at the two interfaces. The main reason is that the simplest way to understand the photonic behavior is to examine the SP dispersion relations. As can be seen, even (symmetric) SP modes and free space in a symmetric environment Air/Au/Air intersect with the critical point (2.48eV). Fundamentally, SP modes in the symmetric gap environment can be classified as even (symmetric) modes and odd (anti-symmetric) modes with respect to mirror symmetry. In this chapter, we ignore the anti-symmetric SP modes because symmetric SP modes are fundamental modes, for which SP modes have the smallest nodes. Similarly, the SP modes and free space in the anti-symmetric environment Air/Au/Si almost intersect the critical point. Physically, this means that when the frequency is below the critical point, the strong momentum mismatch occurs between incident wave and SP modes, thus producing the high reflection spectrum. However, above the critical point, the small momentum mismatch leads to the strong absorption inside the metallic film. More specifically, Fig. 5.4(b),(c) and (d) give us a clue on how the critical frequency (2.48eV) has influenced on the optical behavior of thin film. In Fig. 5.4(b),(c) and (d), the absorption, transmission and reflection maps of Air/Au/Si ranging from 1.5eV-4eV (photonic energies) and 0^0-90^0 (incident angles) are displayed. Below the critical frequency (2.48eV), most EM waves reflected because of strong momentum mismatch. However, at the critical frequency, the peak of transmission occurs as predicted by the SP dispersion analysis. As the frequency increase above the critical point, most incident EM waves absorb in the Au film.

These thin film photonic maps can be significantly modified by creating the photonic band structure. Fig. 5.5 demonstrates the photonic maps of SPPCS with periodicity (Λ=100nm), width ($f\Lambda$=50nm) and thickness (h=50nm). As can be seen in Fig. 5.5(a), the maximum reduced polarizability of rectangular SP cylinder occurs at the resonant frequency (2.36eV), thus leading to strong SP generator, thereby increasing the EM field intensity and enhancing the photo-generation rate in the Si

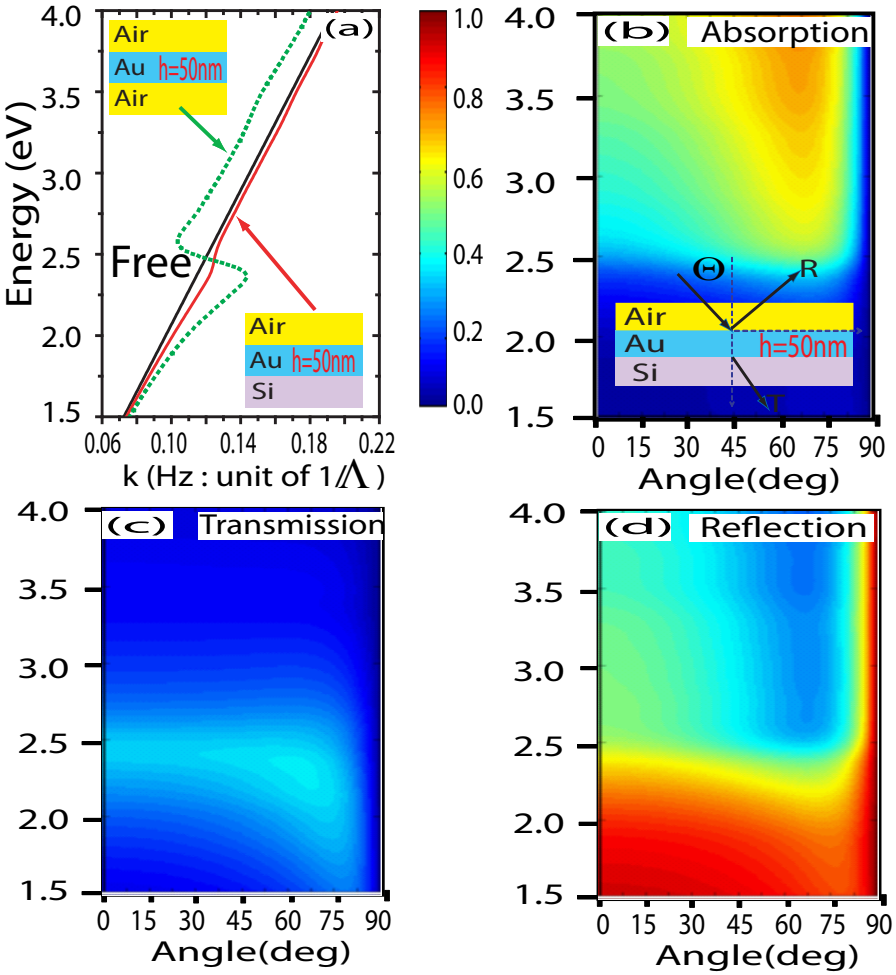

Figure 5.4: TM-photonic maps for a SPPCS (Air/Au/Si) with periodicity (Λ= 100nm), width ($f\Lambda$ =50nm) and thickness (h=50nm). These figures are presented for frequency from 1.5eV to 4eV and incident angles from 0^0 to 90^0. (a) Dimensionless reduced polarizability of Au rectangular SP cylinder as a function of photon energy. (b) Absorption map of SPPCS. (c) Transmission map of SPPCS. (d) Reflection map of SPPCS.

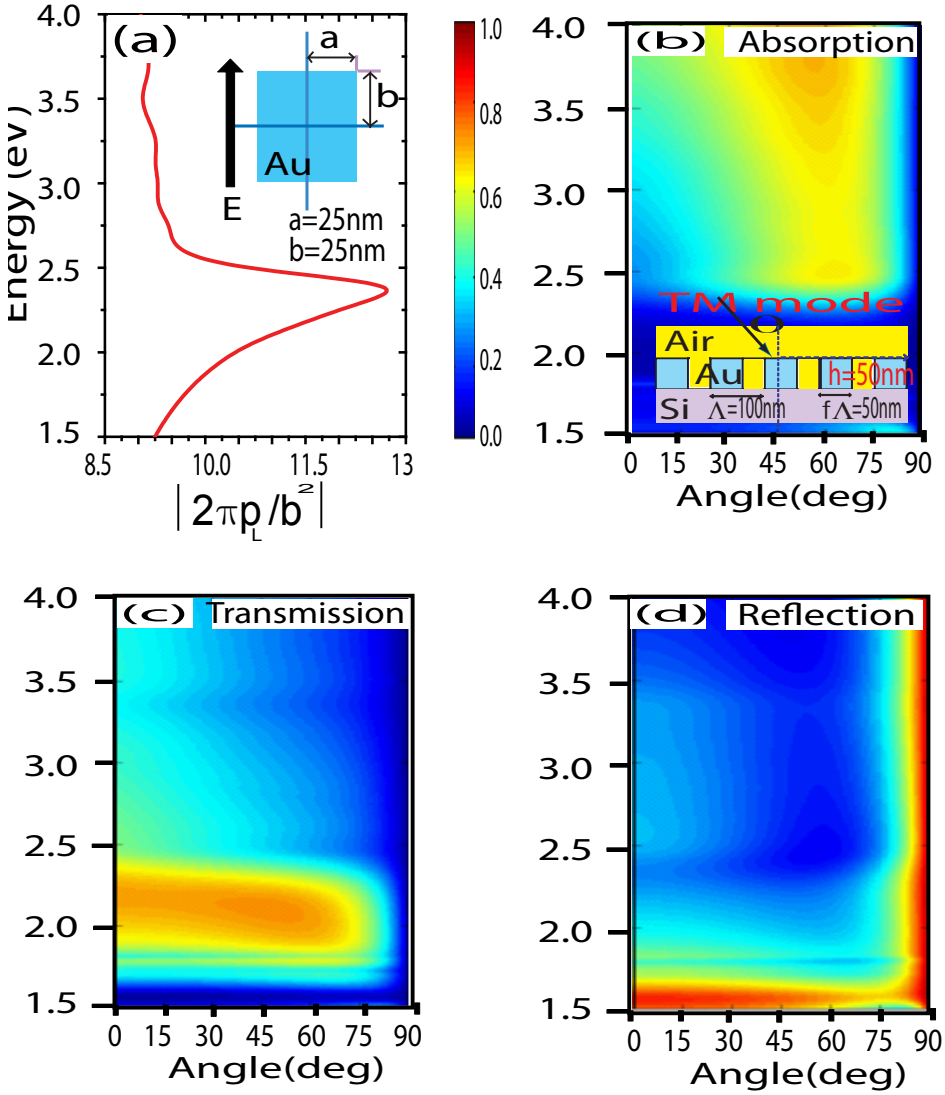

Figure 5.5: TM-photonic maps for a metallic slab (Air/Au/Si) with thickness 50nm. These figures are presented for frequency from 1.5eV to 4eV and incident angles from 0^0 to 90^0. (a) The dispersion relations ω(k) for SP on the thin films : Air/Au/Air (Green line) and Air/Au/Si (red-line). (b). Absorption map of thin film (Air/Au/Si) (c) Transmission map of thin film (Air/Au/Si). (d) Reflection map of thin film (Air/Au/Si)

medium. As shown in Fig. 5.5(b), even though absorption map of SPPCS does not significantly changed by creating the photonic band structure, strong SP resonance coupling between metallic rectangular cylinders leads to the extraordinary transmission and low reflection in angle-frequency domain as shown in Fig. 5.5(c)-(d).

5.4 The FEM simulation of a nanophotodiode

It has been shown that the photonic maps of SPPCS can be tailored, thus obtaining efficient light transmission in the active medium, we now focus on the realistic simulation for demonstrating strong light confinement and enhanced transmission in the SPPCS photodiode. In Fig. 5.6, we show that magnitude of near field density (black line) of SPPCS photodiode under the incident TM plane wave with incident angle θ=0 (degree) and amplitude E=1 $V/$m (field density=0.707 V/m^2) for following SPPCS geometry: periodicity (Λ =100nm), width ($f\Lambda$ =50nm) and thickness (h=50nm). Furthermore, contrast to previous RCWA structure, we make small air gap (5nm) between SPPCS and Si active medium to efficiently distribute strong near field at the surface of semiconductor layer. These graphs have been calculated by the near field pattern obtained by using HFSS simulation based on the finite element method (FEM). As predicted by polarizability analysis, the magnitude plot of near field density is similar to the magnitude graph of polarizability of rectangular SP cylinder, thus justifying the validity of polarizability method as shown in Fig. 5.5(a).

As shown in Fig. 5.6, the near field pattern has strong field profile at the corner of metallic rectangular cylinder. Furthermore, strong near field density profile between 2.16eV and 2.36eV can be explained by the electron cloud oscillation in the confined metallic cylinder. Even though the zigzag shape can be affected by numerical noises from HFSS, the obvious magnitude difference between SPPCS photodiode and uncoated SPPCS photodiode verify the usefulness of SPPCS for the near field enhancement. More specifically, the SPPCS generates to strong near field intensity

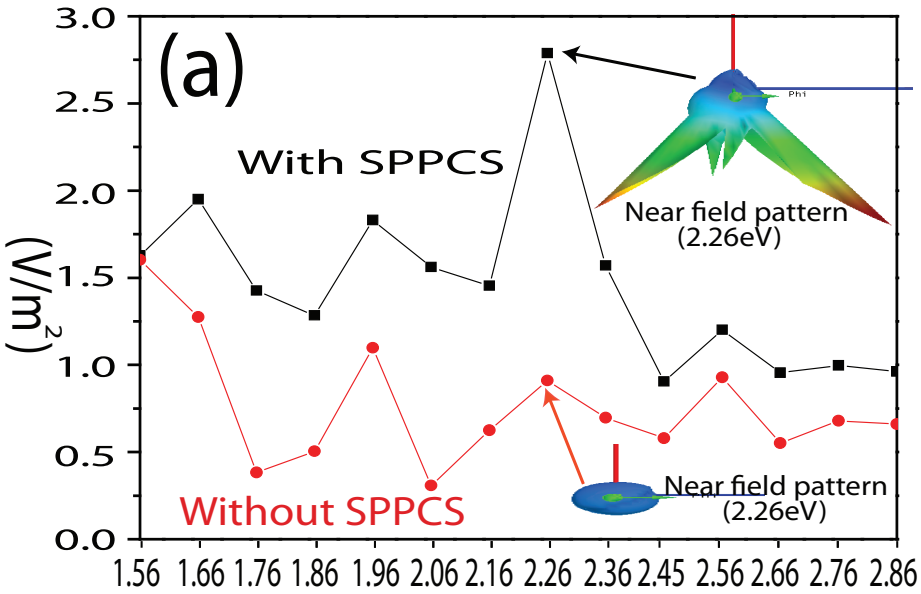

Figure 5.6: Comparison magnitude of near field density between SPPCS photodiode and uncoated SPPCS photodiode

($2.8\,V/\mathrm{m}^2$) at the resonant frequency 2.26eV, this value is four orders of magnitude increase compared to incident far field intensity ($0.707\,V/\mathrm{m}^2$). The small difference (0.01eV) of resonant frequency between polarizability calculation and FEM simulation method may be due to the fact that SP coupling between rectangular structures changes the location of resonant modes of SPPCS. In addition, the SPPCS photodiode gives a high value of directivity compared to uncoated SPPCS structure, thus focusing on strong near-field in the active semiconductor layer. Fig. 5.7(a)-(c) show the snapshots of magnitude of scattered E-field for three different frequencies. Especially, as shown in Fig. 5.7(a), at the low frequency (1.66eV), the strong E-field greater than E=2V/m occupies most active layer because the large wavelength generates delocalized SP modes and localized SP modes, and the optical properties of Si efficiently lead to confine the strong field intensity in the active medium. Fig. 5.7(b), at the resonant frequency (2.26eV), shows that localized SP modes from rectangular structures generate the strong near field intensity and extraordinary transmission

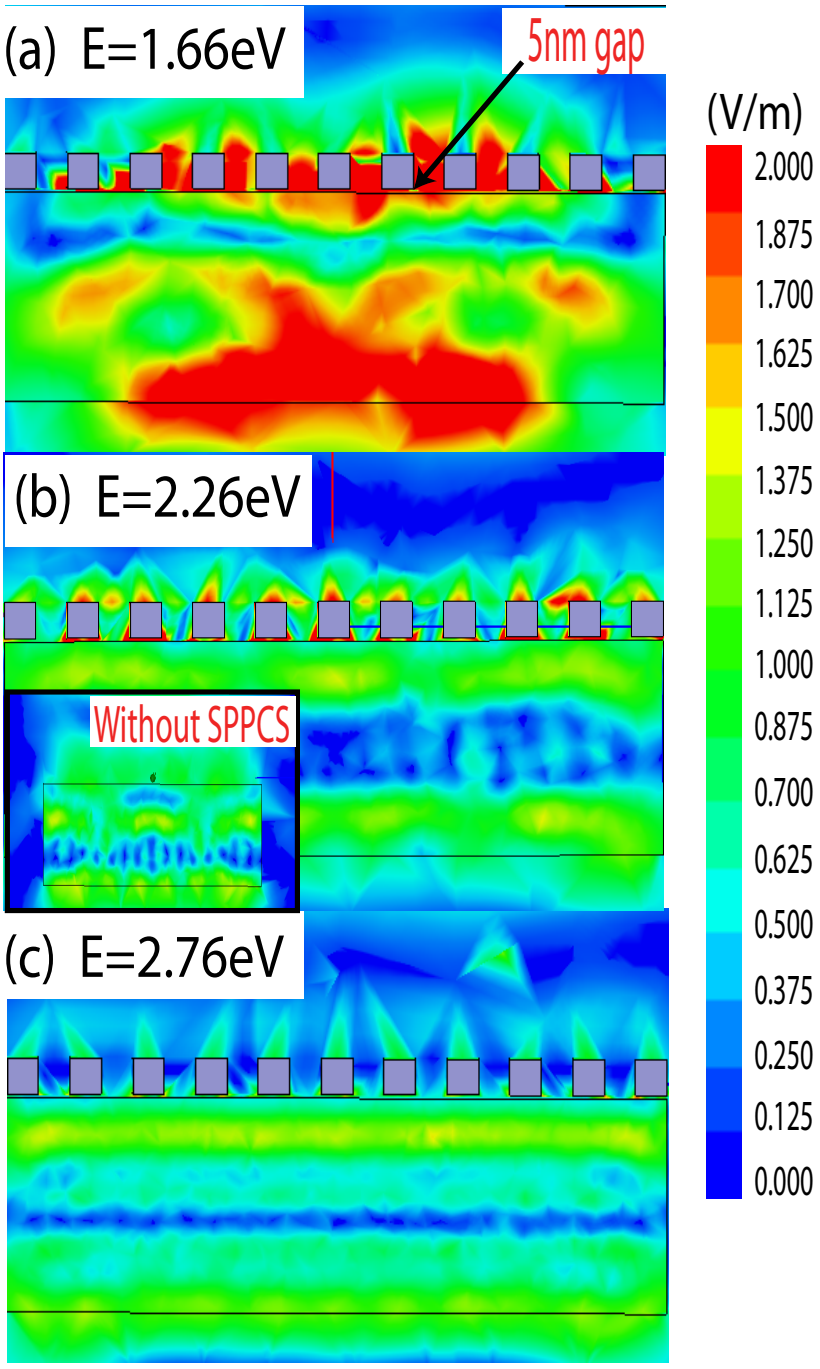

Figure 5.7: (a) The snapshot of magnitude of scattered E-field at 1.66eV. (b) The snapshot of magnitude of scattered E-field at 2.26eV. (c) The snapshot of magnitude of scattered E-field at 2.76eV.

compared to uncoated SPPCS photodiode as shown in the inset of Fig. 5.7(b). As the frequency increases up to 2.76eV, the SPPCS structure almost acts like an anti-reflection coating structure as given in Fig. 5.7(c).

5.5 Summary

In summary, we have presented a new SP nano-photodiode architecture based on 1D SPPCS. Specifically, at the resonant frequency (2.26eV), the four order increase of near field intensity (FEM calculation) and almost 70% EM transmission (RCWA calculation) has been demonstrated. The building geometry and noble metals of SPPCS can be changed for the purpose of optimizing EM transmission, near field generator and broadband sensitivity. Undoubtedly, this concept is extensible to the various promising photo-detector applications such as solar-cell technology and molecular bio-sensing.

CHAPTER VI

Conclusions and future work

6.1 Conclusions

Compressing light on a subwavelength scale is one of the most promising areas of current photonics and electronics [106]. However, it is not possible to confine the light radiated by nanometer size atoms or molecules to a lateral dimension smaller than wavelength of the light by using the conventional waveguiding methods. To overcome these challenges, plasmonics is an ideal candidate for two main reasons: (1) plasmonics uses low dimensional surface waves such as 1-D and 2-D, thus miniaturizing the optical components for solving the integration limit and (2) plasmonics devices provide strong light localization, thus allowing highly sensitive detection and signal transducer components. Thus, the emerging field of plasmonics strongly benefits the various areas such as near-field optics, quantum dots and optical processing.

Specifically, this disseration focuses on three main areas for ultrafast circuit systems: (1) passive plasmonics circuitry, (2) active plasmonics circuitry and (3) ultrafast photodectors. First, the dissertation introduces equivalent circuit modeling of metallic nanoparticle arrays and metallic nanowire. Next, the dissertation presents a new dynamic switching concept using the conductor metamaterial. Finally, the dissertation presents an efficient nano-photodiode using the surface plasmon photonic crystal slab.

6.2 Future work

In the electronic devices, the logic function utilizing series and parallel combinations of switches can be demonstrated by simple pass transistor logic circuits. For example, each of switches can be implemented by a single NMOS and by a pair of complementary MOS transistor, thus passing and blocking signal transmission. In our research, we demonstrate the equivalent circuit model of a Y-junction THz switch consisting four grooves in each section and independent control line. This THz logic circuitry can be easily realized by manipulating the combination sets of LC orientation. In a simple case, this 2:1 multiplexer, a functional digital building block can be easily accomplished by the pass-transistor logic gate. In the planned research, we will develop the various SSPP switches based on the various control methods such as refractive index modulation, absorptive modulation and all optical modulation.

First, we will design the active THz Mach-zender interferometers using the metamaterial. The THz Mach-zehnder interferometers can be designed by changing of wavevector k at small refractive index modulation δn/n$\sim$Ó(0.001). In detail, the SSPP dispersion engineering allows us to obtain the induced phased change $\delta\Phi = L\delta k$, where L is the length of the interferometer. The k can be approximately calculated by the first other perturbation theory [107]:

$$\delta\ k \sim \frac{\omega_o}{v_g}\frac{\delta n}{n}\int \varepsilon|E|^2 \tag{6.1}$$

where group velocity is v_g, resonant frequency ω_o and refractive index n. As shown, the bandwidth compression, THz field enhancement and slow light propagation of the corrugated perfect conductor metamaterial significantly increases the phase shift, thus providing the promising way for the large shift of wavevector (δk) at small length scale. Therefore, the efficient THz mach-zender interferometers based on the perfect conductor metamaterial are achieved.

Next, we will develop a simple channel drop SSPP structures comprising of two waveguides and a THz resonant system [108]. More importantly, channel drop filters can be used to backbone structure of photonic integrated systems and optical communication system. In detail, channel dropping filters can be used to access a wavelength division multiplexed signal along the one channel, while leaving other channels undistributed, thus providing an efficient filter behavior. Among various channel drop filter, the resonant systems are promising candidate for channeling dropping because the resonators with high quality factor Q can be used to obtain the high selectivity. The schematic of a resonant-cavity of the general channel drop filter, where two waveguides, the bus and drop, are coupled through a THz optical resonator. More importantly, the topology management enables us to obtain the ultrahigh cavity structure by designing the metallic structure on a subwavelenth scale. Therefore, we will realize the resonant-cavity channel drop filter using the sub-wavelength design method. Two waveguides can be achieved using the corrugated metallic structure. However, the cavity design is not simple because the resonator should be connected with bus channel and drop channel each other. In the future research, we will build up sub-wavelength gap structure between cavity and channels, thus providing the SSPP coupling mechanics. To achieve this task, it is essential to optimize the resonant frequencies of resonant resonator and THz channels, thus proving the effective resonant-cavity channel drop filter.

APPENDICES

APPENDIX A

Normal Surface of Anisotropic Media

We assume a monochromatic plane wave of angular frequency propagating in anisotropic medium with an electric field and a magnetic field

$$E\exp[i(\omega t - k \cdot r)] \qquad H\exp[i(\omega t - k \cdot r)] \tag{A.1}$$

From the Maxwell equation, we obtain

$$k \times (k \times E) + \omega^2 \mu \epsilon E = 0 \tag{A.2}$$

The fundamental dielectric tensor ϵ is given by $\epsilon = (\epsilon_x, \epsilon_y, \epsilon_z)$. This leads to a constitutive relation between ω and k

$$det \begin{bmatrix} \omega^2\mu\epsilon_x - k_y^2 - k_z^2 & k_x k_y & k_x k_z \\ k_y k_x & \omega^2\mu\epsilon_y - k_x^2 - k_z^2 & k_y k_z \\ k_z k_x & k_z k_y & \omega^2\mu\epsilon_z - k_x^2 - k_y^2 \end{bmatrix} = 0 \tag{A.3}$$

In the case of $k_y = 0$, we obtain two normal surfaces:

TM mode: $(k_{x,I}^n/n_z)^2 + (k_{z,I}^n/n_x)^2 = (\omega/c)^2$

TE mode: $(k_{x,I}^n + k_{z,I}^n)^2/n_y^2 = (\omega/c)^2$

APPENDIX B

Dispersion Diagram of Spoof Surface Plamson Polariton Along the Corrugated Periodic Metamaterial

The permittivity of Region I and grooves have anisotropic permittivity (n_x, n_y, n_z). Firstly, we are interested in calculating the dispersion relation of TM polarized waves propagating in the x direction along the corrugated wave structure bounded by anisotropic dielectric material. To analyze the TM dispersion analysis as a quasi-analytical form, the EM modes can be expanded in terms of Floquet modes that are characteristic waves for periodic structures. The H field with TM polarization (magnetic field perpendicular to the plane of grating structure in Region I) may be expressed in terms of modes:

$$H_y^I = \sum_{n=-\infty}^{+\infty} \rho_n \exp(jk_{z,I}^n z)\exp(jk_{x,I}^n x) \begin{Bmatrix} 0 \\ 1 \\ 0 \end{Bmatrix} \tag{B.1}$$

From the Maxwell equation:

$$E^I = \sum_{n=-\infty}^{+\infty} \rho_n \exp(jk_{z,I}^n z)\exp(jk_{x,I}^n x) \begin{Bmatrix} \frac{-k_z^n}{\omega\epsilon_x} \\ 0 \\ \frac{k_x^n}{\omega\epsilon_x} \end{Bmatrix} \tag{B.2}$$

where ρ_n are amplitude of diffractions $k_{x,I}^n = k_x + 2\pi n/d$ and $(k_{x,I}^n/n_z)^2 + (k_{z,I}^n/n_x)^2 = (\omega/c)^2$ account for biaxial index ellipsoids with $n_x^2 = \epsilon_x/\epsilon_0$, $n_y^2 = \epsilon_x/\epsilon_0$ $n_z^2 = \epsilon_z/\epsilon_0$ and c is the velocity of light. On the other hand, the circular normal surface $(k_{x,I}^n + k_{z,I}^n)^2/n_y^2 = (\omega/c)^2$ represents the TE polarization wave. However, in the Region *II* (blue), all fields are zero except inside the grooves (-a/2 $\leq$ x $\leq$ a/2) in the limit of the perfect conductor, thus H_y within the grooves can be written as a linear combination of the backward and forward z-directional TM modes:

$$H_y^{II} = A^+ \exp(jk_{II,z}z) + A^- \exp(-jk_{II,z}z) \tag{B.3}$$

and

$$E^{II} = A^+ \exp(jk_{II,z}z) \begin{Bmatrix} -\frac{k_{II,z}}{\omega\epsilon_x} \\ 0 \\ 0 \end{Bmatrix} + A^- \exp(-jk_{II,z}z) \begin{Bmatrix} \frac{k_{II,z}}{\omega\epsilon_x} \\ 0 \\ 0 \end{Bmatrix} \tag{B.4}$$

where A^+ and A^- are constants and $k_{II,z} = n_x\omega/c$ (in the case of TE polarization : $k_{II,z} = n_y\omega/c$).

The boundary conditions : It is straightforward to show that the dispersion relation of TM polarized surface wave propagating in x direction along the periodically corrugated meta-material can be rigorously derived by applying the boundary conditions: tangential E and H fields at the interface between Region I and II, tangential E fields vanishing at the perfect conductor surface and E fields at the bottom of the grooves(z=h).

1. First boundary condition (at z=0, only -a/2 $\leq$ x $\leq$ a/2) : $H_x^I = H_x^{II}$

2. Second boundary condition (at z=0, only -a/2 $\leq$ x $\leq$ a/2) : $E_x^I = E_x^{II}$

3. Third boundary condition (at z=h) : $E_x^{II} = 0$

From these boundary conditions, we obtain constitutive matrix with the form of a matrix equation $Q \times A = 0$, i.e.,

$$\begin{bmatrix} \sum_{n=-\infty}^{\infty} \frac{k_{z,II} S_n^2}{k_z n} - 1 & -\sum_{n=-\infty}^{\infty} \frac{k_{z,II} S_n^2}{k_z n} - 1 \\ \exp(jk_{II,z}h) & \exp(-jk_{II,z}h) \end{bmatrix} \begin{bmatrix} A^+ \\ A^- \end{bmatrix} = \begin{bmatrix} 0 \\ 0 \end{bmatrix} \tag{B.5}$$

The TM dispersion relation can be obtained in the condition of det $Q = 0$, i.e.,

$$1 - j \sum_n (\frac{k_{z,II} S_n^2}{k_{z,I}^n}) \tan(k_{z,II} h) = 0 \tag{B.6}$$

where j is $\sqrt{-1}$ and $S_n = (\sqrt{a/d})\text{sinc}(k_x^{(n)} a/2)$.

BIBLIOGRAPHY

BIBLIOGRAPHY

[1] RR Schaller. Moore's Law: Past, present, and future. *IEEE SPECTRUM*, 34(6):52–&, JUN 1997.

[2] LB Kish. End of Moore's law: thermal (noise) death of integration in micro and nano electronics. *PHYSICS LETTERS A*, 305(3-4):144–149, DEC 2 2002.

[3] RH Havemann and JA Hutchby. High-performance interconnects: An integration overview. *PROCEEDINGS OF THE IEEE*, 89(5, Sp. Iss. SI):586–601, MAY 2001.

[4] D.A.B Miller. Physical reasons for optical interconnection. *INTERNATIONAL JOURNAL OF OPTOELECTRONICS*, 11(3):155–168, MAY-JUN 1997.

[5] D.A.B. Miller. Rationale and challenges for optical interconnects to electronic chips. *PROCEEDINGS OF THE IEEE*, 88(6):728 –749, jun 2000.

[6] Mr Feldman, Sc Esener, Cc Guest, and Sh Lee. Comparison between optical and electrical interconects based on power and speed considerations. *APPLIED OPTICS*, 27(9):1742–1751, MAY 1 1988.

[7] D.A.B Miller. Optical interconnects to silicon. *IEEE JOURNAL OF SELECTED TOPICS IN QUANTUM ELECTRONICS*, 6(6):1312–1317, NOV-DEC 2000.

[8] Junichi Takahara, Suguru Yamagishi, Hiroaki Taki, Akihiro Morimoto, and Tetsuro Kobayashi. Guiding of a one-dimensional optical beam with nanometer diameter. *OPT. LETT.*, 22(7):475–477, 1997.

[9] E Ozbay. Plasmonics: Merging photonics and electronics at nanoscale dimensions. *SCIENCE*, 311(5758):189–193, JAN 13 2006.

[10] Liang Tang, Sukru Ekin Kocabas, Salman Latif, Ali K. Okyay, Dany-Sebastien Ly-Gagnon, Krishna C. Saraswat, and David A. B. Miller. Nanometre-scale germanium photodetector enhanced by a near-infrared dipole antenna. *NATURE PHOTONICS*, 2(4):226–229, APR 2008.

[11] Abram L. Falk, Frank H. L. Koppens, Chun L. Yu, Kibum Kang, Nathalie de Leon Snapp, Alexey V. Akimov, Moon-Ho Jo, Mikhail D. Lukin, and Hongkun Park. Near-field electrical detection of optical plasmons and single-plasmon sources. *NATURE PHYSICS*, 5(7):475–479, JUL 2009.

[12] Stefan A. Maier, Pieter G. Kik, Harry A. Atwater, Sheffer Meltzer, Elad Harel, Bruce E. Koel, and Ari A. Requicha. Local detection of electromagnetic energy transport below the diffraction limit in metal nanoparticle plasmon waveguides. *NAT MATER*, 2(4):229–232, April 2003.

[13] Stefan A. Maier, Pieter G. Kik, and Harry A. Atwater. Optical pulse propagation in metal nanoparticle chain waveguides. *PHYS. REV. B*, 67(20):205402, May 2003.

[14] Cecilia Noguez. Surface plasmons on metal nanoparticles: The influence of shpae and physical environment. *JOURNAL OF PHYSICAL CHEMISTRY C*, 111(10):3806–3819, MAR 15 2007.

[15] A. L. Gonzalez and Cecilia Noguez. Influence of morphology on the optical properties of metal nanoparticles. *JOURNAL OF COMPUTATIONAL AND THEORETICAL NANOSCIENCE*, 4(2):231–238, MAR 2007.

[16] Jean-Claude Weeber, Alain Dereux, Christian Girard, Joachim R. Krenn, and Jean-Pierre Goudonnet. Plasmon polaritons of metallic nanowires for controlling submicron propagation of light. *PHYS. REV. B*, 60(12):9061–9068, Sep 1999.

[17] Stefan A. Maier, Mark L. Brongersma, and Harry A. Atwater. Electromagnetic energy transport along yagi arrays. *MATERIALS SCIENCE AND ENGINEERING: C*, 19(1-2):291 – 294, 2002.

[18] M. Quinten, A. Leitner, J. R. Krenn, and F. R. Aussenegg. Electromagnetic energy transport via linear chains of silver nanoparticles. *OPT. LETT.*, 23(17):1331–1333, 1998.

[19] W Srituravanich, N Fang, C Sun, Q Luo, and X Zhang. Plasmonic nanolithography. *NANO LETTERS*, 4(6):1085–1088, JUN 2004.

[20] ML Brongersma, JW Hartman, and HA Atwater. Electromagnetic energy transfer and switching in nanoparticle chain arrays below the diffraction limit. *PHYSICAL REVIEW B*, 62(24):16356–16359, DEC 15 2000.

[21] SY Park and D Stroud. Surface-plasmon dispersion relations in chains of metallic nanoparticles: An exact quasistatic calculation. *PHYSICAL REVIEW B*, 69(12), MAR 2004.

[22] Jeffrey N. Anker, W. Paige Hall, Olga Lyandres, Nilam C. Shah, Jing Zhao, and Richard P. Van Duyne. Biosensing with plasmonic nanosensors. *NATURE MATERIALS*, 7(6):442–453, JUN 2008.

[23] K Aslan, JR Lakowicz, and CD Geddes. Nanogold-plasmon-resonance-based glucose sensing. *ANALYTICAL BIOCHEMISTRY*, 330(1):145–155, JUL 1 2004.

[24] JJ Greffet. Nanoantennas for light emission. *SCIENCE*, 308(5728):1561+, JUN 10 2005.

[25] Pierre Berini. Long-range surface plasmon polaritons. *ADV. OPT. PHOTON.*, 1(3):484–588, 2009.

[26] A Ono, J Kato, and S Kawata. Subwavelength optical imaging through a metallic nanorod array. *PHYSICAL REVIEW LETTERS*, 95(26), DEC 31 2005.

[27] G. Shvets, S. Trendafilov, J. B. Pendry, and A. Sarychev. Guiding, focusing, and sensing on the subwavelength scale using metallic wire arrays. *PHYS. REV. LETT.*, 99(5):053903, Aug 2007.

[28] Satoshi Kawata, Atsushi Ono, and Prabhat Verma. Subwavelength colour imaging with a metallic nanolens. *NATURE PHOTONICS*, 2(7):438–442, JUL 2008.

[29] Peter Nordlander. Plasmonics - Subwavelength imaging in colour. *NATURE PHOTONICS*, 2(7):387–388, JUL 2008.

[30] D. E. Chang, A. S. Sorensen, P. R. Hemmer, and M. D. Lukin. Quantum optics with surface plasmons. *PHYSICAL REVIEW LETTERS*, 97(5), AUG 4 2006.

[31] D. E. Chang, A. S. Sørensen, P. R. Hemmer, and M. D. Lukin. Strong coupling of single emitters to surface plasmons. *PHYS. REV. B*, 76(3):035420, Jul 2007.

[32] KL Wang and DM Mittleman. Metal wires for terahertz wave guiding. *NATURE*, 432(7015):376–379, NOV 18 2004.

[33] Stefan A. Maier and Steve R. Andrews. Terahertz pulse propagation using plasmon-polariton-like surface modes on structured conductive surfaces. *APPLIED PHYSICS LETTERS*, 88(25), JUN 19 2006.

[34] Stefan A. Maier, Steve R. Andrews, L. Martin-Moreno, and F. J. Garcia-Vidal. Terahertz surface plasmon-polariton propagation and focusing on periodically corrugated metal wires. *PHYSICAL REVIEW LETTERS*, 97(17), OCT 27 2006.

[35] Thomas W. Ebbesen, Cyriaque Genet, and Sergey I. Bozhevolnyi. Surface-plasmon circuitry. *PHYSICS TODAY*, 61(5):44–50, MAY 2008.

[36] JB Pendry, D Schurig, and DR Smith. Controlling electromagnetic fields. *SCIENCE*, 312(5781):1780–1782, JUN 23 2006.

[37] Kyungjun Song and Pinaki Mazumder. An Equivalent Circuit Modeling of an Equispaced Metallic Nanoparticles (MNPs) Plasmon Wire. *IEEE TRANSACTIONS ON NANOTECHNOLOGY*, 8(3):412–418, MAY 2009.

[38] Kyungjun Song and Pinaki Mazumder. Equivalent Circuit Modeling of Nonradiative Surface Plasmon Energy Transfer Along the Metallic Nanowire. *To be published : IEEE TRANSACTIONS ON NANOTECHNOLOGY*.

[39] Kyungjun Song and Pinaki Mazumder. Active Terahertz Spoof Surface Plasmon Polariton Switch Comprising the Perfect Conductor Metamaterial. *IEEE TRANSACTIONS ON ELECTRON DEVICES*, 56(11, Sp. Iss. SI):2792–2799, NOV 2009.

[40] Kyungjun Song and Pinaki Mazumder. One-Dimensional Surface Plasmon Photonic Crystal Slab (SPPCS) for a nanophotodiode. *IEEE TRANSACTIONS ON NANOTECHNOLOGY*, 9(4):470–473, Jul 2010.

[41] K. S. Yee. Numerical solution of initial boundary value problems involving Maxwell's equations in isotropic media. *IEEE T. ANTENN. PROPAG.*, 14, 1966.

[42] A Taflove and ME Brodwin. Numerical-solution of steady-state electromanetic scattering problems using time-dependent maxwells equations. *IEEE TRANSACTIONS ON MICROWAVE THEORY AND TECHNIQUES*, 23(8):623–630, 1975.

[43] A Taflove and ME Brodwin. Computation of electromagnetic-fields and induced temperatures within a model of microwave-irradiated human eye. *IEEE TRANSACTIONS ON MICROWAVE THEORY AND TECHNIQUES*, 23(11):888–896, 1975.

[44] MG Moharam, EB Grann, DA Pommet, and TK Gaylord. Formulation for stable and efficient implementation of the rigorous coupled-wave analysis of binary gratings. *JOURNAL OF THE OPTICAL SOCIETY OF AMERICA A-OPTICS IMAGE SCIENCE AND VISION*, 12(5):1068–1076, MAY 1995. Optical-Society-of-America 2nd Topical Meeting on Diffractive Optics, ROCHESTER, NY, JUN 06-09, 1994.

[45] MG Moharam, DA Pommet, EB Grann, and TK Gaylord. Stable Implementation of the rigorous coupled-wave analysis for surface-relief gratings - enhanced transmittance matrix approach. *JOURNAL OF THE OPTICAL SOCIETY OF AMERICA A-OPTICS IMAGE SCIENCE AND VISION*, 12(5):1077–1086, MAY 1995. Optical-Society-of-America 2nd Topical Meeting on Diffractive Optics, ROCHESTER, NY, JUN 06-09, 1994.

[46] MG Moharm and TK Gaylord. Rigorous coupled-wave analysis of planar-grating diffraction. *JOURNAL OF THE OPTICAL SOCIETY OF AMERICA*, 71(7):811–818, 1981.

[47] MG Moharam and TK Gaylord. Rigorous coupled-wave analysis of grating diffraction - E-mode polarization and losses. *JOURNAL OF THE OPTICAL SOCIETY OF AMERICA*, 73(4):451–455, 1983.

[48] W Nomura, M Ohtsu, and T Yatsui. Nanodot coupler with a surface plasmon polariton condenser for optical far/near-field conversion. *APPLIED PHYSICS LETTERS*, 86(18), MAY 2 2005.

[49] LL Yin, VK Vlasko-Vlasov, J Pearson, JM Hiller, J Hua, U Welp, DE Brown, and CW Kimball. Subwavelength focusing and guiding of surface plasmons. *NANO LETTERS*, 5(7):1399–1402, JUL 2005.

[50] PB Johnson and RW Christy. Optical-constants of noble-metals. *PHYSICAL REVIEW B*, 6(12):4370–4379, 1972.

[51] EJ Heilweil and RM Hochstrasser. Nonlinear spectroscopy and picosecond transient grating study of collidal gold. *JOURNAL OF CHEMICAL PHYSICS*, 82(11):4762–4770, 1985.

[52] A Melikyan and H Minassian. On surface plasmon damping in metallic nanoparticles. *APPLIED PHYSICS B-LASERS AND OPTICS*, 78(3-4):453–455, FEB 2004.

[53] N Engheta, A Salandrino, and A Alu. Circuit elements at optical frequencies: Nanoinductors, nanocapacitors, and nanoresistors. *PHYSICAL REVIEW LETTERS*, 95(9), AUG 26 2005.

[54] Mehboob Alam and Yehia Massoud. RLC ladder model for scattering in single metallic nanoparticles. *IEEE TRANSACTIONS ON NANOTECHNOLOGY*, 5(5):491–498, SEP 2006.

[55] LO Chua. Nonlinear circuit foundations for nanodevices, part I: The four-element torus. *PROCEEDINGS OF THE IEEE*, 91(11):1830–1859, NOV 2003.

[56] ES Kuh and IN Hajj. Nonlinear circuit theory - resistive networks. *PROCEEDINGS OF THE INSTITUTE OF ELECTRICAL AND ELECTRONICS ENGINEERS*, 59(3):340–&, 1971.

[57] William L. Barnes, Alain Dereux, and Thomas W. Ebbesen. Surface plasmon subwavelength optics. *NATURE*, 424(6950):824–830, August 2003.

[58] HB Bakoglu and JD Meindl. Optimal interconnection circuits for vlsi. *IEEE TRANSACTIONS ON ELECTRON DEVICES*, 32(5):903–909, 1985.

[59] T Dhane and D Dezutter. Selection of lumped element models for coupled lossy transmission-lines. *IEEE TRANSACTIONS ON COMPUTER-AIDED DESIGN OF INTEGRATED CIRCUITS AND SYSTEMS*, 11(7):805–815, JUL 1992.

[60] WA Challener, IK Sendur, and C Peng. Scattered field formulation of finite difference time domain for a focused light beam in dense media with lossy materials. *OPTICS EXPRESS*, 11(23):3160–3170, NOV 17 2003.

[61] H Ditlbacher, A Hohenau, D Wagner, U Kreibig, M Rogers, F Hofer, FR Aussenegg, and JR Krenn. Silver nanowires as surface plasmon resonators. *PHYSICAL REVIEW LETTERS*, 95(25), DEC 16 2005.

[62] T Sakurai. Closed-form expressions for interconnection delay, coupling, and crosstalk in vlsis. *IEEE TRANSACTIONS ON ELECTRON DEVICES*, 40(1):118–124, JAN 1993.

[63] AE Ruehli and PA Brennan. Efficient capacitance calculations for 3-dimensional multiconductor systems. *IEEE TRANSACTIONS ON MICROWAVE THEORY AND TECHNIQUES*, MT21(2):76–82, 1973.

[64] ND Arora, KV Raol, R Schumann, and LM Richardson. Modeling and extraction of interconnect capacitances for multilayer VLSI circuits. *IEEE TRANSACTIONS ON COMPUTER-AIDED DESIGN OF INTEGRATED CIRCUITS AND SYSTEMS*, 15(1):58–67, JAN 1996.

[65] MW Beattie and LT Pileggi. On-chip induction modeling: Basics and advanced methods. *IEEE TRANSACTIONS ON VERY LARGE SCALE INTEGRATION (VLSI) SYSTEMS*, 10(6):712–729, DEC 2002.

[66] JAB Faria. On the partial-capacitance scheme for multiple conductor systems. *MICROWAVE AND OPTICAL TECHNOLOGY LETTERS*, 47(4):346–349, NOV 20 2005.

[67] PH Siegel. Terahertz technology. *IEEE TRANSACTIONS ON MICROWAVE THEORY AND TECHNIQUES*, 50(3):910–928, MAR 2002.

[68] R Kohler, A Tredicucci, F Beltram, HE Beere, EH Linfield, AG Davies, DA Ritchie, RC Iotti, and F Rossi. Terahertz semiconductor-heterostructure laser. *NATURE*, 417(6885):156–159, MAY 9 2002.

[69] DM Mittleman, RH Jacobsen, and MC Nuss. T-ray imaging. *IEEE JOURNAL OF SELECTED TOPICS IN QUANTUM ELECTRONICS*, 2(3):679–692, SEP 1996.

[70] S Hunsche, DM Mittleman, M Koch, and MC Nuss. New dimensions in T-ray imaging. *IEICE TRANSACTIONS ON ELECTRONICS*, E81C(2):269–276, FEB 1998.

[71] JB Pendry, L Martin-Moreno, and FJ Garcia-Vidal. Mimicking surface plasmons with structured surfaces. *SCIENCE*, 305(5685):847–848, AUG 6 2004.

[72] AP Hibbins, BR Evans, and JR Sambles. Experimental verification of designer surface plasmons. *SCIENCE*, 308(5722):670–672, APR 29 2005.

[73] G Goubau. Surface waves and their application to transmission lines. *JOURNAL OF APPLIED PHYSICS*, 21(11):1119–1128, 1950.

[74] W Rotman. A study of single-surface corrugated guides. *PROCEEDINGS OF THE INSTITUTE OF RADIO ENGINEERS*, 39(8):952–959, 1951.

[75] AV Krasavin and NI Zheludev. Active plasmonics: Controlling signals in Au/Ga waveguide using nanoscale structural transformations. *APPLIED PHYSICS LETTERS*, 84(8):1416–1418, FEB 23 2004.

[76] Darrick E. Chang, Anders S. Sorensen, Eugene A. Demler, and Mikhail D. Lukin. A single-photon transistor using nanoscale surface plasmons. *NATURE PHYSICS*, 3(11):807–812, NOV 2007.

[77] J. Gomez Rivas, J. A. Sanchez-Gil, M. Kuttge, P. Haring Bolivar, and H. Kurz. Optically switchable mirrors for surface plasmon polaritons propagating on semiconductor surfaces. *PHYSICAL REVIEW B*, 74(24), DEC 2006.

[78] Bowen Wang, Yi Jin, and Sailing He. Design of subwavelength corrugated metal waveguides for slow waves at terahertz frequencies. *APPLIED OPTICS*, 47(21):3694–3700, JUL 20 2008.

[79] AP Hibbins, MJ Lockyear, and JR Sambles. The resonant electromagnetic fields of an array of metallic slits acting as Fabry-Perot cavities. *JOURNAL OF APPLIED PHYSICS*, 99(12), JUN 15 2006.

[80] FJ Garcia-Vidal, L Martin-Moreno, and JB Pendry. Surfaces with holes in them: new plasmonic metamaterials. *JOURNAL OF OPTICS A-PURE AND APPLIED OPTICS*, 7(2, Suppl. S):S97–S101, FEB 2005.

[81] YA Vlasov, M O'Boyle, HF Hamann, and SJ McNab. Active control of slow light on a chip with photonic crystal waveguides. *NATURE*, 438(7064):65–69, NOV 3 2005.

[82] ML Povinelli, SG Johnson, and JD Joannopoulos. Slow-light, band-edge waveguides for tunable time delays. *OPTICS EXPRESS*, 13(18):7145–7159, SEP 5 2005.

[83] G Lenz, BJ Eggleton, CK Madsen, and RE Slusher. Optical delay lines based on optical filters. *IEEE JOURNAL OF QUANTUM ELECTRONICS*, 37(4):525–532, APR 2001.

[84] A. Farjadpour, David Roundy, Alejandro Rodriguez, M. Ibanescu, Peter Bermel, J. D. Joannopoulos, Steven G. Johnson, and G. W. Burr. Improving accuracy by subpixel smoothing in the finite-difference time domain. *OPTICS LETTERS*, 31(20):2972–2974, OCT 15 2006.

[85] TW Ebbesen, HJ Lezec, HF Ghaemi, T Thio, and PA Wolff. Extraordinary optical transmission through sub-wavelength hole arrays. *NATURE*, 391(6668):667–669, FEB 12 1998.

[86] ZC Ruan and M Qiu. Enhanced transmission through periodic arrays of subwavelength holes: The role of localized waveguide resonances. *PHYSICAL REVIEW LETTERS*, 96(23), JUN 16 2006.

[87] AL Zhang, KT Chan, MS Demokan, VWC Chan, PCH Chan, HS Kwok, and AHP Chan. Integrated liquid crystal optical switch based on total internal reflection. *APPLIED PHYSICS LETTERS*, 86(21), MAY 23 2005.

[88] M Kobayashi, H Terui, M Kawachi, and J Noda. 2X2 Optical-waveguide matrix switch using nematic liquid-crystal. *IEEE JOURNAL OF QUANTUM ELECTRONICS*, 18(10):1603–1610, 1982.

[89] Fuli Zhang, Qian Zhao, Lei Kang, Davy P. Gaillot, Xiaopeng Zhao, Ji Zhou, and Didier Lippens. Magnetic control of negative permeability metamaterials based on liquid crystals. *APPLIED PHYSICS LETTERS*, 92(19), MAY 12 2008.

[90] Toshihiko Baba. Slow light in photonic crystals. *NATURE PHOTONICS*, 2(8):465–473, AUG 2008.

[91] Mehmet Fatih Yanik, Wonjoo Suh, Zheng Wang, and Shanhui Fan. Stopping light in a waveguide with an all-optical analog of electromagnetically induced transparency (vol 93, pg 233903, 2004). *PHYSICAL REVIEW LETTERS*, 98(14), APR 6 2007.

[92] M Soljacic, M Ibanescu, SG Johnson, Y Fink, and JD Joannopoulos. Optimal bistable switching in nonlinear photonic crystals. *PHYSICAL REVIEW E*, 66(5), NOV 2002.

[93] JT Shen, PB Catrysse, and SH Fan. Mechanism for designing metallic metamaterials with a high index of refraction. *PHYSICAL REVIEW LETTERS*, 94(19), MAY 20 2005.

[94] A Christ, SG Tikhodeev, NA Gippius, J Kuhl, and H Giessen. Waveguide-plasmon polaritons: Strong coupling of photonic and electronic resonances in a metallic photonic crystal slab. *PHYSICAL REVIEW LETTERS*, 91(18), OCT 31 2003.

[95] FJ Garcia-Vidal and L Martin-Moreno. Transmission and focusing of light in one-dimensional periodically nanostructured metals. *PHYSICAL REVIEW B*, 66(15), OCT 15 2002.

[96] C. Genet and T. W. Ebbesen. Light in tiny holes. *NATURE*, 445(7123):39–46, JAN 4 2007.

[97] F. J. Garcia de Abajo. Colloquium: Light scattering by particle and hole arrays. *REVIEWS OF MODERN PHYSICS*, 79(4):1267–1290, OCT-DEC 2007.

[98] N. Garcia and M. Nieto-Vesperinas. Theory of electromagnetic wave transmission through metallic gratings of subwavelength slits. *JOURNAL OF OPTICS A-PURE AND APPLIED OPTICS*, 9(5):490–495, MAY 2007.

[99] E Moreno, FJ Garcia-Vidal, D Erni, JI Cirac, and L Martin-Moreno. Theory of plasmon-assisted transmission of entangled photons. *PHYSICAL REVIEW LETTERS*, 92(23), JUN 11 2004.

[100] A Lewis, H Taha, A Strinkovski, A Manevitch, A Khatchatouriants, R Dekhter, and E Ammann. Near-field optics: from subwavelength illumination to nanometric shadowing. *NATURE BIOTECHNOLOGY*, 21(11):1377–1386, NOV 2003.

[101] A. V. Kabashin, P. Evans, S. Pastkovsky, W. Hendren, G. A. Wurtz, R. Atkinson, R. Pollard, V. A. Podolskiy, and A. V. Zayats. Plasmonic nanorod metamaterials for biosensing. *NATURE MATERIALS*, 8(11):867–871, NOV 2009.

[102] Z. Y. Yang and Y. F. Lu. Broadband nanowire-grid polarizers in ultraviolet-visible near-infrared regions. *OPTICS EXPRESS*, 15(15):9510–9519, JUL 23 2007.

[103] Nicolae C. Panoiu and Richard M. Osgood, Jr. Enhanced optical absorption for photovoltaics via excitation of waveguide and plasmon-polariton modes. *OPTICS LETTERS*, 32(19):2825–2827, OCT 1 2007.

[104] J Vuckovic, M Loncar, and A Scherer. Surface plasmon enhanced light-emitting diode. *IEEE JOURNAL OF QUANTUM ELECTRONICS*, 36(10):1131–1144, OCT 2000.

[105] L Eyges and P Gianino. Polarizabilities of rectangular dielectric cylinders and of a cube. *IEEE TRANSACTIONS ON ANTENNAS AND PROPAGATION*, 27(4):557–560, 1979.

[106] Alexander A. Govyadinov and Viktor A. Podolskiy. Metamaterial photonic funnels for subdiffraction light compression and propagation. *PHYS. REV. B*, 73(15):155108, Apr 2006.

[107] M Soljacic, SG Johnson, SH Fan, M Ibanescu, E Ippen, and JD Joannopoulos. Photonic-crystal slow-light enhancement of nonlinear phase sensitivity. *JOURNAL OF THE OPTICAL SOCIETY OF AMERICA B-OPTICAL PHYSICS*, 19(9):2052–2059, SEP 2002.

[108] SH Fan, SG Johnson, JD Joannopoulos, C Manolatou, and HA Haus. Waveguide branches in photonic crystals. *JOURNAL OF THE OPTICAL SOCIETY OF AMERICA B-OPTICAL PHYSICS*, 18(2):162–165, FEB 2001.